



UNIVERSITÀ DEGLI STUDI DI SALERNO Dipartimento di Farmacia

PhD Program

in Drug Discovery and Development

XXXV Cycle — Academic Year 2022/2023

PhD Thesis in

Alginate hydrogels in drug delivery: from physico-chemical to technological studies of a promising polysaccharide for 3D printing application

Candidate Tutor

Giovanni Falcone Prof. Paola Russo

Co-Tutor

Prof. Pasquale Del Gaudio

PhD Program Coordinator: Prof. Dr. Gianluca Sbardella

"My powers are ordinary.

Only my application brings me success"

Isaac Newton

Index

Abbreviations	vi
Outlines of the project	ix
1 Introduction	1
1.1 The new frontier of healthcare: the Personalized medicine	1
1.2 3D printing of pharmaceuticals, the keystone to develop personal therapeutic management	
1.3 3D printing: classification and technical aspects	8
1.3.1Printing based ink-jet systems	11
1.3.2 Laser-based writing systems	12
1.3.3 Nozzle-based deposition systems	13
1.3.3.1 Fused Filament Fabrication (FFF)	14
1.3.3.2 Semi Solid Extrusion (SSE)	15
1.4 Semi-solid extrusion 3D printing: focus on potentialities and issue pharmaceutical technology	
1.5 Alginate-based hydrogels, increasing interest for the 3D printing application	24
Section 1	29
Extemporaneous gelation of alginate in coaxial semi solid extrusion 3 printing process: development of innovative 3D printed platforms	
2.1 Research aim	29
2.2 Materials & Methods	30
2.2.1 Materials	30
2.2.2Methods	31

2.2.2.1 Inks spreading measurement	31
2.2.2.2 Dynamic viscosity measurement	31
2.2.2.3 DDS Digital optimization & SSE printing process	32
2.2.2.4 Printing resolution and process reproducibility	34
2.2.2.5 Drying process	35
2.2.2.6 Morphological Analysis	35
2.2.2.7 Buoyancy tests and DDS density	36
2.2.2.8 Media induced matrix behaviour (medium up-take test)	36
2.2.2.8 FT-IR analysis	37
3.2.2.7 DSC Thermal Analysis	37
2.2.2.9 Drug content analysis and drug-loading efficiency	38
2.2.2.10 Dissolution tests	38
2.2.11 Release kinetics fitting studies	39
2.3 Results and discussion	40
2.4 Conclusion	60
Application of the alginate extemporaneous gelation for the procustomizable Ricobendazole DDS for veterinary use	
3.1 Scientific background and research aim	62
3.2 Materials & Methods	63
3.2.1 Materials	63
3.2.2 Methods	64
3.2.2.1 Alginate and Crosslinking Ink Preparation	64
3.2.2.2 Rheological characterization	65
3.2.2.3 DDS Digital optimization & SSE printing process	66
3.2.2.4 Printing resolution and reproducibility	67
3.2.2.5 Morphological Analysis	68

3.2.2.6 FT-IR analysis	68
3.2.2.7 DSC Thermal Analysis	68
3.2.2.8 Buoyancy tests	69
3.2.2.9 Drug content analysis and drug-loading efficiency	69
3.2.2.10 Dissolution tests	70
3.2.2.11 Release kinetics fitting studies	70
3.2.2.12 Mechanical investigation of DDS strength	72
3.3 Results and discussion	72
3.4 Conclusion	86
Section 2	87
Pre-crosslinked alginate hydrogels as a new tool in semi solid printing process	
4.1 Research aim	87
4.2 Materials & Methods	88
4.2.1 Materials	88
4.2.2 Methods	88
4.2.2.1 Hydrogel inks production	88
4.2.2.2 Magnetic Resonance Imaging (MRI) of calcium-alginate hyd	drogels90
4.2.2.3 Differential scanning calorimetry	94
4.2.2.4 Rheological characterization	94
4.2.2.5 Inks spreading measurement	95
42.2.6 DDS Digital optimization & SSE printing process	95
4.2.2.7 Printing resolution and reproducibility	96
4.3 Results and discussion	97
4.4 Conclusion	110

Application of the 3D printable alginate hydrogels ink for the of Flurbiprofen loaded personalized DDS	
5.1 Research aim	121
5.2 Materials & Methods	121
5.2.1 Materials	121
5.2.2 Methods	122
5.2.2.1 Ink gel production	122
5.2.2.2 Rheological characterization	123
5.2.2.3 DDS Digital optimization & SSE printing process	123
5.2.2.4 Printing resolution and reproducibility	124
5.2.2.5 FT-IR analysis	125
5.2.2.6 Drug content analysis and drug-loading efficiency	125
5.2.2.7 Dissolution tests	126
5.2.2.8 Release kinetics fitting studies	126
5.3 Results and discussion	127
5.4 Conclusion	137
Application of the 3D printable alginate hydrogels ink for th of easy to swallow tablets	-
6.1 Scientific background and research aim	139
6.2 Materials & Methods	140
6.2.1 Materials	140
6.2.2 Methods	141
6.2.2.1 3D-printable hydrogels preparation	141
6.2.2.2 Rheological evaluation of 3D printable hydrogels	142
6.2.2.3 Inks spreading measurement	142
6.2.2.4 Printability evaluation	143
6.2.2.5 DDS Digital optimization & SSE printing process	144
6.2.2.6 3D-printed platforms resolution and reproducibility	145

6.2.2.7 Drying impact: morphological and mass analysis	146
6.2.2.8 Morphological analysis	146
6.2.2.9 Platforms mechanical characterization	147
6.2.2.10 Media induced matrix behavior	148
6.2.2.11 Statistical analysis	148
6.3 Results and discussion	149
6.4 Conclusion	163
7 Conclusion & Perspectives	165
9 Bibliography	167
Sitography	193
Appendix	194
List of papers	194
Oral communications	195

Abbreviations

AM Additive Manufacturing

ANOVA Analysis of variance

API Active pharmaceutical ingredient

CAD Computer aided design

CAM Computer aided manufacturing

CIJ Continuous ink-jet

CMC Critical micelle concentration

CSD Controlled shear deformation

DC Drug content

DDS Drug delivery system

DIFF Water self-diffusion coefficients

DLE Drug loading efficiency

DoD Drop on demand

DOS Drop on solid

DSC Differential scanning calorimetry

EMA European Medicine Agency

FB Flurbiprofen

FDA Food & Drug Administration

FDM Fused deposition modelling

FFF Fused filament fabrication

FT-IR Fourier-transform infrared spectroscopy

GMP Good Manufacturing Practice

GRDDS Gastro-retentive drug delivery system

HEC Hydroxyethyl cellulose

HPMC Hydroxypropyl methyl cellulose

LBF Lipid-based formulations

LVER Linear viscoelastic region

LWF Line width fidelity

MEK Methyl ethyl ketone

MRI Magnetic Resonance Imaging

MSME Multi-slice-multi-echo

MSUD Maple syrup urine disease

NMR Nuclear magnetic resonance

ODFs Orodispersible films

PAM Pressure-assisted microsyringe

PBS Phosphate-buffered saline

PFG Pulse field gradient

PLA Polylactic acid

PLGA Poly Lactic-co-Glycolic Acid

Prp Propranolol Hydrochloride

RARE Rapid acquisition with relaxation enhancement

RBZ Ricobendazole

ROI Region of interests

SA Sodium alginate

SEM Scanning electron microscopy

SLA Stereolithography

SLM Selective laser melting

SLS Selective laser sintering

SSE Semi-solid extrusion

Outlines of the project

Since the introduction of personalized medicine, the attention of the experts in the pharmaceutical field has been focused on the balancing between efficiency and sustainability of personalized therapeutic approach. To find this equilibrium and facilitate the healthcare system transition, the contribution of technological improvements plays a crucial role, investigating innovative production processes that could fit the patient's variety. Among the newest manufacturing process the 3D printing technologies thanks to the rapid prototyping, the on demand and flexible manufacturing, are catching the attention of the scientific community as confirmed by the increased number of literature articles from 2012 to date.

Based on this background, this research project aimed to explore the potentiality of a specific 3D printing technique, the Semi-solid extrusion for the development and the production of personalized drug delivery systems. The selection of this specific technique was due to the unexplored potentialities of Semi-solid extrusion 3D printing due to the absence of suitable and versatile feedstock for drug loading. In particular the attention was focused on natural polymeric hydrogels referred as inks in the following sections.

Polymeric hydrogels could be considered the most promising class of carrier matrices for personalized medicine; however, their application in 3D printing is still limited by several issues associated to their physico-chemical properties i.e. poor ink flow control, low layer fidelity during the printing and the needs of post printing process. Among the large number of polymers, potential candidates for this investigation, the alginate hydrogels were selected thanks to their biocompatibility, biodegradability and pH-dependent solubility.

However, alginate hydrogels, do not fulfil the printing requirements, causing the spreading of the extruded material onto the building plate after the printing and after the drying processes. In literature, the layers spreading, as well as the collapse of the 3D structure of the alginate printed forms were reported as the most critical challenges that must be overcome to exploit alginate hydrogels in 3D printing production process.

To overcome these limits, it was speculated the possibility to obtain alginate 3D printed platforms taking advantage of the well-known ionotropic gelation of alginate in combination with divalent cations (Figure 1). This alginate peculiar gelation, should allow to improve the ink's shape retention after printing and after drying, while maintaining the ink extrudability.

$$Ca^{2+} \longrightarrow Ca^{2+}$$

$$Alginate blocks$$

$$Egg-box structure$$

Figure 1 Graphical representation of calcium-alginate gelation process

Two different gelation timing were investigated i.e., an extemporaneous cross-linking at the nozzle during the printing, and a cross-linking step before printing. Both studies required several steps:

- a carefully physico-chemical characterization of hydrogel inks, to highlight the influence of each excipient and active ingredient on inks printability;
- the optimization of the operative printing parameters in accordance with the highlighted inks' differences,
- the production of DDS via SSE 3D printing
- post-printing drying
- DDS characterization, in terms of dimensions, shape, physical properties, drug content, drug release kinetics.

In the first part of the project, exploiting the *in-situ* alginate gelation at the nozzle during the printing, the attention was focused on the development of an innovative co-axial process, pumping the alginate ink and the cross-linking ink into two different channels and allowing the crosslinking immediately after the

extrusion. The inks involved in the process (alginate ink and crosslinking agent ink) were optimized to balance the extrudability and the gelation requirements, reaching a good resolution and reproducibility of the printing process. The morphological analysis of the dried platforms suggested the possibility to exploit the hollow structure obtained to develop floating platform. In fact, the hypothesis to apply this process in the pharmaceutical field was investigated producing floating drug delivery systems with two different APIs i.e., propranolol hydrochloride, and ricobendazole. The physico-chemical differences between them, such as water solubility, drove the variation of inks' composition Independently from the inks' composition, it was possible to reach high resolution of the printing process, as well as high reproducibility during both printing and drying steps. The technological characterization of all printed drug delivery systems (i.e., propranolol hydrochloride, and ricobendazole) showed very interesting results in agreement with the idea of therapy personalization. Specifically, the possibility to modulate the dosage and the floating properties was demonstrated, and obtained varying the digital model and/or the inks composition to obtain personalized DDS in accordance to the patient's needs.

Differently, in the second part of the project, the keystone exploited for the application of alginate as a tool in the Semi-solid extrusion 3D printing process was the modulation of the entanglement between alginate and calcium. In detail, thanks to several analytical technologies, a physico-chemical

characterization of crosslinked alginate hydrogels was carried out relating the hydrogels' characteristics with their final printability. The data acquired were analysed to establish a protocol for the development of advanced printable alginate inks. The impact of different calcium-alginate microstructure was also investigated in relation to the morphological changes after drying process. The matrices obtained from calcium-alginate egg-box multimeric structures showed the best shape retention, the inks being still extrudable. At the end of the feasibility study, it was investigated and demonstrate the possibility to add into these inks APIs (i.e., flurbiprofen) as well as functional excipients (such us mannitol or sorbitol) that easily allow to tune the final properties of the printed platforms i.e., DDS dimension, drug content and release, DDS swallowability.

The results of this Ph.D. project, herein described, represent an important step on the long path towards the on-demand and customizable production of dosage forms through SSE-3D printing



1 Introduction

Based on the Review article

Auriemma, G.; Tommasino, C.; Falcone, G.; Esposito, T.; Sardo, C.; Aquino, R.P. Additive Manufacturing Strategies for Personalized Drug Delivery Systems and Medical Devices: Fused Filament Fabrication and Semi Solid Extrusion. Molecules 2022, 27, 2784.

https://doi.org/10.3390/molecules27092784

1.1 The new frontier of healthcare: the Personalized medicine

The need to control spending and to ensure the sustainability of healthcare system led, in the first decade of the new millennium, to the introduction of an economic logic that results in the standardization of processes i.e., introduction of protocols, standards, etc. in healthcare services. Patient care, for example, is classified in 'groups of diseases' based on protocols systems, that define standardized procedures of treatment to determine the payment due to healthcare providers. This concept is more evident focusing on the pharmaceutical field characterized by mass therapeutic treatment "one size fit all". However, assuming that the standardization of healthcare services ensures the economic management, it reduces the quality of the service, and the attention on patients' variety (Amir-Aslani & Mangematin, 2010). With the aim to balance these phenomena, in the last decade, EMA and FDA, the main agencies responsible for advancing the public health, started several

actions promoting the switch from the standard to the personalized medicine (Figure 1.1) (https://s3platform.jrc.ec.europa.eu/personalised-medicine).



Figure 1.1 Mass manufacturing vs on-demand manufacturing

Personalized Medicine Coalition (PMC) published the seventh annual (2021) analysis of the Food and Drug Administration's activities in personalized medicine, highlighting that more than 25% of newly approved drugs are personalized medicine (Figure 1.2) (https://personalizedmedicinecoalition.org)

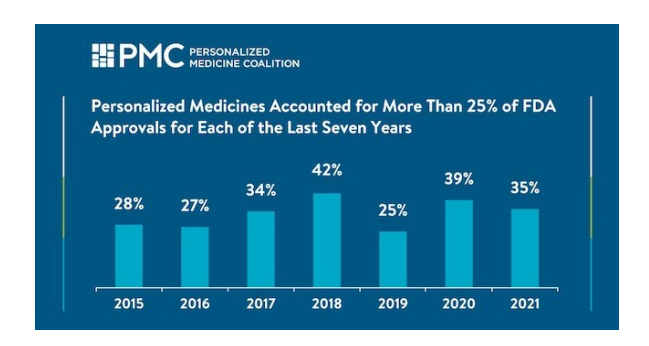


Figure 1.2 Ratio (%) of personalized medicines approved vs the total products approved from 2015 to 2021 (https://personalizedmedicinecoalition.org)

The concept of personalized medicine could be perfectly explained citing the words of the 21st Commissioner of FDA Margaret A. Hamburg, M.D. "The concept of personalized medicine is not new: clinicians have long observed that patients with similar symptoms may have different illnesses, with different causes; and similarly, that medical interventions may work well in some patients with a disease but not in others with apparently the same disease. What is new is that advances in a wide range of fields from genomics to medical imaging to regenerative medicine, along with computational power and the advent of mobile and wireless capability and other technologies, are allowing patients to be treated and monitored more precisely and effectively and in ways that better meet their individual needs" (Administration, 2013). In fact, in accordance with the great deal of interindividual variations due to the increasing results on DNA sequencing and omics investigation, it is not possible to consider the patients as a homogeneous whole (Chan & Ginsburg, 2011; Goetz & Schork, 2018). The differences in age, gender, environmental information, and the coexistence of multiple pathologies must be considered to establish the best decision and to ensure the patient compliance and therapy adherence (Mathur & Sutton, 2017; Vizirianakis, 2004). The personalized approach in healthcare could be described as a circular path where each step is characterized by a technological key from pharmacogenomic and/or pharmacometabolomic investigation, to the therapeutically tailored medications (Figure 1.3) (Soni, Gowthamarajan, & Radhakrishnan, 2018).



Figure 1.3 Graphical representation of keystones for personalized medicine

From this perspective, people and technology represent the two basic components of the new healthcare systems, where patients represent the main source of variety and the technology the instrument to harmonize the effectiveness, efficiency, and sustainability of healthcare (Aquino, Barile, Grasso, & Saviano, 2018).

Focusing on the technological aspects of a tailored therapeutic approach, one of the main topics that has seen rapid advances over the past decade is 3D printing, a set of "Additive Manufacturing technologies" (AM) able to manipulate biomaterials, cells, and molecules to create on-demand custom structures in a reproducible manner (Prendergast & Burdick, 2020).

1.2 3D printing of pharmaceuticals, the keystone to develop personalized therapeutic management

The reasons behind the strong increase in 3D printing applications in the pharmaceutical field lie in the growing demand for complex drug-loading products, medical devices, advanced drug-device combination products, and the request of on-demand manufacturing (Ho et al., 2020).

An overview of scientific literature about 3D printing allows to underline the increasing interest of pharmaceutical research about these technologies. In fact, the number of scientific papers recorded in the Web of Science Core Collection containing the terms "3D printing" in the title increased from 57 in 2012 to 4623 in 2021. In addition, the number of citations of these papers in the same period grew from 23 to 28,438. Narrowing the searching results to the pharmacy/pharmacology category, no result was found in 2012, whereas 553 records were found up to 2021.

3DP offers a forward-looking view of both drug manufacturing and dispensing, moving the attention from traditional mass production to on demand production, and then from centralized towards decentralized facilities (Gao et al., 2015). In the light of this analysis, it is possible to say with certainty that 3DP represents today one of the fastest developing technologies in the healthcare field (Di Prima et al., 2016). As also confirmed from the launch of *Emerging Technology Program* by FDA *Center for Drug Evaluation and Research's (CDER) Office of Pharmaceutical Quality*

(https://www.fda.gov/about-fda/center-drug-evaluation-and-researchcder/emerging-technology-program), and the subsequent publication of "Technical Considerations for Additive Manufactured Medical Devices" by FDA in 2017 (https://www.fda.gov/regulatory-information/search-fdaguidance-documents/technical-considerations-additive-manufacturedmedical-devices). In fact, after the approval by the FDA of the first 3D-printed drug product, Spritam® by Aprecia, in August 2015 (West & Bradbury, 2019), several big pharmaceutical companies took up the challenge to explore the emerging 3DP technologies, and possibly to integrate them into their workflows, with investments of millions of dollars. The 3D-printed pharmaceuticals market was valued at \$175.19 million in 2020 and anticipated to grow to \$285.17 million by 2025, representing a significant opportunity to able to capitalize on its benefits companies and overcome (https://www.marketresearch.com/360iResearch-v4164/3D-Printed-Drugs-Research-Technology-32372054/).

When discussing about 3D printing in pharmaceutical field, there is a fundamental difference between small-scale compounding in the hospital and pharmacy setting or large-scale manufacturing in the industry setting. The main benefits deriving from decentralizing pharmaceutical manufacturing are the following (Awad, Trenfield, Gaisford, & Basit, 2018; Jamróz, Szafraniec, Kurek, & Jachowicz, 2018):

- Reduced length and cost of transport and storage (Boon & Van Wee,
 2018);
- Quick and real-time responses to patient and market needs due to the possibility to rapidly produce small batches of complex formulations with unique geometries (Manners-Bell & Lyon, 2012);
- Reduced waste and hence reduced costs of developing and dosing due to a precise spatial control over the deposition of materials, limiting the amounts of API (active pharmaceutical ingredient) and excipients in comparison to conventional technologies (Campbell, 2011).

Despite these benefits, there are several technical and regulatory challenges that need to be overcome before 3D printing can be widely used for pharmaceutical applications in clinical practice, as shown by only one FDA approval of a 3D printed drug on the market (Di Prima et al., 2016), and one on its way (Everett, 2021). In the industrial setting, a 3D printed product must comply with the current manufacturing and control standards for medical products and devices, specifically the well-established Good Manufacturing Practices (GMP). However, 3DP manufacturing has many more issues involving design and production, raw material storage and transport, quality control, risk of counterfeit production, etc.

From a regulatory point of view, there are still several open questions on how 3D-printed healthcare products can be monitored and evaluated for quality, with no possibility to give universal guidelines for all 3D-printed technologies and medical devices. A separate assessment of safety and effectiveness may be required for each technology and product, especially for the personalised ones. Furthermore, when products are customized for a patient, the question of whether 3D printing is classified as a manufacturing or compounding process also has a great impact on regulatory requirements (https://www.fda.gov/media/125479/download).

Overall, 3D printing has the potential to revolutionize the existing healthcare scenario, allowing not only the development of new drug delivery systems, but also the choice between centralized/decentralized manufacturing, customized/personalized medicines, and medical devices, and on demand/by market order request production.

1.3 3D printing: classification and technical aspects

To fully understand the high potentialities of 3D printing approach, as well as the motivations that cause the actual regulatory difficulties, it is essential to analyse this new production technologies from a strictly technical point of view.

The term 3D printing is defined by International Standard Organization (ISO) as the "fabrication of objects through the deposition of a material layer-by-layer using a print head, nozzle, or another printer technology" (Jamróz et al., 2018). The term 3D printing means subset of a wide variety of techniques able to precisely produce freeform solid objects of a high degree of complexity

starting from digital models created with computer aided design (CAD), ensuring great fidelity, reproducibility, and cost-effectiveness (Gao et al., 2015).

In fact, the Additive manufacturing production process have been considered as a complex series of stages, from the digital design of the object to the slicing manipulation (that means the split of the model in a multi-layer structure), to the layer-by-layer building phase, and finally to the post-processing stage (Figure 1.4).

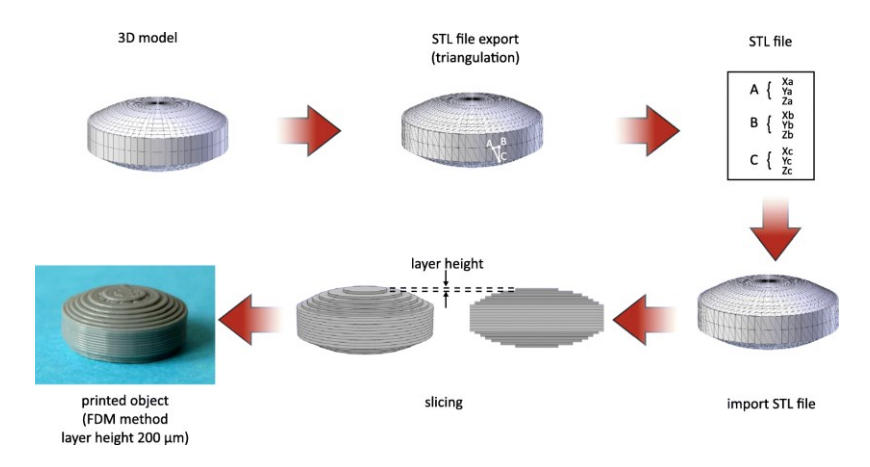


Figure 1.4 Additive manufacturing workflow (Jamróz et al., 2018)

In fact, the FDA gave the Section V of the FDA guidelines "Design and Manufacturing Considerations", to technical considerations that should be addressed as part of fulfilling Quality System (QS) requirements for your device. In detail, the quality requirements of each step of additive manufacturing process are described from the file format conversation, to the starting material preparation, as well as the management of material reuse

(https://www.fda.gov/regulatory-information/search-fda-guidance-documents/technical-considerations-additive-manufactured-medical-devices).

According to the American Society for Testing and Materials (ASTM F2792-12a), AM processes can be classified in seven categories, namely: (1) material jetting, (2) binder jetting, (3) vat photopolymerization, (4) powder bed fusion, (5) material extrusion, (6) energy deposition, and (7) sheet lamination (ISO/ASTM52900, 2021) (Figure 1.5).

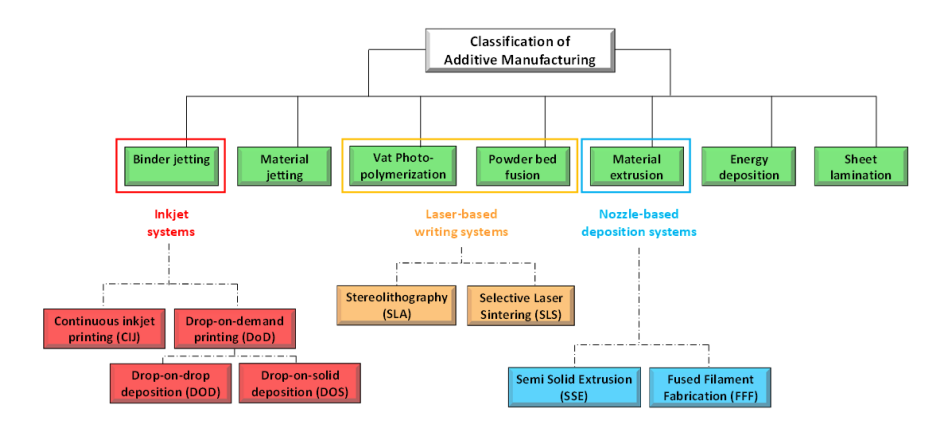


Figure 1.5 Schematic view of 3D printing technologies according to ISO/ASTM 52900 classification

Further AM classifications may be done based on the physical state of the starting material used to form the product (solid, liquid, and powder-based processes), or even the medium used for its processing (laser beam, ultraviolet rays, thermal means, etc.) (Saleh Alghamdi, John, Roy Choudhury, & Dutta, 2021). A commonly accepted classification of the different 3DP systems used for pharmaceutical and medical applications is based on three main groups (Goole & Amighi, 2016; Mohapatra, Kar, Biswal, & Bindhani, 2022), namely:

1.3.1Printing based ink-jet systems

The idea of "ink-jet" systems originated from computer-operated ink-jet printing, which recreates digital images by propelling ink droplets onto paper. This was adapted for pharmaceutical application by the replacement of the ink with liquid solutions containing APIs and excipients, and paper with edible paper-like sheets known as substrates. In this case, the major challenge, often underestimated, is the formulation of an API-containing ink with appropriate properties. Specifically, during a generic inkjet-based 3DP process, the ink must be sprayed at a set speed, and through specific motions, into droplets with precise sizes. Operative conditions must be well established to facilitate reliable jetting and homogeneous droplet formation with minimal satellites (Barui, 2021). In addition, the choice of the solvent for the ink formulation, as well as the ink drying rate, could influence the solid state of the loaded API after deposition and hence its bioavailability (Hsiao, Lorber, Reitsamer, & Khinast, 2018). The ink-jet based 3DP technologies can be divided into two types: continuous (CIJ) and drop-on-demand (DoD) inkjet printing (Vaz & Kumar, 2021). In the first case, the ink is sprayed, mainly through piezoelectric crystals, in a continuous flow. On the contrary, during a DoD process, the ink flow, either provided by a thermal or a piezoelectric device, is provided only as needed. This latter process can be also defined as drop-on-drop deposition (DOD) if the drops are allowed to deposit on each other to form a bed and drop-on-powder deposition (drop-on-solid, DOS) if the droplets are allowed to deposit on the powder bed; this approach is also known as the TERIFORM® process.

1.3.2 Laser-based writing systems

The second set of 3DP technologies is that laser-based 3DP technologies. This group includes selective laser sintering (SLS), or selective laser melting (SLM), and stereolithography (SLA, the first 3D printing technology patented in 1984 by Charles Hull), for which the object is built by the solidification of photosensitive liquids. Many are the advantages and the disadvantages of such techniques. Ideally, almost any dosage form can be fabricated by SLS with a high level of precision, accuracy, and resolution. In fact, even objects of several cubic centimetres (and hence rather large) can be built with a resolution down to 0.2 micron (Kafle et al., 2021). SLS can be successfully applied to produce porous, rapidly disintegrating, as well as modified release dosage forms without binding agent, with high drug loading efficiency and good mechanical properties. However post-printing processing is required as the object is built into a powder, and such a step requires specific powder removal procedures and facilities. Other disadvantages are due to the risk of API decomposition after exposure to laser beam, the high variability of mechanical properties, and the limited speed for sintering (Jamróz et al., 2018)

1.3.3 Nozzle-based deposition systems

The third group of 3D-printing technologies is represented by nozzle-based deposition systems allowing direct writing through extrusion. Such systems deposit ink direct through a nozzle to create a 3D pattern layer-by-layer with controlled composition and architecture (Park et al., 2019). They can be basically divided into processes based on material melting, such as fused filament fabrication (FFF), also referred to as fused deposition modelling (FDM), and processes not involving material melting, such as Semi-solid extrusion (SSE), also known as pressure-assisted microsyringe (PAM) (Figure 1.6).

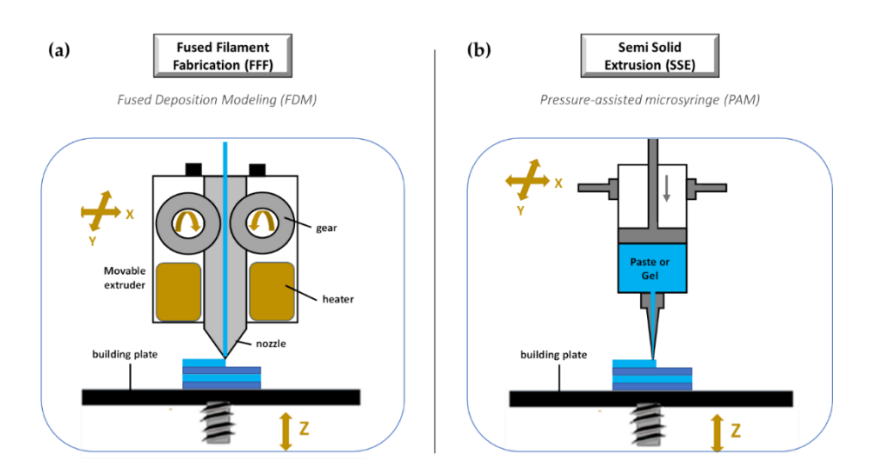


Figure 1.6 Illustration of Nozzle based techniques a) Fused Filament Fabrication, and b) Semi-solid extrusion

Nozzle based 3DP technologies have been highly investigated, thanks to their great versatility, reproducibility, and high scalability potential, combined to cheap processing costs. A lot of recent scientific papers deepened the discussion on the application of such techniques to develop pharmaceutical and biomedical products.

1.3.3.1 Fused Filament Fabrication (FFF)

FFF is a very investigated 3DP technique because it is cheap, easy to use, and readily available (Alhijjaj, Belton, & Qi, 2016; Park et al., 2019). Its increasing popularity is mainly due to the progressive availability of compact sized and relatively inexpensive equipment (Jamróz et al., 2018; Vaz & Kumar, 2021). During a FFF process, a thermoplastic polymeric material (mainly in form of filament) is extruded through a warmed-up nozzle and printed layer-by-layer (Figure 1.6a). Nozzle diameter varies from 0.2 to 0.4 mm, and it has an impact on the final resolution of 3D printed product. Generally, the width of the printed path corresponds to the nozzle diameter, while its height is equal to the half of the width. However, properties of the selected starting material as well as printer settings may induce modifications. During the process, the paths are arranged in layers until the formation of the final object, the resolution of which depends on layer height. Differently, the mechanical characteristics of the printed product are related to a number of outlines that build the external wall of the object and infill pattern (e.g., linear, or hexagonal).

The development of dosage forms and medical devices by the FFF approach requires a deep understanding of the printing process parameters as well as a thorough formulation study to properly select raw materials. Several critical

material requirements need to be considered for their influence on FFF processability as well as on the 3D printed product quality. In more detail, filament mechanical properties (e.g., elastic modulus and strain at yield) and viscosity at the melted state mainly influence the extrusion step. Rheological properties, and particularly viscosity, surface tension, and relaxation dynamics, have impact above all on layer and intralayer adhesion, and thus on object precision and resolution. Finally, thermal properties (e.g., conductivity, heat capacity, coefficient of thermal expansion, and crystallinity), besides specifically driving process parameter set-up, are often responsible for fibre shrinkage and warpage (Tan, Zhu, & Zhou, 2020). Therefore, the careful evaluation of such aspects may avoid processing issues (Jamróz et al., 2018).

In general, the main disadvantages of FFF rely in the poor choice of starting materials which, as introduced, is limited to thermoplastic polymers, and the need of preparing drug-loaded filaments in advance. Moreover, due to the elevated temperatures associated with this process, the potential risk of drug degradation is a significant issue hindering its use in pharmaceutical field.

1.3.3.2 Semi-solid extrusion (SSE)

Differently from FFF, the SSE process involves a semi-solid starting material (in the form of gel or paste) that is extruded through an orifice by compressed air pressure, a syringe plunger, or screw, depending on the specific equipment used, and deposited layer by layer (Figure 1.6b) (Awad, Trenfield, Goyanes, Gaisford, & Basit, 2018). Semi-solid materials can be easily obtained

by excipients commonly employed in the pharmaceutical industry by mixing them in with appropriate solvent(s) to obtain a viscosity range suitable for printing. In fact, several studies underlined the relevance of ink's rheological characterization to ensure the success of the printing process (Schwab et al., 2020). SSE does not require high temperatures but, using materials in form of pastes or gels, a further drying process is needed, implying shrinking or deformation of the printed product (Gutierrez et al., 2019). The fabricated object may also collapse during 3D printing if a constructed layer did not harden sufficiently to withstand the weight of the successive layer. The technique is usually confined to a low resolution since an orifice with a size of 0.4–0.8 mm is typically employed. However, an accurate parameterization of the dispensing of the semi-solid mass, as well as the use of nozzles smaller in diameter, allows to obtain dosage forms with a good resolution and mass uniformity (Basit & Gaisford, 2018; Elbadawi et al., 2021). The main advantage of SSE resides in the possibility to fabricate dosage forms with high drug loading. By using multi-syringe printing, "polypills" may also be obtained containing 3–5 APIs released with different kinetics (Khaled, Burley, Alexander, Yang, & Roberts, 2015a, 2015b).

The data shown earlier indicate that each 3DP approach presents specific advantages and disadvantages and suggest the choice that must be made based on the properties of the starting materials as well as the drug to load and the

desired performances for the final 3DP products, without forgetting system cost-effectiveness and realizable scale-up.

To give the reader a rapid comparison and insight into the different available techniques, the above discussed topics are summarized in Table 1.1

Table 1.1 Comparison of Nozzle based 3D printing techniques

FFF	Thermoplastic polymers (mainly in form of filaments), e.g., PVA, PLA, PLGA, PCL, TCP, HPC, Eudragit, HPMCAS, Soluplus®, etc.	 Cheap, widely available, compact, and easy to use equipment High speed Medium resolution Very good accuracy Good mechanical properties High quality High drug uniformity No need for post-printing Optimum in term of design complexity Used for a wide range of thermoplastic materials 	■ Poor surface finish
SSE	Semi-solid mixture of polymers and solvents It allows the use of the most types of excipients used in pharmaceutical technology such as HPMC, HPC, PVP, MCC, etc.	 Cheap, readily available, and easy to use Low temperature process (suitable for thermolabile drugs) High drug loading (up to 90%) Large choice of starting materials Multi-material printing Ability to manufacture drug loaded devices with multi-release modo 	 Low drug loading Difficult to scale up Use of organic solvents Limited resolution (depending on nozzle size) Need for post-processing (e.g., drying) Low efficiency Low mechanical properties (low hardness and high friability) Need for sufficiently viscous semi-solid materials

	 Difficulty to control the flow of semi-solid materials through the nozzle
	■ Risk of nozzle clogging

1.4 Semi-solid extrusion 3D printing: focus on potentialities and issues in pharmaceutical technology

SSE technique is attracting the attention of pharmaceutical researcher to produce various pharmaceutical dosage forms, different types of tablets, and polypills (e.g., loaded with single API or multiple APIs, floating, orodispersible or chewable), many of which for paediatric requirements (Figure 1.7).

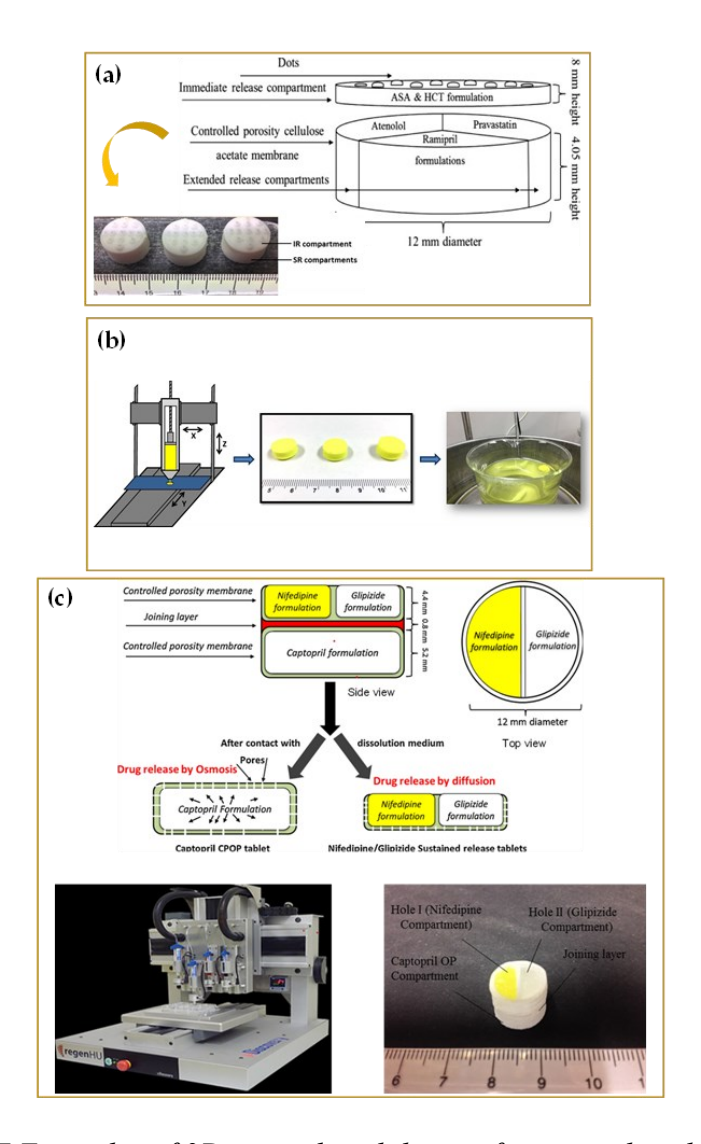


Figure 1.7 Examples of 3D printed oral dosage forms produced by SSE technique. (a) Polypill loaded with five different APIs (Khaled et al., 2015a); (b) Gastro-floating tablets of dipyridamole. (Li et al., 2018); (c) Polypill designed as an osmotic pump containing captopril, and with other two compartments acting as sustained release platforms for nifedipine and glipizide (Khaled et al., 2015b)

The first application of SSE printing process for DDS production was a fivein-one polypill with strictly controlled drug release, that was designed by Khaled et al. in the 2015 (Khaled et al., 2015b). They developed a novel tablet with a complex geometry able to deliver five APIs with two independently well-defined release profiles. The first three compartments were designed to release in a sustained manner pravastatin, atenolol, and ramipril. The combination of such drugs in a single polypill for the prevention and treatment of cardiovascular diseases allows to optimize therapy as well as patient compliance while avoiding incompatibility issues thanks to the physical separation of each drug within the compartments.

SSE has also been exploited for the fabrication of gastro-floating tablets to improve the bioavailability, and thus therapeutic efficacy of some drugs. Li et al. (Li et al., 2018) successfully developed gastro-floating tablets with a fine lattice internal structure loaded with dipyridamole, a poorly water-soluble drug with a short biological half-life. Tablets were prepared starting from pastes of hydroxypropyl methylcellulose (HPMC K4M) and hydroxypropyl methylcellulose (HPMC E15), two traditional pharmaceutical excipients, and applying three different infill percentages (30%, 50%, and 70%).

SSE would be an important tool in personalizing paediatric formulations. Indeed, the number of papers reporting the use of SSE 3DP in the manufacturing of paediatric-friendly chewable printlets for the oral administration of both hydrophilic and lipophilic drugs is growing. Goyanes et al., for example, evaluated for the first time the use of SSE 3D printing in a hospital setting for the administration of isoleucine in the form of personalized

chewable printlets to treat a rare metabolic disorder, maple syrup urine disease (MSUD), in paediatric patients (Goyanes et al., 2019). Isoleucine blood levels after six months of treatment with personalized chewable formulations prepared at the hospital by automated 3D printing were comparable to those obtained with conventional capsules prepared by manual compounding. However, the 3D printlet therapy caused mean levels closer to the target value and less variability. As regards acceptability, 3DP formulations prepared with different flavours and colours were well accepted by the children, although each patient had different preferences.

Personalized chewable medicines for children were produced *via* Semisolid extrusion in the form of gummies with different shapes too, e.g., heart, bear, or disc, loaded with paediatric doses of ranitidine hydrochloride (Tagami et al., 2021). In this case, a syringe-based extrusion mechanism used mixtures of gelatin, carrageenan, xanthan gum, and sweeteners (Herrada-Manchón et al., 2020). Mass as well as dose uniformity were guaranteed, fitting standards that only well-established tableting technologies can reproduce. The added value of the personalized paediatric formulations resides in the easy handling and intake, high dosage flexibility, and personalization of the final products by simple changing the size, infill density, or design of the digital model. Moreover, the attractive, funny, and appetizing appearance of the gummies could enhance treatment adherence and help to decrease the emotional impact of the disease in children.

Recently, LegoTM-like chewable bricks made of edible soft material (gelatin-based matrix) were also proposed by a variant of SSE, namely embedded three-dimensional printing (e-3DP). E-3DP implies the extrusion of semi-solids within a solidifying liquid matrix (Rycerz et al., 2019). Such chewable dosage forms with dual drug loading (paracetamol and ibuprofen) were produced by directly extruding novel printing patterns of model drug ink (embedded phase) into a liquid gelatin-based matrix (embedding phase) at an elevated temperature (70 °C), followed by solidification at room temperature. The main advantage of this technology is the possibility to encapsulate the drug paste within a matrix that masks its flavour, as in the case of bitter-tasting drugs.

One more application of SSE is in printing lipid-based formulations (LBFs) loaded with poorly water-soluble APIs into solid oral dosage forms for the delivery of poorly water-soluble APIs (Real, Barberis, Camacho, Bruni, & Palma, 2020). Johannesson et al., for example, used SSE to produce solid lipid tablets based on printable emulsion gels with appropriate rheological properties by the addition of methyl cellulose as viscosity enhancer (Johannesson, Khan, Hubert, Teleki, & Bergström, 2021). Tablets loaded with fenofibrate were successfully 3D-printed, showing good mechanical and dimensional properties as well as high mass uniformity and dose accuracy. Moreover, as expected for immediate release formulations, the produced tablets were able to disintegrate in less than 15 min. The combination of the

advantages of an established formulation strategy for poorly water-soluble drugs as LBFs with such a novel and flexible production technique as 3DP via SSE opens new horizons to delivery highly potent, poorly water-soluble APIs for which dose adjustments may be required in some patient categories.

ODFs (orodispersible films) may be manufactured by SSE (Elbl, Gajdziok, & Kolarczyk, 2020; Sjöholm & Sandler, 2019; Tian et al., 2019). ODFs are polymeric thin film strips loaded with drugs that rapidly dissolve upon contact with saliva (Visser, Wibier, Mekhaeil, Woerdenbag, & Taxis, 2020). SSE 3D printing in the production of such systems provides a very increased flexibility in terms of drug dosage as the drug dose can be established based on the dimensions of the ODF itself, representing a great advantage to realize a personalized pharmacotherapy. Yan et al. printed individualized ODFs in doses of 1.25 mg, 2.5 mg, and 5 mg of levocetirizine hydrochloride (Yan et al., 2020). HPMC was used as water-soluble and film-forming polymer, pregelatinized starch as filling agent, and maltitol and sucralose as flavouring agents. For this kind of application, the critical point is the careful selection of the relative ratios among such components to obtain a printable ink, that is a gel with consistency and viscosity suitable for 3D printing process. Whilst the main advantage resides in the drug content uniformity and dose accuracy, high flexibility, and rapid drug release performances (complete drug dissolution within 2 min).

The great potential of SEE 3DP for biomedical applications, and specifically for the manufacture of polymeric scaffolds incorporating thermolabile drugs, and hence requiring low process temperatures, has been recently evidenced. Naseri et al. reported a novel low-temperature (20 °C) 3D printing technique based on SSE poly-lactic-co-glycolic acid scaffolds using methyl ethyl ketone (MEK) as a mild organic solvent (Naseri, Butler, MacNevin, Ahmed, & Ahmadi, 2020). In this paper, the printability study of PLGA scaffolds was performed on different starting bio-inks obtained by varying the PLGA concentration in MEK solvent, lactic to glycolic ratio, and molecular weight of PLGA. For 3DP via SSE of PLGA scaffolds with high shape fidelity, good flexibility, and elasticity, the authors recommend PLGA concentrations higher than 80% w/v, lactic to glycolic ratio greater than 75%, molecular weight more than 100-200 kDa, and printing through nozzles smaller than 0.96 mm in internal diameter.

1.5 Alginate-based hydrogels, increasing interest for the 3D printing application

Alginate, thanks to its biocompatibility, and biodegradability, is one of the most versatile polymers, which is used in a wide range of field from food industry, to biomedical as well as pharmaceutical field, and more recently in the 3D printing.

Alginate is a natural polymer obtained from the extracellular matrix of seaweed. specifically, the brown type of algae (i.e., *Laminaria hyperborea*, *Macrocystis pyrifera*, and *Ascophyllum nodosum*).

From a chemical point of view, alginate is a linear unbranched polysaccharide containing varying proportions of β -D mannuronic (M) and a-L-guluronic acid (G) residues that are 1,4-linked by glycosidic bonds-forming homo polymeric MM or GG blocks, which are interspersed with hetero polymeric MG or GM blocks (Figure 1.8) (Liew, Chan, Ching, & Heng, 2006).

Figure 1.8 Structure of β -D mannuronic (M) and a-L-guluronic acid (G) residues 1,4-linked by glycosidic bonds

Proportions of blocks in alginate (M/G ratio), as well as the chain length affect the physico-chemical properties of alginate (Skaugrud, Hagen, Borgersen, & Dornish, 1999). Alginate is an ideal candidate for chemical functionalization as it has several free hydroxyl and carboxyl groups distributed along the backbone, the properties such as solubility, hydrophobicity and physicochemical and biological characteristics may be modified by forming alginate derivatives through functionalizing available hydroxyl and carboxyl groups (Yang, Xie, & He, 2011). Various chemical or

physical methods such as grafting copolymerization, polymer blending and compounding with other functional components can be used to modify sodium alginate (Balakrishnan & Jayakrishnan, 2005; Coleman et al., 2011; Thakur & Arotiba, 2018). Among the large range of polymers, alginate shows as peculiar characteristic, the pH-sensitive gel-forming ability, that allow to obtain at the end of polymer hydration high viscous gels (Chan, Ching, Liew, & Heng, 2007). Alginate has carboxyl groups which are charged at pH values higher than 3-4, making alginate soluble at neutral and alkaline conditions (Cardoso, Costa, & Mano, 2016). In the presence of multivalent cations alginate forms stable reversible hydrogels with variable gelling homogeneity and strength. In fact, gelling depends on ion binding (Mg $^{2+}$ < Ca $^{2+}$ < Zn $^{2+}$ < Sr $^{2+}$ < Ba $^{2+}$) (Reis, Neufeld, Vilela, Ribeiro, & Veiga, 2006). The egg-box formation is the most popular model used to describe this interaction between alginate chain and cations (Braccini & Pérez, 2001). In detail, as demonstrate by Mørch et al the alginate bonds are prevalent due to the G blocks interactions, consequentially robust hydrogel can be engineered by using a G-rich alginate (Mørch, Donati, Strand, & Skjåk-Bræk, 2007). In a study published by Fang et al. the entanglement between alginate and calcium ions was investigated highlighting three different kind of structure from monocomplexes, to the egg-box dimers and finally laterally associated egg-box multimers (Fang et al., 2007)

Concerning the pharmaceutical application of alginate, it is used in a large range of traditional and innovative formulations such us tablets, beads, nanoparticles, and microsphere (Draget, Skjåk-Bræk, & Smidsrød, 1997). It may use as carrier matrix for biomolecules or APIs (Auriemma et al., 2020), as well as excipient for local administration (Amante et al., 2021), or as functional excipient able to modulate the release-rate (Boontheekul, Kong, & Mooney, 2005). Thanks to the high potentialities of alginate hydrogels, they are attracting a lot of attention in various fields, and countless research are being done in several field (Grøndahl, Lawrie, Anitha, & Shejwalkar, 2020; Hariyadi & Islam, 2020). Among the innovative application of alginate hydrogels, there is certainly their potential use as ink for 3D printing process (Axpe & Oyen, 2016). Indeed, the versatility of alginate for 3D printing is highly restricted and limited due to issues related with structural collapsing and shape fidelity (Gutierrez et al., 2019; Hazur et al., 2020). In fact, alginate hydrogels are characterized by low viscosity and weak mechanical performance in comparison to the 3D printable inks commercially available (such as Pluronic acid); for these reasons the preparation of complex structure and high-fidelity printouts is difficult. Moreover, the spreading after the extrusion on the build-plate and low matter content negatively affect the shape retention of extruded forms after printing and after drying, respectively (Leppiniemi et al., 2017).

To date, the mainly 3D printing use of Alginate-based materials is in the 3D bio-plotting to prepare the tissue equivalents (Axpe & Oyen, 2016). In these cases, the printability issues of alginate were counteract using chemical

derivates of alginate or more often mixing the alginate with other polymers or micro/nano composites (Erol-Taygun, Unalan, Idris, Mano, & Boccaccini, 2019; Leppiniemi et al., 2017). In 2021 Mallakpour et al in published an Historical Perspective review that resumed in detail the state-of-art of 3D printing technology of alginate-based hydrogels (Figure 1.9) concluding that "The development of perfect alginate-based bio-ink is yet in progress. However, due to the extensive contributions all over the world, it could be possible for applying this alginate-based system for industrial purposes in the near future" (Mallakpour, Azadi, & Hussain, 2021).



Figure 1.9 Fields of 3D printed alginate materials applications (Mallakpour et al., 2021)

However, analysing the Mallakpour's review, it is possible to highlight that the 3D printing application of alginate hydrogels in the pharmaceutical field is almost uncharted. Considering these premises, the lack of knowledge in the use of alginate based gels in SSE 3D printing can be considered the starting point of this research project.

Section 1

Extemporaneous gelation of alginate in coaxial Semi-solid extrusion 3D printing process: development of innovative 3D printed platforms

Based on the Article

Falcone, G., Saviano, M., Aquino, R. P., Del Gaudio, P., & Russo, P. (2021). Coaxial Semi solid extrusion and ionotropic alginate gelation: A successful duo for personalized floating formulations via 3D printing.

Carbohydrate Polymers, 260, Article 117791.

https://doi.org/10.1016/j.carbpol.2021.117791

2.1 Scientific background & Research aim

The limited use of the SSE in the production of drug products is related to both the lack of study on the printability of drug-loaded gels, and the critical step of post-processing after printing. In fact, the number of works nowadays present in literature are limited (Goyanes et al., 2019; Khaled, Burley, Alexander, & Roberts, 2014), and particularly, focusing on floating SSE prints, only infill geometries or binding agents have been used to modulate the buoyancy behavior (Li et al., 2019; Wen et al., 2019). In this research, we hypothesized that the ionotropic gelation of SA in a coaxial Semi-solid

extrusion printing technique, would lead to novel drug delivery systems (DDS) without further chemical post-processing or crosslinking. Moreover, the suitable pumping of the two different feeds into the coaxial extruder in the right configuration in/out should make those DDS able to float. Particularly, the selected fluids were the SA gel (named alginate ink) and a hydroxyethyl cellulose (HEC) gel (Dai et al., 2019) containing the crosslinking agent Ca²⁺ (named crosslinking ink). Finally, theorising the application of this single-step manufactured DDS in the personalized therapy, the addition of Propranolol Hydrochloride into the SSE formulations was carried out.

2.2 Materials & Methods

2.2.1 Materials

All materials involved in the printing process as well as in the characterization of printouts were used as received unless otherwise noted: sodium alginate (SA) European Pharmacopoeia X with β-d-mannuronic:β-l-guluronic acid ratio of 1.3, MW > 200000 g/mol, and 1% aqueous solutions viscosity 65 mPa·s (CAS 9005-38-3, Carlo Erba, Milano, Italy); hydroxyethyl cellulose (HEC) high viscosity (2100 mPas of 1% aqueous solutions), with a degree of substitution of 1.5 (3 hydroxyls substituted/2 units)(CAS 9004-62-0, ACEF, Italy), calcium chloride (CaCl₂, CAS 10043-52-4, VWR International, Milano, Italy), Tween® 85 (Tw, CAS 90005-70-3, Sigma-Aldrich);

Propranolol Hydrochloride (Prp) (CAS 318-95-9, Farmalabor, Milano, Italy); Hydrochloric acid 37% w/w (ACS reagent, CAS 7647-01-0, Sigma-Aldrich, Italy); Sodium Phosphate (CAS 7601-54-9, Sigma-Aldrich, Italy).

2.2.2Methods

2.2.2.1 Inks spreading measurement

Following the literature information about the spreading of hydrogel drops or extruded filament that negatively affect the final resolution of printouts (Paxton et al., 2017), a method was developed to evaluate the spreading angle. The spreading angle was described as " θ values" (i.e., left and right angle values between the extruded gel filament and the build plate. In detail, to evaluate the spreading angle of inks, pictures of ink's drop on the build plate were taken after the extrusion and were analysed exploiting the manual point procedure of ImageJ software.

2.2.2.2 Dynamic viscosity measurement

For the alginate inks (SA from 4 to 6 % w/v), the dynamic viscosity (expressed in Pa *·s), was measured using the viscometer Visco Basic Plus (Fungilab, USA). The measurements were conducted at room temperature with L3 spindle and 50-1 rpm range. Instead, for all the crosslinking inks, the measurement was effectuated using Visco Smart (Fungilab, USA) with R6 spindle and 100-20 rpm range. For all the analysed samples, at least seven measurements were acquired at intervals of 10 seconds and 1 minute.

2.2.2.3 DDS Digital optimization & SSE printing process

The .stl files of toroidal geometries, selected for the formulations, were processed using the slicing software Cura 4.3.0 (Ultimaker) and sent to the printer as. gcode. The digital dimensions of the printouts are shown in Table 2.1

Table 2.2 Size of the digital model with toroidal geometries

Toroidal models	External diameter (mm)	Internal diameter (mm)	Height (mm)	Number of layers	Graphical representation
Drug-free formulations	13.00	7.00	11.75	3	

The platforms were produced using lab made coaxial extruder connected through tubes to a syringe pump system, Fusion 4000 (Chemix Inc., UK). In particular, the extruder was designed in size and dimensions along XY axes for a perfect installation on the Ultimaker3 printhead and into the radial/axial fans bracket, without hampering the normal movement of the printer using the (CAD) software Rhinoceros 6. CAD models were exported stereolithographic files (.stl) and then processed via the slicing software Cura 3.2.1 (Ultimaker, Netherlands). The material selected for the extruder production was the Polylactic acid (PLA) which allows the creation of highresolution parts with good surface quality and good mechanical strength. The holes for the insertion of the two feeding tubes were designed to fit with them (tubes with a diameter of 3 mm), while the exit holes were designed for a satisfactory resolution of SSE extrusion, considering the viscosity of the processed inks. The printed extruder was fixed on the printhead of the Ultimaker³ printer to exploit its movements along the axes, while the extrusion occurs (Figure 2.1). Specifically, the two gels were loaded in two separate syringes (12.25 mm diameter) to feed the inner and outer channels simultaneously at the same flow rate (150 μ L/min; print speed for blank forms 0.25 mm/s; drug-loaded forms 0.225 mm/s). SSE printing took place, with no need to heat the nozzle, and following the concentric geometry of the drawn toroidal models. The printing parameters were optimized using as initial layer height 3.75 mm, and then a layer height of 4 mm.

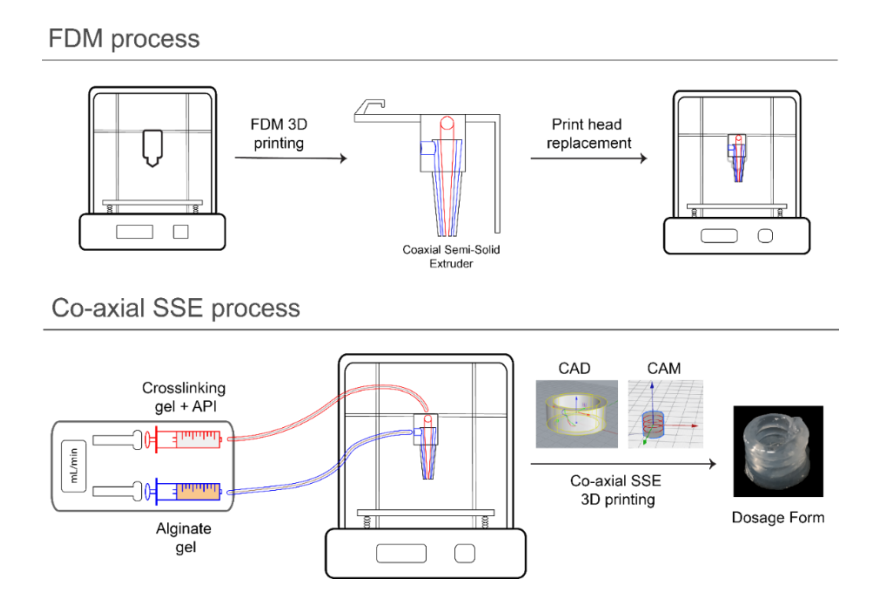


Figure 2.1 Schematic representation of the co-axial printing process

2.2.2.4 Printing resolution and process reproducibility

To investigate the resolution and reproducibility of the manufacturing processes, for all the produced batches the mass and the dimension (diameter "D" and height "H") were analyzed during both steps: post-printing and post-drying. In detail, at least six printed units for each formulation were accurately weighed by digital analytical balance (MX5 micro-balance, Mettler Toledo, Germany) both after printing and after drying. The results of post-printing mass were reported as absolute values (g) with standard deviation; while, for post-drying mass evaluation, the results were showed thanks to the following equation:

$$M_d$$
 (%) = $\frac{Mass\ after\ drying\ (mg)}{Mass\ after\ printing\ (mg)} * 100$ (Eq 2.1)

Where M_d is the mass variation after drying.

Similarly, the dimensions were analyzed after both steps by digital caliper. the acquired data were used to calculate the process resolution and reproducibility. For the evaluation of shape fidelity after printing, the data were compared to the digital dimensions exploiting the equation reported below:

$$D_p (\%) = \frac{D_{Printed model}}{D_{Digital model}} * 100$$
 (Eq 2.2)

$$H_p (\%) = \frac{H_{Printed model}}{H_{Digital model}} * 100$$
 (Eq 2.3)

While, to highlight the impact of drying process on the shape fidelity, the dimension after drying were related to the dimension after printing

$$D_d (\%) = \frac{D_{Dried \ model}}{D_{Printed \ model}} * 100$$
 (Eq 2.4)

$$H_d (\%) = \frac{H_{Dried \ model}}{H_{Printed \ model}} * 100$$
 (Eq 2.5)

2.2.2.5 Drying process

Following the aim to overcome the need to subject the printouts to curing process, it was investigated the impact of drying process post-printing. The drying methodologies for printouts were carried out on F6_0.1 batch. In detail, the processes applied were:

- air drying, with storage at room temperature until constant weight was obtained.
- microwave-assisted drying at 200 W for 15', 300 W for 10' or 400 W for 5'.
- oven drying at 40°C until constant weight was obtained, about 7 hours.
- vacuum drying with vacuum cycles every 30' for 6 hours and then overnight in desiccator.

2.2.2.6 Morphological Analysis

The printed systems were photographed with a single lens reflex camera (Canon EOS 600D; parameters: f-stop: f/6.3, shutter speed: 1/5 s, ISO 200). Optical microscopy (Alphaphot-2 YS2, Nikon, Japan), with an objective 4X, was used to acquire images of dried layers details. The platforms were also observed by Scanning Electron Microscopy (Tescan Solaris, Tescan Orsay Holding, Czech Republic) to obtain information about inner microarchitecture

of Ca⁺⁺- alginate matrix; while the drug-loaded DDS were observed to highlight the API distribution in the polymeric matrix

2.2.2.7 Buoyancy tests and DDS density

Buoyancy tests were performed gently placing the dried formulations in acidic dissolution medium prepared according to the method proposed by USP 36 (dissolution 0.1M HCl solution; pH 1.2 ± 0.5). The medium was in constant stirring at 70 rpm and at 37 ± 0.5 °C. The lag time before the buoyancy and the floating time of the single samples were visually evaluated and reported in hours. The buoyancy properties were related to the density, the latter was determined matching the mass after drying to the volume of the printouts.

2.2.2.8 Media induced matrix behaviour (medium up-take test)

To investigate the main processes that lead to the matrix disintegration, all batches (at list minimum 3 samples for each one) were subjected to in vitro test using a USP dissolution Apparatus II, in paddle configuration (70 rpm) (AT7 Smart Dissolution Tester, Sotax Corporation). In detail, the changes in the DDS mass during the residence in gastro (pH 1.2 ± 0.5) simulated fluids at 37 ± 0.5 °C were examined. At specific time points, samples were withdrawn from the vessel, deprived of the medium excess, and weighed using analytical balance. The mass acquired was calculated in percentage following the equation reported below.

$$\textit{Mass Acquired (\%)} = \frac{\textit{Platoform mass (ti)-Dried Platform mass}}{\textit{Dried Platform mass}} *100 \quad (Eq~2.6)$$

Where Platform mass (ti) means the mass value at specific time from 0 to 300 min

2.2.2.8 FT-IR analysis

FT-IR analysis was carried out using FT-IR spectrophotometer (Spotlight 400N FT-NIR Imaging System, Perkin Elmer Inc, USA) equipped with an ATR accessory (ZnSe crystal plate) to detect any changes in the drug structure during the printing and drying processes. All the analysed samples i.e., powders, films and printed layer particles were analysed using 128 scans and 1 cm-1 resolution step in the spectral range of 4000-600 cm-1.

3.2.2.7 DSC Thermal Analysis

The differential scanning calorimetry were performed by DSC 822e (Mettler Toledo, Germany) and the results were processed by Mettler Toledo STARe software.

The analytic protocol involved the use of 40 μ L predrilled aluminium pans filled with a standard mass of materials (3-5 mg). The samples were analysed in form of powders, films, and printed layer particles. The thermal cycle selected included three segments, a dynamic from 25 °C to 100 °C at a heating rate of 50 °C/min, an isothermal at 100 °C for 10 min (to remove the residual water from the samples) and finally a dynamic from 100 °C to 350 °C at 10 °C/min. The latter was reported as thermograms.

2.2.2.9 Drug content analysis and drug-loading efficiency

All the Prp formulations ($n \ge 3$) were evaluated for drug content (DC) and drug loading efficiency (DLE) values.

The DLE (Eq.) has been calculated as:

DLE (%) =
$$\frac{Mass\ of\ PrpHCl\ observed\ (mg)}{Mass\ of\ PrpHCl\ predicted\ (mg)} * 100$$
 (Eq 2.7)

and the DC (Eq.) according to:

$$DC$$
 (%) = $\frac{Mass\ of\ PrpHCl\ observed\ (mg)}{Mass\ of\ dryed\ formulation\ (mg)} * 100$ (Eq 2.8)

The Prp content was obtained by UV-vis Spectrophotometer (Evolution 201 UV-vis Spectrophotometer, Thermo Fischer Scientific Inc.) setting the wavelength (λ) at 288 nm and using PBS (pH 6.8) calibration curve (concentration range: from 10.3 μ g/ml to 63 μ g/ml).

2.2.2.10 Dissolution tests

Dissolution tests were performed with USP dissolution Apparatus II (AT7 Smart Dissolution Tester, Sotax Corporation): paddle or basket configuration (Figure 3.2), 70 rpm stirring, 37 °C, using as dissolution medium gastric (pH 1.2 ± 0.5) simulated fluids, according to USP 36.

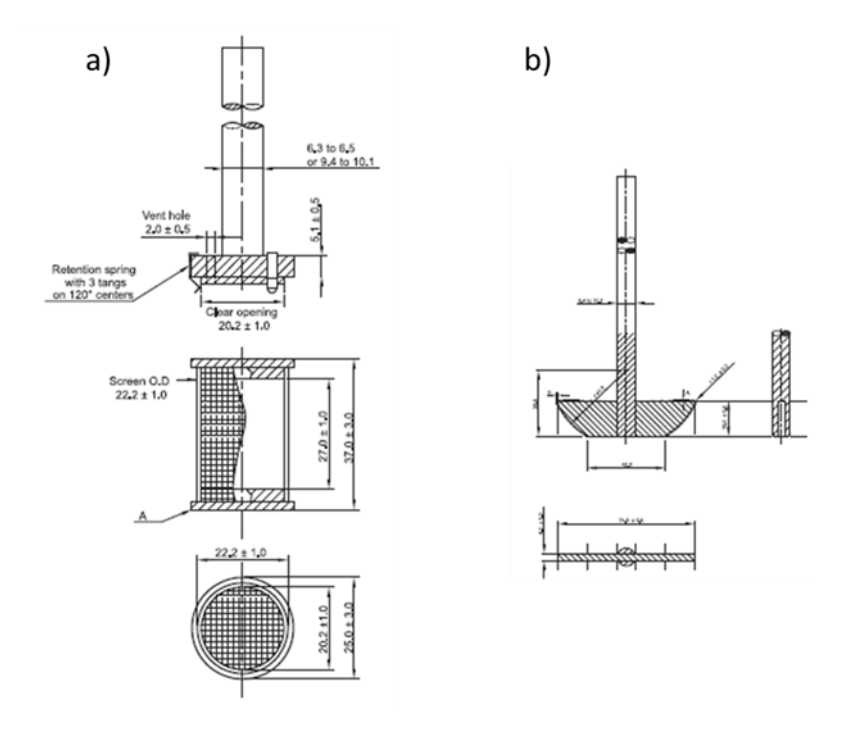


Figure 2.2 Graphical representation of a) basket configuration, and b) paddle configuration [European pharmacopoeia 8 Ed 2013]

For all drug loaded batches, the absorbance values (λ =288 nm), at different times were measured and related to the API acidic calibration curve (in a range of concentration from 10.5 μ g/ml to 65 μ g/ml). For all batches analyzed, mean values and standard deviations were reported.

..2.2.11 Release kinetics fitting studies

Fitting analysis on the release data was performed by using two different kinetic models to clarify release mechanism of the different formulations in accordance with the method proposed by Del Gaudio and collegues (Del Gaudio et al., 2015) in fact, both the Higuchi's model (Eq. 3.8) and Peppas-Korsmeyer's equation (Eq. 3.9) were used.

Higuchi's model is one of the most used to investigate pure Fickian transport, when pure diffusion is the main driving force of the release (Higuchi, 1961)

Higuchi:
$$M_t = A\sqrt{D(2C_0 - C_S)t}$$
 (Eq 2.9)

where Mt is the drug cumulative amount released at time t, t is time, A is the surface area, D the diffusivity of the drug through the matrix, and C0 and Cs are the initial drug concentration and drug solubility, respectively.

The Peppas-Korsmeyer's equation (Ritger & Peppas, 1987) used to mainly explain complex release mechanisms where diffusion is coupled with erosion or swelling of the matrix:

$$Peppas - Korsmeyer: \frac{M_t}{M_{mo}} = kt^n$$
 (Eq 2.10)

where $M\infty$ is the drug amount released at infinity, k is a constant, and n is a diffusion coefficient, which depends on geometry of the system and on the release mechanism. When pure diffusion controls the release mechanism n=0.5, whereas when n=1 the release is mechanism is dominated by a case II transport and Eq. 3.10 turns into a zero-order kinetic.

2.3 Results and discussion

Two different gels, (referred to alginate ink and crosslinking ink) were prepared (using bid. Water as solvent) and their composition were

characterized and optimized. In order to identify the range of concentrations of SA, CaCl2 and HEC allowing for good self-standing behaviour after extrusion, the shape retention angles (θ_L and θ_R) of alginate ink and crosslinking ink was monitored (Table 2.2). Angles under 90° were considered characteristic of printable gel with no spreading onto the plate; angles between 90° and 130° were distinctive of gels with limited spreading onto the surfaces; finally drops with angles over 130° had excessive spreading and consequentially were not printable. Particularly, it was possible to observe for all the gels analysed that the values of θ_L and θ_R of the same sample were comparable, demonstrating the good symmetry of the drops after deposition.

Table 2.3 Dynamic viscosity and angle values after extrusion of different alginate and crosslinking inks

in		inking ik	Alginate ink			Dynamic
CaCl ₂ (M)	HEC (% w/v)	Tw (% v/v)	SA (% w/v)		∂ _R (°)	Viscosity (Pa s)
0.5	3	-	-	76 ± 4	74 ± 4	41.5 ± 0.9
0.25	3	-	-	83 ± 11	82 ± 7	14.6 ± 2.7
0.25	3	0.1	-	79 ± 5	77 ± 7	14.1 ± 1.1
0.1	3	-	-	84 ± 7	84 ± 3	15.2 ± 2.3
0.1	3	0.1	-	79 ± 10	74 ± 8	12.7 ± 2.0
-	-	-	2	130 ± 5	125 ± 6	1.1 ± 0.1
-	-	-	3	117 ± 2	117 ± 3	4.5 ± 0.1
-	-	-	4	115 ± 6	115 ± 9	14.2 ± 0.2
-	-	-	6	105 ± 7	105 ± 7	54.7 ± 0.2

High amount of CaCl₂ caused an increase in the solution viscosity, nevertheless all the prepared crosslinking inks were extrudable by the pump. Moreover, they showed angles lower than 90°, underlining the possibility to freely change the cross-linker concentration (from 0.1 to 0.5M) to modulate ionotropic gelation, without affecting the shape retention of these gels. For alginate inks (SA column Table 2.2), despite the increase of concentration from 2 to 6% w/v, all θ_L and θ_R values were between 100° and 130°, with a lower accommodation after extrusion and deposition for the more concentrated gels. Furthermore, as expected, by increasing the concentration of SA it was possible to observe an increase in dynamic viscosity which did not prevent its extrusion. As preliminary study to highlight the interaction between the feeds, two different configurations of extrusion were investigated: the alginate ink in the outer channel with crosslinking ink in the inner one and vice versa. The choice of channel in which inks were pumped affected the structure of the extruded product: pumping the alginate ink trough the inner channel the result after drying was a bulk filament, while if it was pumped in the outer channel a hollow filament was obtained. According with the aim to develop a new floating system the latter configuration was selected for all the experiments. Once the optimal ranges of concentration have been identified, in terms of shape retention and extrudability of gels (SA 4 and 6% w/v; HEC 3% w/v with CaCl₂ from 0.1 to 0.5M), printing tests were carried out by means of the coaxial extruder fed with different gel compositions, as reported in Table 2.3.

Table 2.4 Composition of both extruded inks and weight of blank DDS obtained

DDS	Alginate Ink	Crosslinking ink (HEC 3 %w/v)		Post-printing weight	Residual weight after drying (%)
	SA (% w/v)	CaCl ₂ (% (% v/v)		(g)	
F4_0.5	4	0.5	-	1.41 ± 0.14	8.90 ± 0.40
F6_0.5	6	0.5	-	1.57 ± 0.08	10.19 ± 0.41
F6_0.25		0.25	-	1.42 ± 0.10	8.24 ± 0.18
F6_0.25_0.1		0.25	0.1	1.42 ± 0.10	7.44 ± 0.31
F6_0.25_0.3		0.1	0.3	1.60 ± 0.28	8.2 ± 0.4
F6_0.1		0.1	-	1.41 ± 0.05	6.62 ± 0.29
F6_0.1_0.1		0.1	0.1	1.51 + 0.04	5.62 + 0.27

For the formulation F4_0.5, the poor shape retention of 4% w/v SA (as highlighted by θ_L and θ_R in Table 2.2) was balanced by the presence of a high concentration of CaCl₂ (0.5 M), speeding up the gelation rate of polymeric matrix. However, this gelation did not prevent the spreading onto the build plate of part of the outer alginate not involved in the cross-linking process. Hence, to counteract the leakage of the alginate solution onto the printing plate and to optimize the interaction between the two gels, the SA concentration was increased to 6% w/v, which showed a minimum value of θ_L and θ_R . However, F6_0.5 showed poor adhesion between layers due to the immediate hardening

of the filament negatively affecting the resolution of final product. Thus, CaCl₂ concentration was reduced to 0.25 M (F6_0.25) and 0.1 M (F6_0.1), leading to high-resolution printed products. The formulation with the lowest amount of crosslinker, F6_0.1, was selected for the reproducibility of the printing phase (Table 3.3) to carry out preliminary tests of drying processes. The microwave-assisted drying, regardless of the wattage and the time of the cycle, brought a general wrinkling of the alginate matrix (Figure 2.3). The separation of the layers and deformation of the toroidal structure were caused by the excessive rapid evaporation of water molecules during microwaving. The oven process browned the formulations, making them glassy and fragile in texture, thus not resistant to handling, and giving them a variable buoyancy behaviour. While the vacuum drying affected the hollow cavities of dried forms along the height, affecting the floating behaviour of the toroidal channelled filaments.

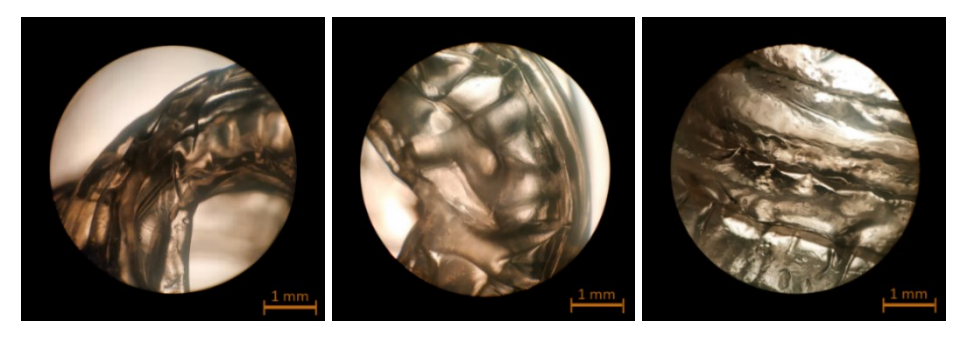


Figure 2.3 Optical magnification of the formulations F6_0.1 after the microwave assisted drying

Therefore, the selected process for all the produced batches was the air drying, with the lowest impact on the alginate matrix. Particularly, the air-drying preserved the shape of the printouts without excessive wrinkling; led to

an optimal texture of the forms resistant to handling; did not significantly affect the height of the dried forms. Hence, this process led to formulations with homogenous cavities that could be considered a positive thing for reproducible buoyancy. However, for both batches F6_0.1 and F6_0.25 an excessive reduction in dimension along the z-axis was observed for the lowest layer, as shown in Figure 2.4 and Table 2.4.

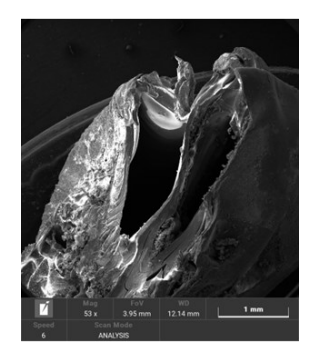




Figure 2.4 SEM images of longitudinal view of section of blank form (left), and magnification of crosslinked alginate fibre (right)

Aiming to reduce this lowering, several experiments were conducted, adding the non-ionic surfactant agent, the Tw at different percentages into the crosslinking-inks. The Tw concentration was above the CMC value (0.00029 mM) (Hait & Moulik, 2001), and reduced the surface tension of the crosslinking gel, promoting the feeds interaction and the formation of a well-structured alginate scaffold (Figure 2.4) (Kaygusuz, Evingür, Pekcan, von Klitzing, & Erim, 2016).

Table 2.5 Dimensional analysis of blank forms and related density

Printouts	D_p (%)	H_p (%)	D_d (%)	H _d (%)	Density (g/cm³)
F6_0.25	109.8	82.9	88.2	19.7	0.564 ± 0.113
F6_0.25_0.1	105.8	86.1	70.7	37.8	0.432 ± 0.050
F6_0.1	106.7	88.9	88.7	17.6	0.579 ± 0.135
F6_0.1_0.1	111.1	85.6	75.8	28.7	0.484 ± 0.080

Moreover, the addition of the surfactant also improved the height retention of the dried formulations, allowing to obtain more homogenous hollow structures. Indeed, printouts deriving from F6_0.25_0.1 batches presented a good printability in terms of shape maintenance and gelation rate (Figure 2.5).

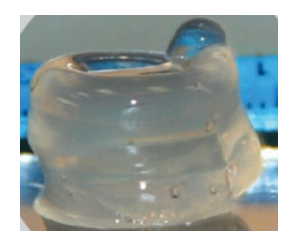


Figure 2.5 Blank form after printing

F6_0.25_0.1 batch showed a solid alginate matrix, with tunnelled filaments and the highest percentage in terms of height retention after the drying process

among all the produced formulations (Table 2.4). Notwithstanding the good results obtained adding 0.1% v/v of Tw, when the surfactant was added in higher concentration, as in F6 0.25 0.3, the formulations presented hollow filaments but, after the drying process, they resulted mealy. The texture was due to a large amount of HEC on the outer wall of the filaments, coming out after the extrusion process. Moreover, alginate matrix was brittle, underlining the effect of the surfactant in hiding part of the negative centers of alginate structure that cannot interact with calcium ions as evidenced also by Kaygusuz and colleagues, F6 0.25 0.3 were then fragile and characterized by porous matrix, with less Z shape retention after drying compared to F6 0.25 0.1 (Kaygusuz et al., 2016). The impact of 0.1 %v/v Tw on forms produced with the lowest crosslinker concentration (F6 0.1 0.1; 0.1M CaCl2) was evaluated. The results showed a slight reduction in height of these formulations compared to F6 0.25 0.1 batches, but these forms displayed a good shape retention.

To highlight the floating ability of these innovative platforms, the buoyancy properties of each of them were evaluated, all the high-resolution printouts showed a floating time of 5 ± 1 hours without a lag phase, thanks to low density values (Table 2.4). Regarding the interaction of matrices with gastric simulated fluid, all the tested batches showed a rapid gain in the weight acquired in the first 30 minutes, that gradually increased during the tests time (Figure 2.6).

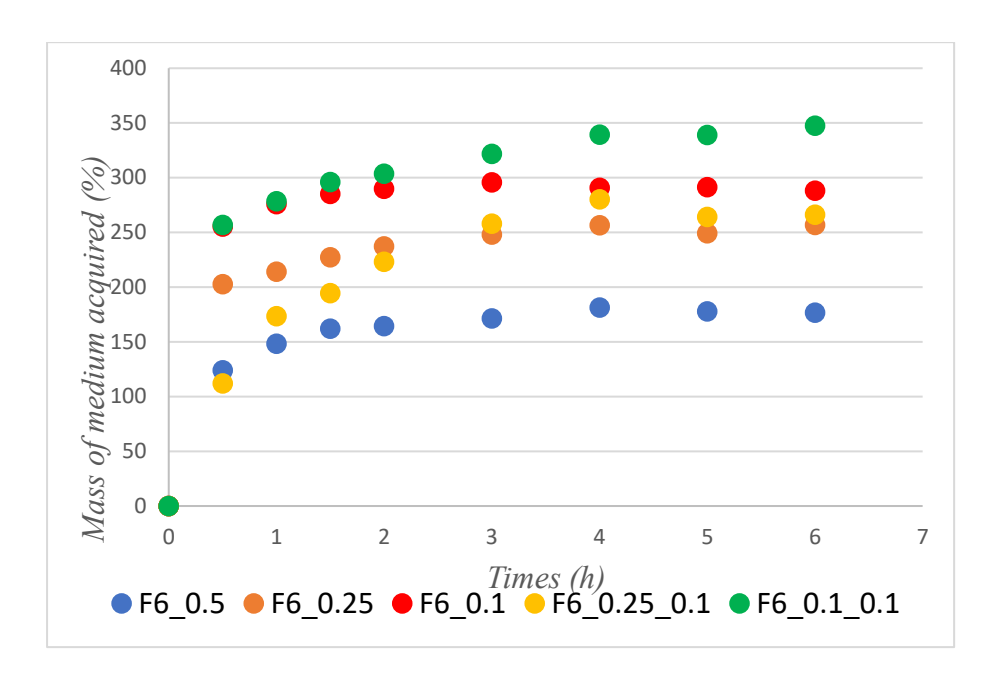


Figure 2.6 Graphical representation of media induced matrix behaviour

The graph allows to evidence a rapid hydration of the polymer into aqueous solutions that may ease the drug dissolution. A relationship between CaCl₂ concentration and medium uptake capacity was highlighted, with a doubling of fluid absorbed by F6_0.1_0.1 compared to F6_0.5. Moreover, the addition of Tw positively affected the medium uptake capacity, in fact the absorption capacity increased from 250% to 350%.

After the successful development of a new alginate/calcium chloride co-axial extrusion system described above, the addition of Propranolol Hydrochloride into the ink for SSE formulations was carried out, theorising the application of this single-step manufactured DDS in the personalized therapy.

.

Figure 2.7 Chemical structure of Propranolol Hydrochloride

Prp (Figure 2.7) is a non-selective beta-adrenergic antagonist used to treat hypertension, angina, or more in general cardiovascular disease. The Prp is a lipophilic drug, with a poor water solubility, insoluble in intestinal fluids, while its solubility increases in acidic condition, like gastric fluid. Moreover, it is characterized by short bioavailability due to the high first-pass metabolism that negative affects Prp half-life (Jagdale, Agavekar, Pandya, Kuchekar, & Chabukswar, 2009). This pharmacokinetic aspect limited the Prp administration, with a therapeutic plan that involve in the administration of fast dissolving tablets 3 or 4 times per day, reaching a daily dosage between 80 to 150 mg. Based on this information, the delivery of Prp via gastro-retentive drug delivery systems (GRDDS) could allow to improve the effect of therapy also reducing the toxicity or therapeutic failure due to the dose fluctuation (Srikanth, Rao, Sunil, Ram, & Kolapalli, 2012).

The most promising combination of gels was selected to be loaded with Prp

• Alginate ink: SA 6% w/v

• Crosslinker ink: CaCl₂ 0.1 M + HEC 3% w/v + Tw 0.1% v/v

To identify in which ink, i.e., alginate or crosslinking gel, it was better to load the drug, the characteristics of all gel components were evaluated. The API loaded alginate ink was initially produced, however, during the gel preparation phase, the incompatibility of SA with anionic salts due to precipitation phenomena was highlighted. Therefore, for the following experiments, Prp was added to the crosslinker gel. Different ratios of Prp concentration were selected in accordance with maximum and minimum daily dosage (25% w/w ~190mg and 12.5% ~95mg considering a DDS with an average mass of 1500 mg). In addition to the evaluation of the effect of different drug concentrations, batches with 12.5% w/v of drug were produced also various heights 2, 3 or 4 layers (Table 2.5), to verify the potential application of the developed SSE 3D printing system in personalized medicine.

Table 2.5 Size of the digital toroidal models

Toroidal models	External diameter (mm)	Internal diameter (mm)	Height (mm)	Number of layers	Graphical representation
Drug-loaded formulations	13.00	7.00	7.75	2	
	13.00	7.00	11.75	3	
	13.00	7.00	15.75	4	

As expected, a growth of residual weight has been found for higher drug loaded batches, but not for forms with different heights (Table 2.6). Moreover, the high reproducibility of printing process of all batches was highlighted by the weight of single layers (535.41 ± 40.00 mg) obtained during the production of different digital models.

Table 2.6 Mass evaluation of Prp loaded DDS

DDS	Alginate Ink SA (% w/v)	Crosslinking ink PrpHCl (% w/v)	Post-printing weight (mg)	M _d (%)
EC 0.1.0.1	(70 W/V)	(70 W/V)		
F6_0.1_0.1 25 (3)	6	25	1.81 ± 0.03	14.6 ± 0.7
F6_0.1_0.1 12.5 (2)		12.5	1.05 ± 0.03	12.1 ± 0.6
F6_0.1_0.1 12.5 (3)		12.5	1.56 ± 0.08	12.1 ± 0.3
F6_0.1_0.1 12.5 (4)		12.5	2.10 ± 0.04	11.9 ± 0.7

Finally, the addition of Prp in the crosslinking gel had a positive influence on the shape retention, as underlined by the θ_L and θ_R values of gel loaded with 12.5% of API (θ_L = 57 ± 1; θ_R = 59 ± 1), while the number of layers; influenced the DDS density, which slightly decreased as the layers increased (Table 2.7).

Table 2.7 Dimensional and density evaluation of Prp loaded DDS

DDS	D_p (%)	H_p (%)	$D_d(\%)$	H_d (%)	Density (g/cm³)
F6_0.1_0.1 25(3)	113.7	95.6	81.2	44.5	0.551±0.059
F6_0.1_0.1 12.5(2)	111.5	94.8	87.1	36.7	0.494±0.092
F6_0.1_0.1 12.5(3)	111.3	89.3	92.6	64.5	0.463±0.041
F6_0.1_0.1 12.5(4)	111.2	91.9	86.8	42.7	0.392±0.032

Figure 2.8 showed the Prp loaded DDS immediately after printing.

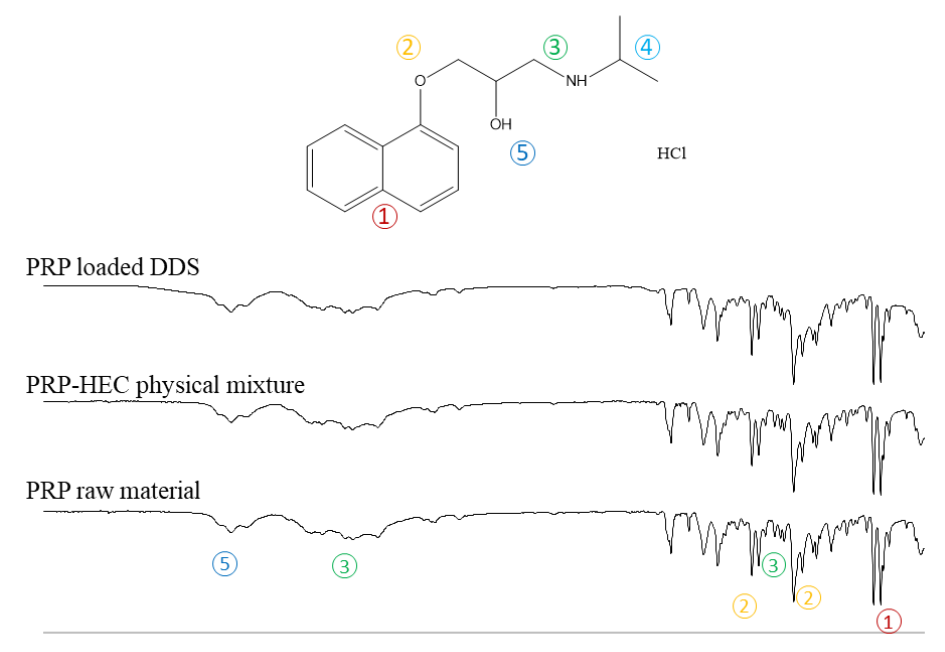




Figure 2.8 Macroscopic image of $F6_0.1_0.1_12.5(3)$ and $F6_0.1_0.1_12.5(4)$

To verify the presence of interactions between Prp and the polymers, FT-IR analysis was carried out (Figure 2.9).

Propranolol HCl structure



3850 3600 3350 3100 2850 2600 2350 2100 1850 1600 1350 1100 850 600

Figure 2.9 FT-IR spectra of Prp raw material, Prp-HEC physical mixture, and Prp loaded DDS. The Prp HCl structure, with schematic representation of the chemical bonds, was reported to allow data analysis

Particularly, the spectrum of drug-loaded form showed a shift of COO-asymmetric stretch at lower wave-values compared to neat SA spectrum as result of the calcium-alginate interaction. Moreover, a large peak in the range 3200-3400 cm-1 was highlighted, due to the extensive hydrogen bonding founded (Daemi & Barikani, 2012). The Prp spectrum in showed several characteristic peaks: two peaks in a range 770-797 cm⁻¹ identified the α-naphthalene group (peak 1); at 1072 cm⁻¹ the symmetric stretch of C-O-C was observed, as well as the asymmetric stretch at 1266 cm⁻¹ (peak 2); the C-N bond was detected among 1147-1170 cm⁻¹ (peak 3), and finally the O-H and N-

H bonds were shown at 3227 (peak 4) and 3032-2968 (peak 5) cm⁻¹, respectively (Farhadnejad et al., 2018). Following the results proposed by Takka S. et al. about the interactions of Prp and anionic polymers, the FT-IR spectra of HEC-Prp physical mixture and drug-loaded formulations were compared with Prp spectrum to investigate eventually additional bands, broadening or alterations in wavenumber position (Takka, 2003). From the comparison between neat API, HEC-Prp physical mixture and drug loaded DDS, all characteristics peaks of Prp were still detected, underlining no chemical interaction among the components of the formulations.

The data obtained from FT-IR were coupled with DSC thermal analysis (Figure 2.10). The API thermogram (Figure 3.5) showed an endothermic peak at 165°C, representing the melting range of PrpHCl commercially available, in accordance with Bartolomei et al. (Bartolomei, Bertocchi, Ramusino, & Signoretti, 1998).



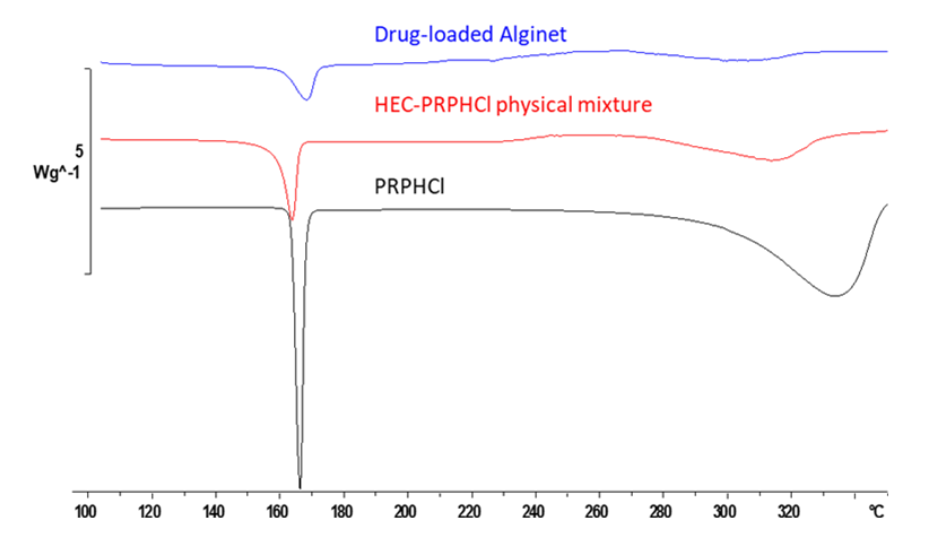


Figure 2.10 Thermal profile of Prp raw material (black), Prp-HEC physical mixture (red), and Prp loaded DDS (blue)

The same peak was detected in the thermograms of HEC-Prp physical mixture and drug-loaded DDS, proving the absence of physicochemical interactions and therefore the drug stability during all processing steps.

Moving to the technological properties of printed DDS, DLE and DC were among the most interesting aspects to be analysed (Table 2.8), in relation with different API concentrations or different digital models.

Table 2.8 Drug loading efficiency and drug content values from different Prp loaded DDS

DDS	Drug loading Efficiency	Drug Content
F6_0.1_0.1_25 (3)	60.84±2.31	50.47±1.60
F6_0.1_0.1_12.5 (2)	87.07±2.05	45.63±0.29

F6_0.1_0.1_12.5 (3)	85.30±0.90	41.09±0.55
F6_0.1_0.1_12.5 (4)	83.80±1.04	42.54±0.73

The DLE was significantly lower in printouts with higher amount of API in the crosslinking ink.

Matching the data (Table 2.8) with SEM acquisitions (Figure 2.11), the reduced loading efficiency and reproducibility of formulations containing Prp 25% w/v were probably due to the elevated migration of the drug into the HEC during the formation and drying of filaments (Figure 2.11), aided by the drug solubility.

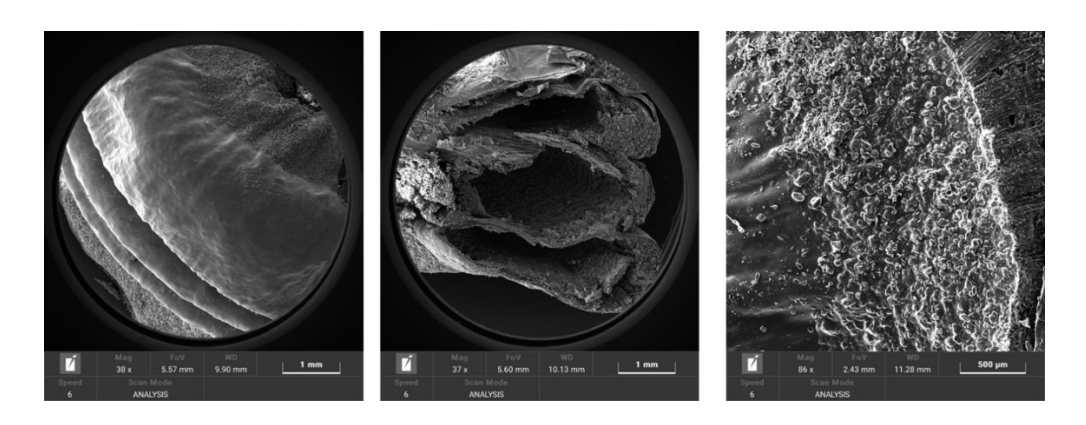
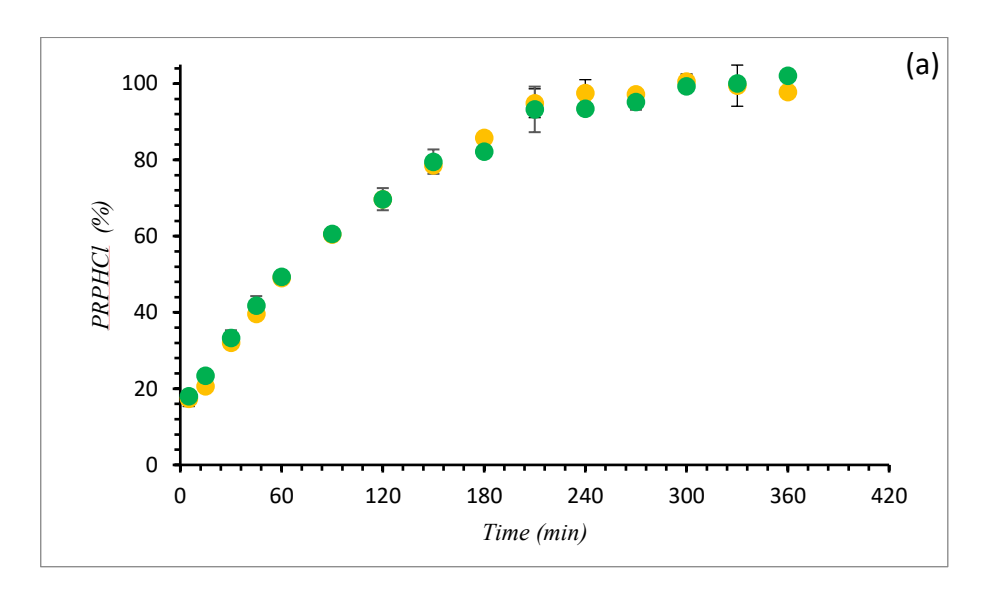


Figure 2.11 SEM acquisitions of Prp loaded DDS. From left to right: external view, longitudinal view, and layer cross section

On the contrary, the variation of digital models in height (at the same drug concentration, 12.5% w/v) did not affect the DLE (Table 3.4).

Finally, DDS obtained from different drug concentrations (12.5% and 25% w/v) or digital models (2, 3 or 4 layers with 12.5% w/v of API) were subjected to dissolution tests (Figure 2.12).



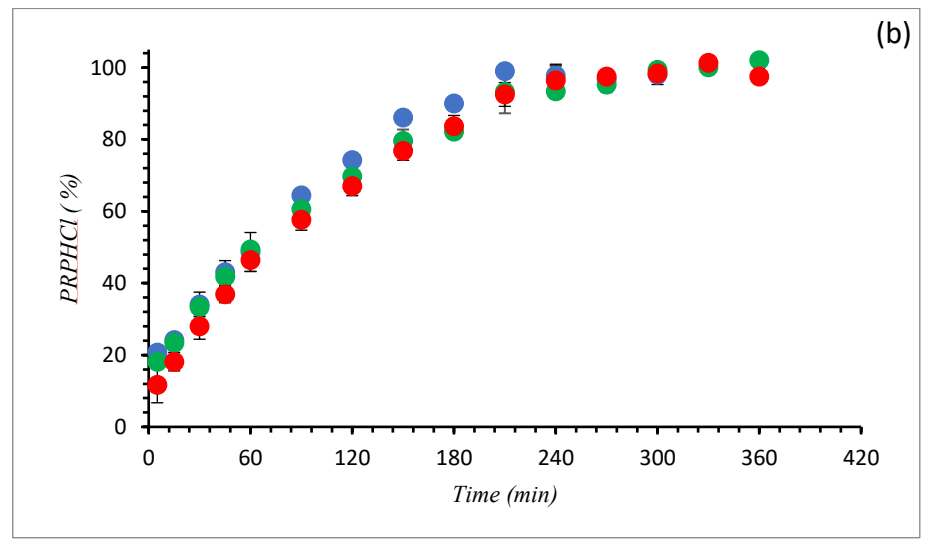


Figure 2.12 Dissolution profile a) DDS produced from feeds with different drug concentration. green: $F6_0.1_0.1_12.5$ (3); yellow: $F6_0.1_0.1_25$ (3); b) DDS printed with different number of layers blue: $F6_0.1_0.1_12.5$ (2); green: $F6_0.1_0.1_12.5$ (3); red: $F6_0.1_0.1_12.5$ (4)

For all DDS, the drug release was complete after 6 hours. Matching data obtained from drug release, DC and DLE, it is possible to assume that the overlap of 25% w/v curves and 12.5% w/v curves (Figure 2.12a) does not means that the kinetic release was independent from drug concentrations, but probably it was due to the maximum load capacity of the polymeric matrix. While the release kinetics obtained from F6_0.1_0.1_12.5 batches with 2, 3 and 4 (Figure 2.12b) were very similar, ensuring the ability to produce formulations with different drug dosages exploiting the developed SSE process without affecting the drug release.

As shown by Table 2.9, the Peppas-Korsmeyer's equation (Ritger & Peppas, 1987) fitted well the release data producing r2adj > 0.92 and lower values of reduced $\chi 2$ for all formulations

Table 2.9 Fitting of different kinetic models on the release profiles of different formulations

Higuchi		Korsmeyer-Peppas		eppas
r ² adj † Reduced		r^2_{adj}	†Reduced	n (S.E.)
	χ^2		χ^2	
0.872	8.83	0.920	2.62	0.71 ± 0.04
0.837	9.80	0.935	2.01	0.73 ± 0.07
0.803	8.39	0.972	1.82	0.77 ± 0.04
0.832	8.98	0.935	2.08	0.75±0.11
	r ² adj 0.872 0.837 0.803	r^{2}_{adj} †Reduced χ^{2} 0.872 8.83 0.837 9.80 0.803 8.39	$ \begin{array}{c cccc} r^2_{adj} & {}^{\dagger}\textbf{Reduced} & r^2_{adj} \\ & \chi^2 & \\ \hline 0.872 & 8.83 & 0.920 \\ \hline 0.837 & 9.80 & 0.935 \\ \hline 0.803 & 8.39 & 0.972 \\ \hline \end{array} $	$ \begin{array}{c ccccccccccccccccccccccccccccccccccc$

^{*} r^2_{adj} : 1-[(n-1/n-k-1)(1-r²)], n: number of data points, k: number of independent variables

 $^{^{\}dagger}\chi^2/\text{DoF}$ as obtained by the Levenberg-Marquardt method

. The Higuchi's model (Higuchi, 1961) showed in all cases poorest performance. Moreover, the values of coefficient n, ranging between 0.71 and 0.77, indicate a complex non-Fickian transport mechanism involving matrix swelling depending on the number of layers (Figure 2.8). In fact, increasing the matrix's layers results in a relaxed matrix in height able to strictly control drug diffusion trough the alginate hydrogel at the boundary of the forms (Peppas & Sahlin, 1989).

Both n coefficient and reduced $\chi 2$ were not significantly influenced by drug concentration in any fitting model leading to the conclusion that drug content do not contribute actively to the release behaviour into the produced formulations.



Figure 2.8 SEM image of DDS matrix after dissolution test

2.4 Conclusion

In this research, the hypothesis of applying the extemporaneous gelation of sodium alginate in 3D printing compounding, via co-axial Semi-solid extrusion 3D printing was successfully assessed and confirmed. The best composition of alginate and crosslinking inks for the in-situ one-step production of hollow floating forms was identified

Alginate Ink: sodium alginate 6% w/v

Crosslinking Ink: calcium chloride 0.1M, thickened with hydroxyethyl cellulose 3% w/v and added with Tween85® 0.1% v/v. Specifically, HEC was used to obtain a gel with adequate extrudability of the crosslinking feed, while the surfactant addition improved the resolution of dried DDS (an increase of a further 10% in height).

Finally, innovative GRDDS were successfully produced by co-axial Semisolid extrusion 3D printing using in a pioneering manner the ionotropic gelation of sodium alginate. The addition of Propranolol hydrochloride in the crosslinking ink, in two different concentrations (12.5 and25% w/v), enhanced the ink extrudability, lowering the angle values of the deposited drop. Even varying the digital model of the DDS in terms of number of layers, the elevated reproducibility of the developed process was highlighted in terms of mass of a single layer (average value of 535 mg) and drug content (43% w/w). Furthermore, the optimized process did not affect the physico-chemical

characteristics of the components, as supported by FT-IR and DSC thermal analyses results. Furthermore, the drug release kinetics of batches with 12.5% w/v of API but differing in number of layers (2, 3 or 4 layers) were strictly similar and independent from the drug amount. These results guide the possible application of co-axial Semi-solid extrusion 3D printing in the personalization of dosage according to the patients' therapeutic plans

Application of the alginate extemporaneous gelation for the production of customizable Ricobendazole DDS for veterinary use

Based on the Article

Falcone, G., Real, J.P., Palma, S. D., Aquino, R. P., Del Gaudio, P., Garofalo, E., & Russo, P. (2022). Floating Ricobendazole Delivery Systems:

A 3D Printing Method by Co-Extrusion of Sodium Alginate and Calcium Chloride. International Journal of Molecular Science, 260, 23(3), 1280.

https://doi.org/10.3390/ijms23031280

3.1 Scientific background and research aim

Benzimidazole composites, due to their wide spectrum of action, good tolerability, and low toxicity are at present the first-choice drugs for the treatment of helminthic parasites such us nematode and trematode in domestic and livestock animals (Liu & Weller, 1996; McKellar & Scott, 1990). The pharmacokinetic properties of these anthelmintic drugs, in particular the rate and ex-tent of gastrointestinal absorption, are strongly influenced by some extrinsic parameters, i.e., species, dosage, and function of the esophageal groove reflex (Spasov, Smirnova, Iezhitsa, Sergeeva, & Ozerov, 2002). For this reason, the control and the improvement of the benzimidazole pharmacokinetic profile represent an important challenge to allow for efficacious parasite control in animals (Lifschitz, Lanusse, & Alvarez, 2017; Lopez-Garcia, Torrado-Duran, Torrado-Duran, Martínez-Fernández, & Bolás-Fernández, 1997). To achieve this goal, for more than three decades the benzimidazole backbone underwent to chemical modifications to develop several subclasses: triazoles, probenzimidazoles and methylcarbamates (Shahare, Kadam, Jagdale, Gandhi, & Gaikwad, 2012). However, these compounds were characterized by a very low water solubility that limits the drug's bioavailability, creating a technological challenge (Lanusse et al., 1998). Gastro-retentive drug delivery systems (GRDDS) can potentially be the most suitable forms in accordance with the technological and pharmacokinetic requirements of methylcarbamate anthelmintic drugs (Dib et al., 2015). Following the potential advantages of benzimidazole gastric release, in the present study the innovative calcium-alginate floating system previously described was applied to this veterinary drug to obtain new ricobendazole loaded GRDDS.

3.2 Materials & Methods

3.2.1 Materials

All ingredients used for the preparations of the inks, both alginate and crosslink-ing, and the media for analysis are listed below: the Sodium Alginate (SA) European Pharmacopoeia 10th (CAS 9005-38-3, Carlo Erba, Milano, Italy) with a ratio between β-d-mannuronic:β-l-guluronic acid of 1.3, MW > 200,000 g/mol, and 1% aqueous solu-tions viscosity 65 mPa·s was selected as the polymeric matrix; hydroxyethyl cellulose (HEC) high viscosity (CAS 9004-62-0, ACEF, Piacenza, Italy) (2100 mP·s of 1% aqueous solu-tions),

with a 1.5 degree of substitution was used as thickening agent; calcium chloride (CaCl₂, CAS 10043-52-4, VWR International, Milano, Italy) was used as the crosslinking agent; Tween® 85 (Tw, CAS 90005-70-3, Sigma-Aldrich, Milano, Italy) was used as stabilizer; Ricobendazole (Figure 3.1) (RBZ, CAS 54029-12-8, Todo Droga® Córdoba, Argentina) ≥ 98% (HPLC) was used as the API focus of this study; ethanol 96% (CAS 64-17-5, Sig-ma-Aldrich, Milano, Italy) Reag. Ph Eur., hydrochloric acid 37% w/w (ACS reagent, CAS 7647-01-0, Sigma-Aldrich, Milano, Italy) and sodium phosphate (CAS 7601-54-9, Sigma-Aldrich, Milano, Italy) were used for the preparation of the dissolution media.

Figure 3.1 Ricobendazole chemical structure

3.2.2 Methods

3.2.2.1 Alginate and Crosslinking Ink Preparation

For the alginate ink preparation, 6% w/v of sodium alginate powder was added into a pre-settled volume of water and magnetically stirred at 70 rpm to reach full hydration of the matrix. The crosslinking ink containing the calcium

chloride for the co-axial extrusion system was optimized in accordance with the physico-chemical properties of RBZ, the active ingredient selected. In particular, to slightly improve the drug solubility (62 μg/mL in water and 1.2 mg/mL in ethanol (Wu, Razzak, Tucker, & Medlicott, 2005) and maintain the gel extrudability, a 80/-20 water ethanol solution was used as solvent and the HEC was added at a concentration of 2.0% w/v. Firstly, the drug was dispersed into the ethanol and then the alcoholic dispersion was added to the aqueous calcium chloride solution to obtain an hydroalcoholic suspension (final concentration 5% w/v in RBZ; 0.05–0.1 M in CaCl2) stabilized with Tween 85 (0.1% v/v).

3.2.2.2 Rheological characterization

With the aim to highlight the rheological properties of each ink, Rotational, and Oscillatory analysis were carried out. In detail, Flow curve (rotational test) with a shear rate from 1*1/s to 25*1/s, and amplitude sweep (oscillatory test) with a shear strain from 0.1% to 100% (constant frequency of 10*1/s) were performed.

Measurements were performed using MCR 102 rheometer (Anton Paar, Austria) equipped with parallel plate (PP25, with a diameter of 24.985 mm) selecting as measuring gap values 0.250 mm (Figure 3.2).



Figure 3.2 MCR 102 Rheometer by Anton Paar (https://www.anton-paar.com/it-it/prodotti/dettagli/reometri-mcr-102-302-502/)

3.2.2.3 DDS Digital optimization & SSE printing process

The digital model of RBZ DDS was developed via the CAD software Rhinoceros 6. The 3D structure selected was a double circumference toroid with an external diameter of 22 mm, a height of 14 mm, and a central hole of 10 mm. The model, in the form of an STL file, was processed with Cura 4.6.1 (Ultimaker, The Netherlands) to optimize the printing parameters (initial layer height, 3 mm; layer height, 2.75 mm; number of layers, 5). The printing process was performed with lab made coaxial extruder connected through tubes to a syringe pump system, Fusion 4000 (Chemix Inc., UK). The flow rate was fixed at 50 μ L/min for the alginate ink and at 100 μ L/min for the crosslinking feed.

3.2.2.4 Printing resolution and reproducibility

To investigate the resolution and reproducibility of the different manufacturing processes, for all the produced batches the mass and the dimension (diameter "D" and height "H") were analyzed during both steps: post-printing and post-drying. In detail, at least six printed units for each formulation were accurately weighed by digital analytical balance (MX5 micro-balance, Mettler Toledo, Germany) both after printing and after drying. The results of post-printing mass were reported as absolute values (g) with standard deviation; for post-drying mass evaluation, the results were showed thanks to the following equation:

$$M_d$$
 (%) = $\frac{Mass\ after\ drying\ (mg)}{Mass\ after\ printing\ (mg)} * 100$ (Eq 3.1)

Where M_d is the mass variation after drying.

Similarly, the dimensions were analyzed after both steps by digital caliper. the acquired data were used to calculate the process resolution and reproducibility. For the evaluation of shape fidelity after printing, the data were related to the digital dimensions exploiting the equation reported below:

$$D_p (\%) = \frac{D_{Printed model}}{D_{Digital model}} * 100$$
 (Eq 3.2)

$$H_p$$
 (%) = $\frac{H_{Printed\ model}}{H_{Digital\ model}} * 100$ (Eq 3.3)

While, to highlight the impact of drying process on the shape fidelity, the dimension after drying were related to the dimension after printing

$$D_d (\%) = \frac{D_{Dried \ model}}{D_{Printed \ model}} * 100$$
 (Eq 3.4)

$$H_d (\%) = \frac{H_{Dried \ model}}{H_{Printed \ model}} * 100$$
 (Eq 3.5)

3.2.2.5 Morphological Analysis

The DDS after printing were photographed with a single lens reflex camera (Canon EOS 600D; parameters: f-stop: f/6.3, shutter speed: 1/5 s, ISO 200). To obtain information about the impact of both API addition and further reduction in calcium concentration, the drug-loaded dried formulations were observed by Scanning Electron Microscopy (Tescan Solaris, Tescan Orsay Holding, Czech Republic)

3.2.2.6 FT-IR analysis

FT-IR analysis was carried out using FT-IR spectrophotometer (Spotlight 400N FT-NIR Imaging System, Perkin Elmer Inc, USA) equipped with an ATR accessory (ZnSe crystal plate) to detect any changes in the drug structure during the printing and drying processes. All the analysed samples i.e., powders, films and printed layer particles were analysed using 128 scans and 1 cm-1 resolution step in the spectral range of 4000-600 cm-1.

3.2.2.7 DSC Thermal Analysis

The differential scanning calorimetry were performed by DSC 822e (Mettler Toledo, Germany) while the results were processed by Mettler Toledo STAR^e software.

The analytic protocol involved the use of 40 µL predrilled aluminium pans filled with a standard mass of materials (3-5 mg). The samples were analysed in form of powders, films, and printed layer particles. A single dynamic thermal cycle was performed in a range from 25°C to 300°C at a heating rate of 10 °C/ min

3.2.2.8 Buoyancy tests

Buoyancy tests were performed gently placing the dried formulations in acidic dissolution medium prepared according to the method proposed by USP 36 (dissolution 0.1M HCl solution; pH 1.2 ± 0.5). The medium was in constant stirring at 70 rpm and at 37 ± 0.5 °C. The lag time before the buoyancy and the floating time of the single samples were visually evaluated and reported in hours

3.2.2.9 Drug content analysis and drug-loading efficiency

All the formulations ($n \ge 3$) loaded with RBZ were evaluated in terms of drug content (DC) and drug loading efficiency (DLE) values.

The DLE (Eq.) has been calculated as:

DLE (%) =
$$\frac{Mass\ of\ PrpHCl\ observed\ (mg)}{Mass\ of\ PrpHCl\ predicted\ (mg)} * 100$$
 (Eq 3.6)

and the DC (Eq.) according to:

$$DC (\%) = \frac{Mass \ of \ PrpHCl \ observed \ (mg)}{Mass \ of \ dryed \ formulation \ (mg)} * 100$$
 (Eq 3.7)

The RBZ content was obtained relating the absorbance values of each sample at 295 nm of wavelength (λ) (detection acquired by using UV-vis

Spectrophotometer (Evolution 201 UV–vis Spectrophotometer, Thermo Fischer Scientific Inc.), with PBS calibration curve (concentration range: from $10.3 \,\mu\text{g/ml}$ to $63 \,\mu\text{g/ml}$).

3.2.2.10 Dissolution tests

Dissolution tests were performed with USP dissolution Apparatus II (AT7 Smart Dissolution Tester, Sotax Corporation): paddle or basket configuration (figure 5), 70 rpm stirring, 37 °C, using as dissolution medium in gastro (pH 1.2 ± 0.5) and/or intestinal (pH 6.8 ± 0.5) simulated fluids, according to USP 36.

For all drug loaded batches, the absorbance values i.e., 298 nm RBZ, at different times were measured and related to the API acidic calibration curve (in a range of concentration from 10.5 μ g/ml to 65 μ g/ml). For all batches analyzed, mean values and standard deviations were reported.

3.2.2.11 Release kinetics fitting studies

Fitting analysis on the release data was performed by using two different kinetic models i.e., the Higuchi's model (Eq.4.8) and Peppas-Korsmeyer's equation (Eq. 3.9) were used.

Higuchi's model is one of the most used to investigate pure Fickian transport, when pure diffusion is the main driving force of the release (Higuchi, 1961)

Higuchi:
$$M_t = A\sqrt{D(2C_0 - C_S)t}$$
 (Eq 3.8)

where Mt is the drug cumulative amount released at time t, t is time, A is the surface area, D the diffusivity of the drug through the matrix, and C0 and Cs are the initial drug concentration and drug solubility, respectively.

The Peppas-Korsmeyer's equation (Ritger & Peppas, 1987) used to mainly explain complex release mechanisms where diffusion is coupled with erosion or swelling of the matrix:

Peppas – Korsmeyer:
$$\frac{M_t}{M_{\infty}} = kt^n$$
 (Eq 3.9)

where $M\infty$ is the drug amount released at infinity, k is a constant, and n is a diffusion coefficient, which depends on geometry of the system and on the release mechanism. When pure diffusion controls the release mechanism n=0.5, whereas when n=1 the release is mechanism is dominated by a case II transport and Eq. 9 turns into a zero-order kinetic.

The use of both equations is mainly limited to the description of the first 60% of the release (however, the fitting performed over 60% of release was compared to that over 100% of the profile to verify the adequacy of the procedure. Correlation coefficient corrected for the degree of freedom of the system (r^2_{adj}) and reduced χ^2 Levenberg–Marquardt method (Jang & Mizutani, 1996) for the minimization of the function were used to evaluate the lack of fit.

3.2.2.12 Mechanical investigation of DDS strength

The DDS mechanical strength analysis was conducted with a CMT 6000 dynamometer (MST[®], Beijing, China) equipped with a 1 kN load cell. One DDS was placed between two steel plates; the upper one, connected with the load cell, was then manually lowered towards the DDS surface (Russo et al., 2019). The test in the compression mode was then started at a velocity of 5 mm/min. The data were reported in a graph obtained plotting the recorded strength (kN) against the travel made by the upper plate (mm).

3.3 Results and discussion

To develop this DDS loaded with RBZ, the first part of the study was focused on the optimization of the crosslinking ink, matching the physicochemical characteristics of RBZ with the printing requirements of the ink. Two different concentrations of calcium chloride were tested with the aim to better highlight the relation between the crosslinking process and the physicochemical properties of drug that could influence both printing and drying process, as well as the final properties of DDS (Table 3.1)

Table 3.1 Composition of alginate and crosslinking ink for both DDS0.05_R5 and DDS0.10 R5

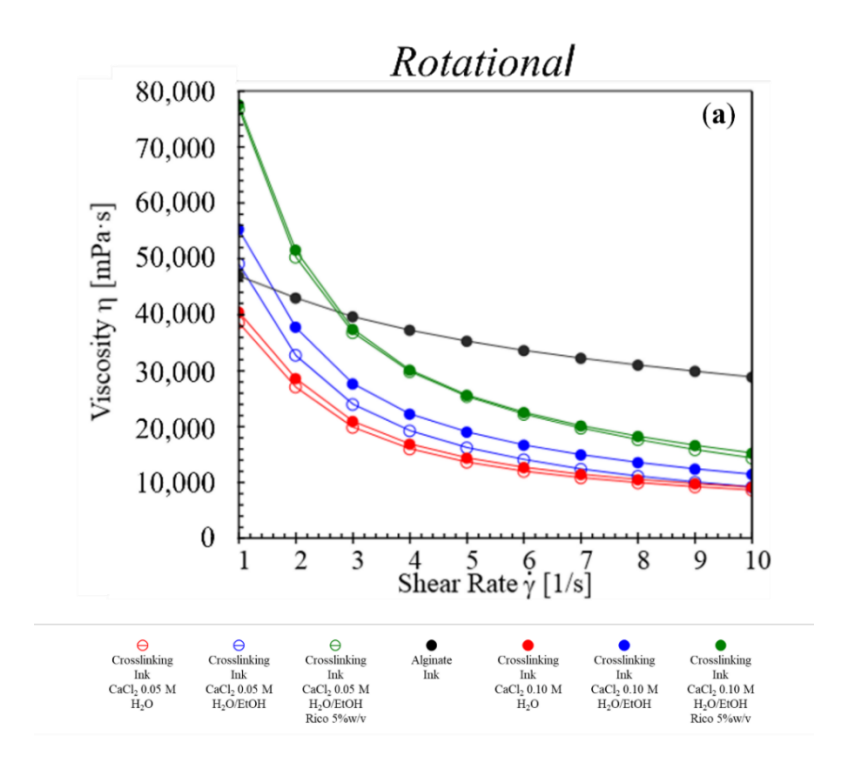
DDS	Inks		
	Alginate	Crosslinking	
DDS0.05_R5	Solvent	Solvent	
	H ₂ O	H ₂ O/EtOH 80/20 v/v	
	Ingredients	Ingredients	

		ium 60/ m/m	CaCl ₂	0.05 M
	Sodium		RBZ	5% w/v
	Alginate	6% w/v	HEC	2% w/v
			Tw	$0.1\% \ v/v$
Code	Inks			
	Alginate		Crosslinking	
	Solvent		Solvent	
	H_20		$H_2O/EtOH~80/20~v/v$	
DDS0.10 R5	Ingredients		Ingredients	
DDS0.10_K3			$CaCl_2$	0.10 M
	Sodium Alginate	6% w/v	RBZ	5% w/v
			HEC	2% w/v
			Tw	$0.1\% \ v/v$

By direct incorporation of RBZ in the aqueous crosslinking ink, a biphasic system was obtained due to the drug's very poor solubility in water, which caused a nozzle obstruction during the extrusion. Following the information proposed by Wu et al. about the solubility and lipophilicity of RBZ, some different hydroalcoholic mixtures were tested (Wu et al., 2005). Particular attention was paid to the water/ethanol mixture, which was evaluated in three different ratios from 90/10 to 70/30 to find the best balance between RBZ solubility and the ethanol effect of viscosities effect of HEC. Crosslinking ink with homogeneous drug incorporation and good extrudability was obtained using H2O/EtOH 80/20 as solvent (HEC 2% w/v, RBZ 5% w/v, and Tw 0.1% v/v) and assaying two different concentrations of calcium chloride (0.1 and 0.05 M).

To understand the physical characteristics of gels and consequently relate them to the Semi-solid extrusion printing requirements, the rheological behaviour of both feeds was analysed (Figure 4.3) (Hölzl et al., 2016; Paxton

et al., 2017). In particular, the attention was focused mainly on the crosslinking feed to highlight the impact of ethanol, calcium, and RBZ on the gel properties. Through a rotational test (Figure 3.3a), it was possible to observe a constant slight decrease in viscosity at all shear rate values for the alginate ink curve (black line); this was different from all crosslinking inks, which showed a rapid decrease in viscosity. Moreover, the increase in calcium concentration led to a minimum increase in the viscosity of the crosslinking feed both in water and hydroalcoholic gels (filled markers with 0.10 M of calcium vs. empty markers with 0.05 M of calcium). The alcohol content led to an increase in gel viscosity (blue markers vs. red ones), which further showed a 60% growth after the addition of the drug (green markers). The results obtained from the oscillatory test (Figure 3.3b) helped to highlight the key variations between alginate and crosslinking inks. The alginate ink showed a loss factor > 1, suggesting for this gel a clear prevalence of liquid behaviour, which was also confirmed by the minimum decrease in the viscosity under an increased shear rate. On the other hand, all crosslinking feeds showed a loss factor of about 0.5, with comparable gel-like properties and shear thinning behavior. (Mezger, 2020).



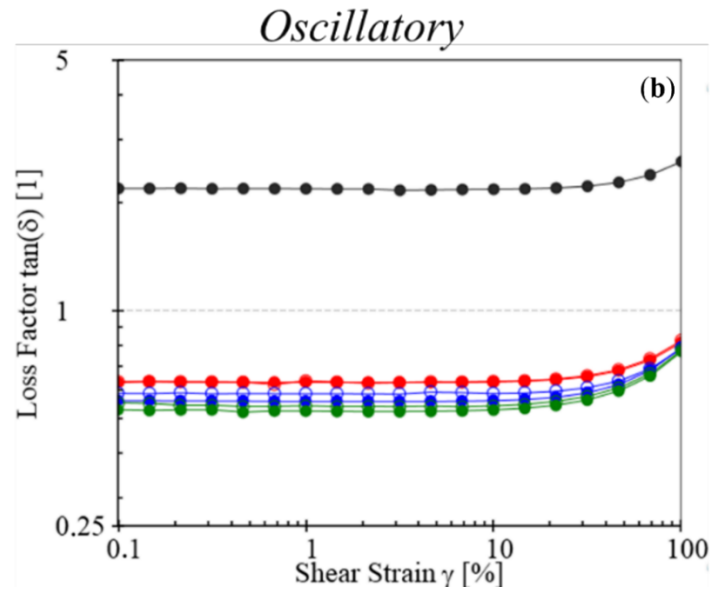


Figure 3.3 Rheological evaluation of both alginate and crosslinking inks a) rotational test, and b) oscillatory test

After the optimization of the new inks, the second part of the workflow was dedicated to the printing process and the DDS characterization. To prevent the

alginate ink from spreading onto the build plate, which could negatively affect the printing resolution, to obtain a complete gelation of the alginate during the extrusion and an excellent shape retention after printing, the flow rates of alginate and crosslinking ink was fixed at 50 μ L/min and at 100 μ L/min, respectively (Xiong et al., 2021).

Figure 3.4 is a picture of RBZ loaded DDS immediately after printing, in which it is possible to see that the masking tape was selected as print bed support material because it was characterized by the highest adhesion with the first layer ensuring the good rest of the printing process.



Figure 3.4 Photo of RBZ loaded DDS immediately after printing

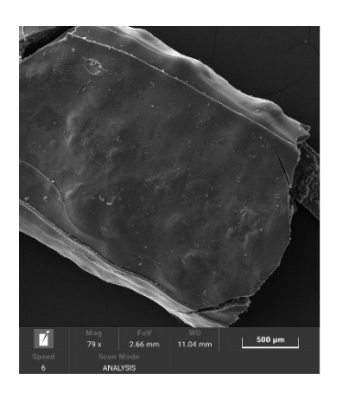
All DDS showed very low variations in mass, both after printing and after drying, underlining the high reproducibility of the co-axial printing

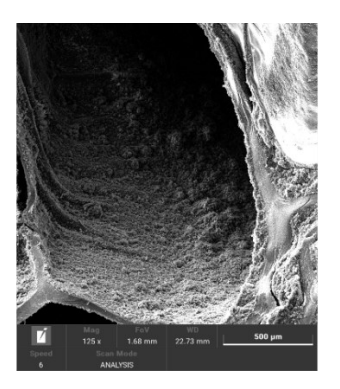
process, independently from the crosslinking agent concentration used (Table 3.2).

Table 3.2 Mass and dimensional analysis, after printing and drying of RBZ-loaded DDS

DDS	Mass (g)	D _p (%)	H_p (%)	M _d (%)	D_d (%)	H_d (%)
DDS0.05_R5	3.2 ± 0.2	110.2 ± 1.3	88.3 ± 2.8	7.9 ± 0.4	78.7 ± 7.6	33.3 ± 10.7
DDS0.10_R5	3.2 ± 0.1	97.0 ± 2.7	104.7 ± 4.0	8.7 ±0.2	81.0 ± 2.2	55.0 ± 6.6

On the other hand, the calcium concentration being very important in shape retention after the drying process. DDS0.05_R5, in fact, did not maintain its shape after drying, as evidenced by a final height of only 33% compared to the height of the model after printing (Table 4.2). The collapse of the structure was the result of a lower organization of the calcium-alginate matrix. Thanks to the SEM acquisition (Figure 3.5) it was possible to highlight the homogenous RBZ distribution in the alginate shell. In the right square of Figure 5.5 it is possible to observe the filament stratification from inside out: RBZ in crystal form, HEC foil, and the shell of calcium alginate on the bottom.





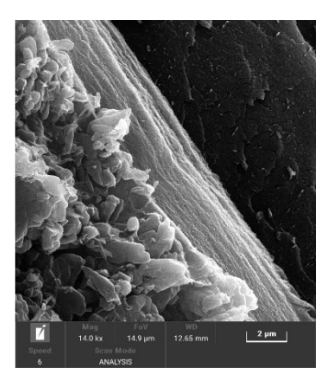
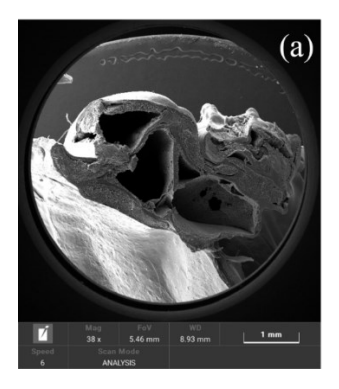


Figure 3.5 SEM capture of RBZ loaded DDS, from left to right: single layer top view, cross-section view, and longitudinal-section view

Moreover, looking at a cross section of the printout (Figure 3.6), DDS0.05_R5 produced from crosslinking ink with the lowest calcium amount showed an internal collapse after drying (Figure 3.6a) that led to the formation of RBZ niches and a dramatic reduction in empty spaces (Table 3.2). On the other hand, the DDS0.1_R5 after drying showed good shape retention with a defined hollow filament and a more uniform distribution of API next to the alginate shell (Figure 3.6b).



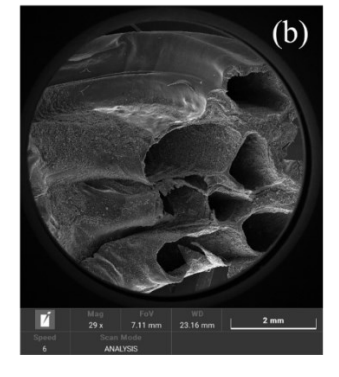


Figure 3.6 Cross-section SEM images of a) dried DDS0.05_R5, and b) dried DDS0.10 R5

Before to move to the investigation of the DDS technological properties, a physico-chemical characterization was carried out by FT-IR, DSC, and mechanical test. In accordance with the literature (Chaudhary et al., 2021), all peaks related to the benzimidazolic rings i.e., C-C at 1304 cm-1 (peak 3), C=C stretch at 1586 cm-1 (peak 5), C-N at 1516 cm-1 (peak 4), C=N at 1633 cm-1 (peak 6), C-H from 3050 to 3171 cm-1(large band-width 8), as well as the stretch of the C=O of amidic group around 1729 cm-1 (peak 7), the sulfuric group C-S at 648 cm-1 (peak 1), and S=O at 1006 cm-1 (peak 2), which distinguish the RBZ from the other benzimidazolic compounds, were identified with-out modification in the spectrum of drug-loaded DDS (Figure 3.7).

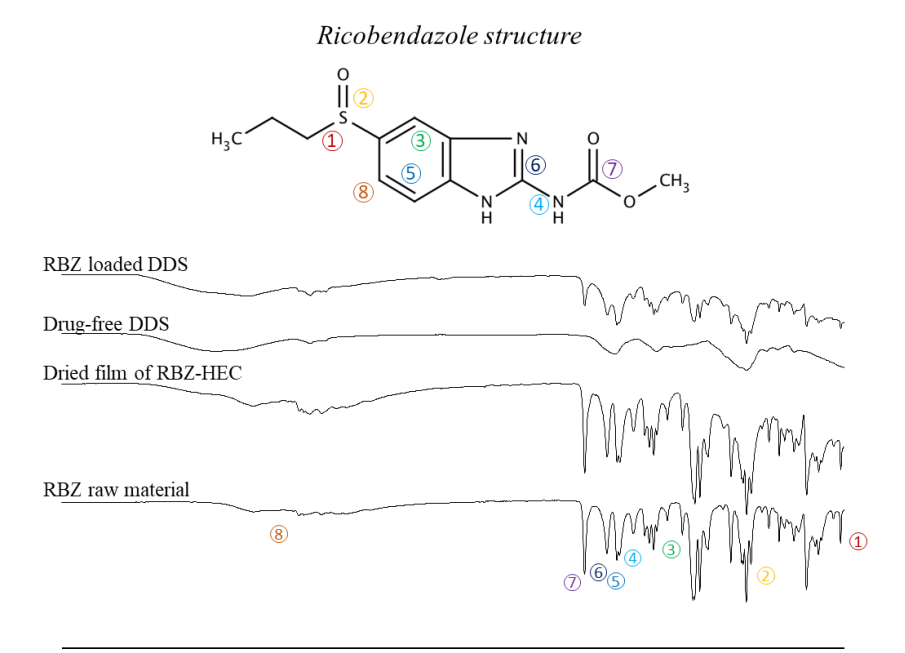


Figure 3.7 FT-IR spectrum of RBZ raw material, dried film obtained from RBZ-HEC gel, drug-free DDS and RBZ loaded DDS; RBZ structure, with schematic representation of the chemical bonds, was reported to allow data analysis

3850 3600 3350 3100 2850 2600 2350 2100 1850 1600 1350 1100 850

Through DSC analysis (Figure 3.8), the RBZ raw material exhibited an endothermic band from 207 to 224 °C due to the melting of the API polymorphs (Castillo et al., 1999) (black line in Figure 17).

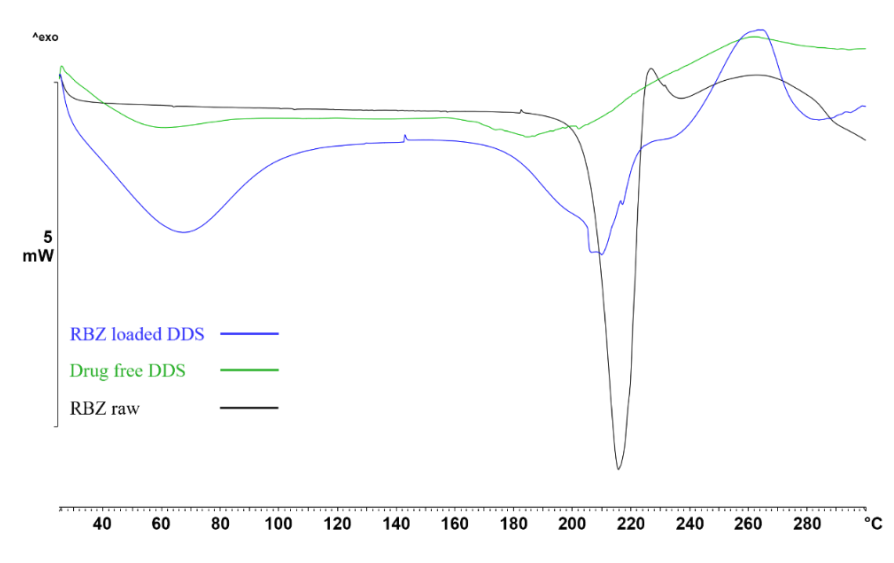


Figure 3.8 Thermographs of RBZ raw material (black line), drug-free DDS (green line), and RBZ-loaded DDS (blue line).

DDS (green and blue lines in Figure 3.8) exhibited a broad peak at temperatures lower than 100 °C due to the loss of water, and in the region around 200 °C. The peaks corresponding to the breakage of calcium—carboxylate bonds in the formed egg-box structure of the alginate polymers are clearly visible in the drug-free DDS (green line) and in the drug-loaded systems (blue line), but with different temperatures and peak broadness. The variation in temperature and profile of the drug melting peak and of the breakage of calcium—carboxylate bonds in the polymer might be correlated with a drug—polymer interaction.

The load curves (Figure 3.9) obtained following the method 3.2.2.12 showed the differences in the matrix behaviour as the calcium chloride concentration varies, with a linear increase in the recorded strength, up to the structure crack for batch DDS0.05_R5 (green line) and a series of peaks

corresponding to the progressive crushing of the different hollow filaments clearly distinguishable in the batch DDS 0.10 R5 (red line).



Figure 3.9 Load-crosshead curve of DDS0.05_R5 (green line) and DDS 0.10_R5 (red line).

The information about the drug content and the drug loading efficiency, obtained by DDS dissolution in PBS, were among the most interesting data related to the matrix composition and the drying behaviour. For both batches, DDS0.05_R5 and DDS0.10_R5, the drug loading efficiency was extremely high (Table 3.3), close to 100% for the batch containing the highest amount of calcium, suggesting a direct relationship between the stiffness/structuration of the matrix and the load retention capacity during the drying. Further confirmation of the difference in drug loading capacity was obtained from the DC values, with a slight increase after the increase of calcium.

Table 3.3 Drug loading efficiency and drug content values of both RBZ loaded DDS

DDS	Drug loading Efficiency	Drug Content
DDS0.05_R5	81.9±4.1	34.8±1.3
DDS0.10_R5	99.2±2.4	39.0±2.1

Finally, an important part of the research was related to the technological evaluation of GRDDS, from the floating properties to the drug release from GRDDS, to understand the influence of the matrix composition on of all these properties.

Batches of DDS0.05_R5 showed a considerable variation in the buoyancy properties, with a lag phase in the range from 0 to 30 min, and a floating time about 5 h with a relative standard deviation higher than 10%. Differently, the DDS0.10_R5 batches were characterized by the absence of a lag phase and a high reproducibility in the floating time of about 14 h (14 ± 1). To carry out the in vitro release studies, the test condition (0.1 M HCl solution at pH 1.2 ± 0.5, without enzymes) were selected in accordance with the technical procedure described in USP44 and have been widely reported and adopted in literature. From a macroscopic point of view, for both DDS0.05_R5 and DDS0.10_R5 a complete drug release was reached before 24 h, even if after about 5 h the DDS0.05 R5 sank (Figure 3.10)

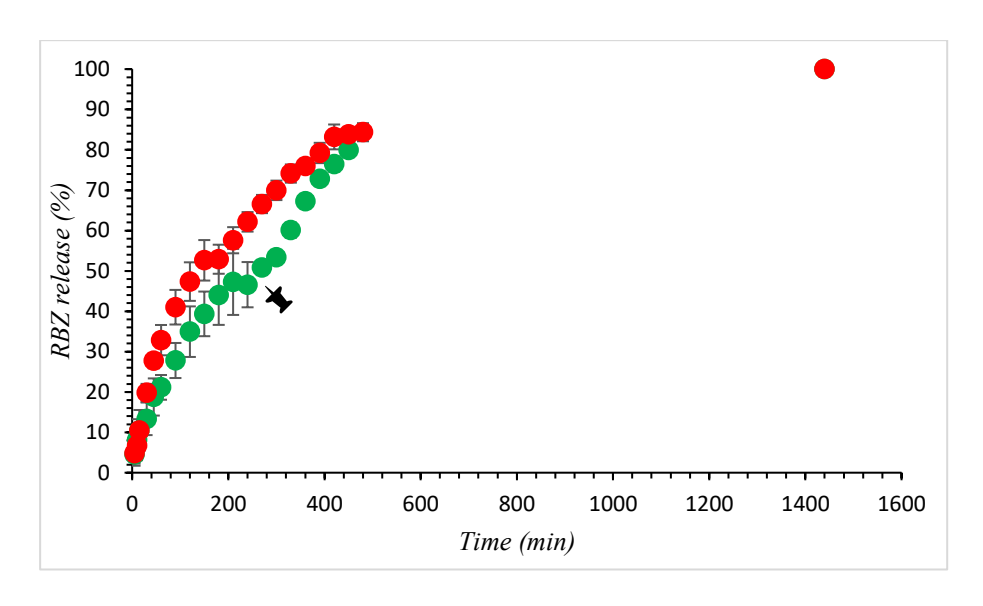


Figure 3.10 Comparison of release profiles from DDS_0.05_R5 (green) and DDS_0.10_R5 (red). The pin indicates the time point in which the sinking of DDS0.05 R5 occurs.

From the comparison between the drug release profiles, reported in Figure 3.10, it is possible to observe a significant variation in release rates due to the difference in the amount of calcium in the matrix according to the peculiar DDS properties previously described. This difference was also evidenced by the release kinetics fitting study (Table 3.4).

Table **3.4** Fitting of different kinetic models on the release profiles of different formulations.

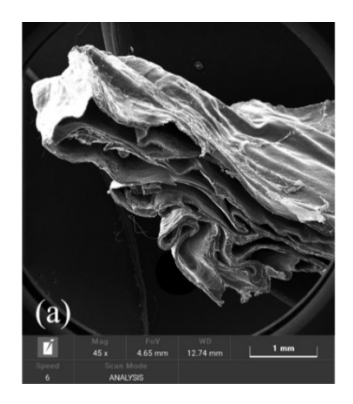
Model	Higuchi]	Korsmeyer-Pe	ppas
DDS	r^2_{adj}	†Reduced χ ²	r^2_{adj}	†Reduced χ ²	n (S.E.)
DDS0.05_R5	0.861	7.83	0.926	2.08	0.71±0.08
DDS0.10_R5	0.881	6.42	0.913	2.52	0.69±0.05

^{*} r^2_{adj} :1-[(n-1/n-k-1)(1-r²)], n: number of data points, k: number of independent variables

 $^{^{\}dagger}\chi^2/\text{DoF}$ as obtained by the Levenberg-Marquardt method

As shown by Table 3.4, the Peppas–Korsmeyer equation fit the release data well, producing r2adj > 0.92 and lower values of reduced χ2 for all formulations. Higuchi's model showed in both cases a lack of fit for the experimental points (Higuchi, 1961; Peppas & Sahlin, 1989). The values of the n coefficient indicate a complex non-Fickian transport mechanism involving matrix erosion and swelling depending on the internal network of the matrix. DDS0.10_R5 showed a lower n value, around 0.69, which is a sign of a tougher internal structure less prone to swelling compared to the external layers. In particular, the release data of DDS0.05_R5, recorded in the first two hours, showed higher standard deviation values of drug released compared to DDS0.10_R5, probably due to the different exposure of the DDS0.05_R5 surface to the dissolution medium during the inconstant lag phase.

The differences in the matrix organization generated by different concentrations of calcium were also highlighted from the SEM acquisition of DDS after the drug release (Figure 4.11).



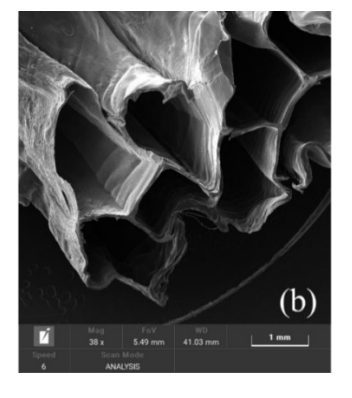


Figure 3.11 Cross-section SEM images acquired after dissolution test a) dried DDS0.05_R5, and b) dried DDS0.10_R5

It was possible to observe a further reduction in height for the DDS0.05_5 (Figure 4.11a), while the matrix of DDS0.10_5 after dissolution and re-drying (Figure 4.11b) preserved the hollow filaments with an almost unchanged matrix and simply emptied of the drug.

3.4 Conclusion

Drug delivery systems able to float while releasing the drug in simulated gastric fluids were successfully obtained by 3D printing Semi-solid extrusion, exploiting the in situ alginate ionotropic gelation. Moreover, through the addition of the right amount of crosslinking agent, the matrix showed a proper stiffness to counteract the layer collapse during the drying process, with mechanical strength values comparable to conventional tablets. The improved DDS was able to float with no lag time for about 14 h, releasing almost 80% of the loaded drug into the simulated gastric fluid during the floating time. Further in vivo studies will clarify whether this printed drug delivery system can be proposed as an interesting technological platform able to overcome ricobendazole pharmacokinetics issues, extending for many hours the contact time between the active compound and the infected tissue, as expected from an effective GRDDS.

Section 2

Pre-crosslinked alginate hydrogels as a new tool in Semi-solid extrusion
3D printing process

Based on the Article

Falcone, G.; Mazzei, P.; Piccolo, A.; Esposito, T.; Mencherini, T.; Aquino, R.P.; Del Gaudio, P.; Russo, P. Advanced printable hydrogels from pre-crosslinked alginate as a new tool in Semi solid extrusion 3D printing process. Carbohydrate Polymers 2022, 276, 118746.

https://doi.org/10.1016/j.carbpol.2021.118746

4.1 Research aim

Fang et al. described the possibility to obtain different polymeric network, i.e., monocomplexes, egg-box dimers and laterally associated egg-box multimers, adding increasing concentration of calcium chloride into the sodium alginate solution. They observed higher relative viscosity values when the alginate network is in the boundary between the egg-box dimers and the multimers (Fang et al., 2007).

Given that, in this section, another promising strategy to use the alginate in SSE-3D printing was field, speculating that a pre-crosslinking step of the alginate with low amount of Ca⁺² could improve the ink hydrogel performance,

going beyond its limits in SSE 3D printing for the development of innovative printed platforms. Therefore, compared to the previous described research, the alginate crosslinking timing was anticipated and moved from the printing step to the ink gel production.

To verify its feasibility, the influence of different pre-crosslinker concentration on the hydrogel's rheological properties, extrudability and on the shape retention of extruded forms after printing and after drying were studied, with the aim of process optimization that could lead to customizable drug platform using a ready-to-print alginate ink.

4.2 Materials & Methods

4.2.1 Materials

Sodium alginate (SA) (CAS 9005-38-3) (with β -d-mannuronic: β -l-guluronic acid ratio of 1.3 and MW > 200000 g/mol), selected as polymeric matrix for the new DDS, and Mannitol (M, CAS 69-65-8) were purchased from Carlo Erba (Carlo Erba, Milano, Italy); the crosslinking agent "Calcium chloride" (CaCl₂, CAS 10043-52-4) was provided by VWR International (VWR International, Milano, Italy).

4.2.2 Methods

4.2.2.1 Hydrogel inks production

Hydrogel inks were prepared according to the following 4-step protocol:

- Sodium alginate hydration: 6% w/v of sodium alginate powder was added into 50 mL of water and allowed to fully hydrate overnight under magnetic stirring at 70 rpm.
- Crosslinking solution preparation: different amounts of calcium chloride were accurately weighed and solubilized in 50 mL of water, to obtain crosslinked feeds with different calcium final concentrations (10mM, 12.5mM, 15mM, 18mM, 20mM and 25mM) (Fang et al., 2007).
- Alginate crosslinking: the crosslinking solution (50 mL) was slowly poured into the sodium alginate gel (50 mL) under homogenization via Ultra-Turrax® T25 (IKAWorks GmbH & Co. Staufen, Germany) to achieve a uniform crosslinking. The obtained crosslinked hydrogels were loaded into 50 mL conical centrifuge tubes and centrifuged at 2500 rpm for 10 min to remove air bubbles.
- Storage: the pre-crosslinked gels were stored for 16 hours at 4°C in a refrigerator to improve the structuring of gels.

The composition of each ink is reported in Table 4.1

Table 4.1 Hydrogel inks composition

Code	Alginate (%w/v)	Calcium Chloride (mM)
------	--------------------	-----------------------------

<i>G</i> 3	3	-
G3_10	3	10
G3_12.5	3	12.5
G3_15	3	15
G3_18	3	18
G3_20	3	20
G3_25	3	25

For the preparation of ink gels containing mannitol (15-20-25% w/v) the powder of functional material was mixed with SA powder before the hydration phase

4.2.2.2 Magnetic Resonance Imaging (MRI) of calcium-alginate hydrogels

All 1 H MRI experiments were performed at 298 ± 1 K on a 300 MHz Bruker Avance wide-bore magnet (BrukerBiospin, Rheinstetten, Germany), equipped with a 10 mm μ -imaging MICRO 5 probe working at a 1 H frequency of 300.13 MHz. Each sample (10, 15, 18, 20 and 25 mM) was loaded into 10 mm NMR tube and put vertically for 8 hours to permit a homogeneous spatial distribution of the material before the analysis.

T₂ experiments were performed by applying an echo-train MSME (multi-slice-multi-echo) pulse sequence, setting 2.5 s of recycle delay, 12 scans, and

acquiring 16 experiments with an increasing number of spin-echoes (total spin-echo time ranging within 14 and 168 ms). Data were fitted to a single exponential decay, according to the equation (Eq 4.1):

$$M_t = M_0 \exp(-t/T_2)$$
 (Eq 4.1)

where, M_0 and M_t represent the magnetization intensity resulting at the minimum spin-echo delay and after the i-th spin-echo interval, respectively. Spin density measurements were performed by considering the images obtained at the shortest echo-delay (14 ms).

T₁ measurements were acquired by RARE (rapid acquisition with relaxation enhancement) experiments, which consisted of 3 scans, a rare factor of 2, and increasing repetition times ranging within 0.286 to 22.5 s in 8 experiments. Data were fitted to a single exponential decay, according to the equation (Eq 4.2):

$$M_{\rm t} = M_0 [1-\exp(-t/T_1)]$$
 (Eq 4.2)

where, M_0 and M_t represent the magnetization intensity resulting at the full nuclear relaxation and after the i-th recovery delay, respectively.

Water self-diffusion coefficients (DIFF) were extrapolated by NMR data resulting from the application of a pulse field gradient (PFG) sequence integrated with stimulated echoes. This experiment was set up with 4 s of recycle delay, 6 scans, δ and Δ diffusion delays of 4 and 13 ms, respectively, and gradients at increasing strengths (0, 4.5, 17.9, 40.3, 71.7, 161.3, 286.8,

448.1, 645.3, 878.3 and 1147.1 S mm⁻²) in 11 experiments. Since any significant difference in diffusivity was observed by applying gradient pulses in longitudinal (z) or transverse (y) direction, it was assumed an isotropic apparent diffusion in gel samples. Consequently, the gradients for PFG experiments were applied only in the z direction in all cases. Data were analyzed by nonlinear least-squares regression of the equation (Eq 4.3):

$$M_{\rm t} = M_0 \exp \left[-\gamma^2 G^2 \delta^2 \left(\Delta - \delta/3 \right) D \right]$$
 (Eq 4.3)

where M_0 and M_t represent the magnetization intensity resulting after the application of gradients at the minimum and at the i-th strength, respectively, γ is the proton magnetogyric ratio, G is the pulsed field gradient intensity, δ is the duration of the field gradient pulse, and Δ is the time interval between the leading edges of the field gradient pulses.

The MRI images resulted from the acquisition of 8 interlaced axial slices with a width of 1.35 mm, a field of view of $1.33 \times 1.20 \text{ mm}^2$, and 1.07 mm of slice-interdistance. The images consisted of a $256 \times 256 \text{ matrix}$, for T_2 experiment, and a $128 \times 128 \text{ matrix}$, for diffusion and T_1 experiments. ParaVision 5.1 Bruker software was used to process MRI data, attain all the images, calculate T_1 and T_2 relaxation times as well as the apparent diffusion coefficients. All calculations were conducted on nuclear data extrapolated from six ROIs (Region Of Interests) per sample. Briefly, two representative slices *per* sample were considered (mostly the central ones) and, for each of

them, 3 ROIs were selected, possibly accounting for possible spatial inhomogeneity and artifacts. The chosen ROIs consisted in two smaller ($4\cdot10^6$ μ m²) and one larger ($17.2\cdot10^6$ μ m²) circular areas. T_I , T_2 and DIFF data were calculated for each single ROI and averaged for each sample (3 ROIs x 2 slices x sample) (Figure 4.1).

The ANOVA (ANalysis Of VAriance) method was applied to assess the significance of differences (Tukey's Test at an α confidence level of 0.05) detected among studied hydrogels and was carried out by the XLStat software (v.2019, Addinsoft, Paris, France). The letters A, B, C, and D arbitrarily associated as symbols with T1, T2 and DIFF results, indicate whether the differences among tested hydrogels are statistically significant (p-value < 0.05) or not. Specifically, results which differ significantly from each other were marked with different letters, while results which did not exhibit significant differences were marked with the same letter.

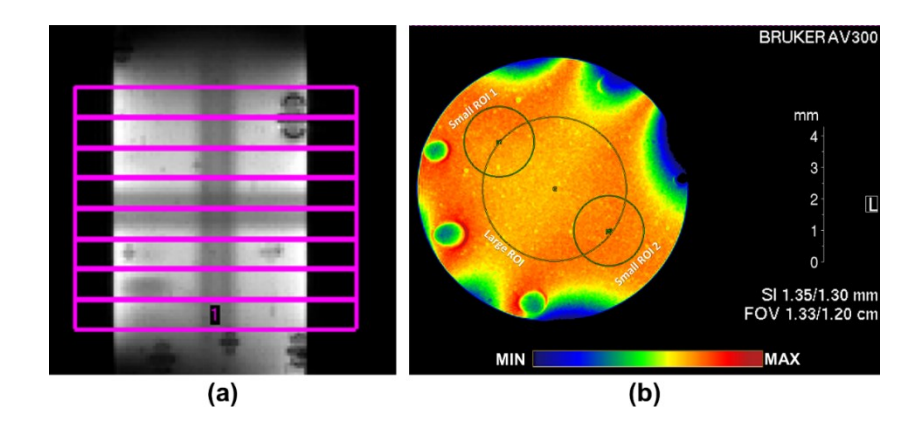


Figure 4.1 a) Slices geometry consisting in 8 interlaced axial slices with a width of 1.35 mm, a field of view of 1.33 \times 1.20 mm2, and 1.07 mm of slice-interdistance. b) The 3 yellow circles show a representative ROIs selection applied to a single slice, consisting of two smaller (4·106 μ m2) and one

larger (17.2·106 μm2) regions. The colour scale indicates the relative spin intensities, ranging from lower (MIN, dark blue) to higher (MAX, red) values.

4.2.2.3 Differential scanning calorimetry

The differential scanning calorimetry were performed by DSC 822e (Mettler Toledo, Germany) while the results were processed by Mettler Toledo STAR^e software.

The analytic protocol involved the use of 40 μ L predrilled aluminium pans filled with a standard mass of materials (3-5 mg). The samples were analysed in form of powders, films, and printed layer particles. The method selected to perform the analysis consisted of a dynamic cycle from 25 °C to 300 °C at a heating rate of 10 °C/min

4.2.2.4 Rheological characterization

Rheological tests were performed using the MCR 102 rheometer (Anton Paar, Austria) equipped with a parallel plate (PP25, with a diameter of 24.985mm), selecting as measuring gap value 0,250mm. Samples were extruded onto the plate through the same syringe used for the printing process and measured after a rest of 1min at 25±1°C. All gels were subjected to both rotational (flow curve and shear test) and oscillatory (amplitude sweep and frequency sweep test) evaluations to obtain information about flow behaviour and viscoelastic properties, respectively. In detail, after preliminary studies, the following operative conditions were used:

• Flow curve (rotational test) with a shear rate range 1*1/s to 100*1/s,

- time dependent viscosity curve (rotational test) at constant shear
 rate (10*1/s),
- amplitude sweep (oscillatory test) in shear strain range between
 0.1% to 250% (constant frequency of 10*1/s),
- frequency sweep (oscillatory test) with an increased angular frequency from 300*1/s to 0.01*1/s (constant amplitude in the LVER established thanks to the amplitude sweep results).

4.2.2.5 Inks spreading measurement

The spreading angle was reported as " θ values" (i.e., left and right angle values between the extruded gel filament and the build plate. In detail, to evaluate the spreading angle of inks, pictures of ink's drop on the build plate were taken after the extrusion and were analysed exploiting the manual point procedure of ImageJ software. These values were taken as a measure of the ink gel accommodation, with higher angles indicating a greater and unwanted spreading of the polymer

4..2.2.6 DDS Digital optimization & SSE printing process

To carry out the printing phase, a cylindrical scaffold was selected as digital model for the platforms a (diameter of 15mm, height of 7.5mm and, final volume of 1.325 cm3). It was processed and optimized through CAM software Cura 4.6.1 (Ultimaker, Netherlands) to obtain the final printing .gcode.

For the printing phase, a semi-solid extruder in PLA, with an exit hole of 800 µm, was produced to perfectly fit with FDM 3D printer Ultimaker3 (Netherlands). The extruder was fixed on the Ultimaker3 printhead and connected with a syringe pump system, Fusion 4000 (Chemix Inc., UK) through a channel. The flow rate was set at 125µL/min, while the printhead speed at 0.75 mm/sec. The extruded forms were left to air dry on a glass slide at room conditions, until a constant weight was reached.

4.2.2.7 Printing resolution and reproducibility

To investigate the resolution and reproducibility of the different manufacturing processes, for all the produced batches the mass and the dimension (diameter "D" and height "H") were analyzed during both steps: post-printing and post-drying. In detail, at least six printed units for each formulation were accurately weighed by digital analytical balance (MX5 micro-balance, Mettler Toledo, Germany) both after printing and after drying. The results of post-printing mass were reported as absolute values (g) with standard deviation; for post-drying mass evaluation, the results were showed thanks to the following equation:

$$M_d$$
 (%) = $\frac{Mass\ after\ drying\ (mg)}{Mass\ after\ printing\ (mg)} * 100$ (Eq 6.4)

Where M_d is the mass variation after drying.

Similarly, the dimensions were analyzed after both steps by digital caliper. the acquired data were used to calculate the process resolution and reproducibility. For the evaluation of shape fidelity after printing, the data were related to the digital dimensions exploiting the equation reported below:

$$D_p (\%) = \frac{D_{Printed model}}{D_{Digital model}} * 100$$
 (Eq 6.5)

$$H_p (\%) = \frac{H_{Printed model}}{H_{Digital model}} * 100$$
 (Eq 6.6)

While, to highlight the impact of drying process on the shape fidelity, the dimension after drying were related to the dimension after printing

$$D_d (\%) = \frac{D_{Dried \ model}}{D_{Printed \ model}} * 100$$
 (Eq 6.7)

$$H_d (\%) = \frac{H_{Dried \ model}}{H_{Printed \ model}} * 100$$
 (Eq 6.8)

4.3 Results and discussion

With the aim to obtain printable ink of alginate, able to maintain its shape after the extrusion, a polymer pre-crosslinking operating procedure was developed and applied during the preparation of the ink gels.

The crosslinking phase, which could be considered as a sol-gel transition, was performed adding to a fixed volume of sodium alginate solution the same volume of water in which different amounts of calcium chloride were solubilized. In details, the egg box formation was due to the displacement of sodium by calcium ions from the binding sites, mainly the carboxyl groups of glucuronate blocks exploiting a zipper mechanism (from unfavourable to favourable binding) (Figure 4.2).

$$Ca^{2+} \longrightarrow Ca^{2+}$$
Alginate blocks
$$Ca^{2+} \longrightarrow Ca^{2+}$$

Figure 4.2 Graphical representation of egg-box formation

To improve the embedding of divalent cations into the forming network and prevent inhomogeneous gels formation, the mixing of sodium alginate solution with calcium chloride was performed under high-speed stirring that potentially increases the calcium distribution. As expected, during the stirring phase, a large amount of air was entrapped, requesting a centrifugation cycle for its removal. The obtained hydrogels, characterized by free from air bubbles and homogeneous matrix, were then stored at 4°C for 16 hours. In table 4.2 the composition of all inks also coupled with the density value are reported.

Table 4.2 Hydrogel inks composition, and density

Code	Alginate (%w/v)	Calcium Chloride (mM)	Density (g/cm³)	
<i>G3</i>	3	-	1.053 ±0.006	
G3_10	3	10	1.015 ±0.009	
G3_12.5	3	12.5	0.999± 0.010	

G3_15	3	15	0.997 ±0.009
G3_18	3	18	0.996 ±0.011
G3_20	3	20	0,997 ±0.014
G3_25	3	25	0.970 ±0.022

To highlight the impact of crosslinking agent on the physical properties of alginate hydrogels, their thermal behaviour was analysed by differential scanning calorimetry. The obtained thermograms are reported in Figure 4.3

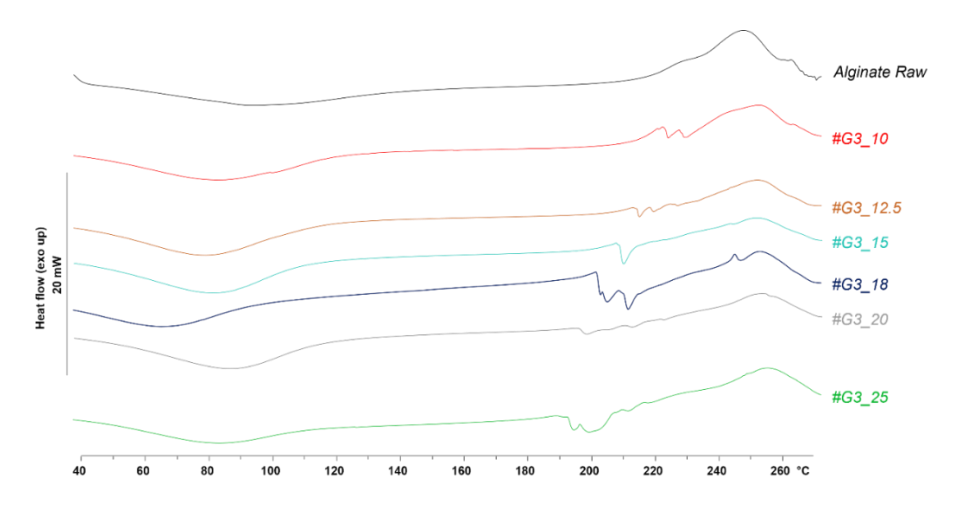


Figure 4.3 DSC thermographs of film obtained from sodium alginate powder (black) and 3% sodium alginate solutions with: 10 mM calcium chloride, #G3_10, (red); 12.5 mM calcium chloride, #G3_12 (light brown); 15 mM calcium chloride, #G3_15 (light blue); 18 mM calcium chloride, #G3_18 (dark blue), 20 mM calcium chloride, #G3_20 (grey); 25 mM calcium chloride, #G3_25 (green).

The sodium alginate (black curve) shows a large endothermic band from 90 to 145°C which underlines the presence of bonded water, and an exothermic peak around 245°C related to the oxidative degradation of alginate polymers.

The calcium-alginate crosslinking led to a slight upward shift of the exothermic band from about 245°C (raw alginate) to 255°C (0.25 mM of calcium chloride) indicative of a greater resistance of calcium alginate to thermal oxidation. Moreover, a shift of the water loss at lower temperature was observed, indicating looser interactions between the alginate and the water, this time only embedded into the polymer network. However, the most interesting region is between 195°C and 220°C showing at least three peaks corresponding to the breakage of calcium-carboxylate bonds in the formed egg-box structure, with broadness and temperature values dependent on the calcium chloride concentration. These peaks converge into one, with 15 mM CaCl₂ (Figure 6.3, green line), probably due to the predominant egg box dimer state. Further increases in calcium determine a re-separation of the peaks and their broadening, demonstrating the coexistence of dimeric and multimeric state, the latter dominant in G3 25 (Fang et al., 2007).

¹H MRI represents a non-invasive NMR spectroscopic technique capable to reconstruct images revealing inner morphological characteristics of intact samples (at a μm level) and, at the same time, provides structural and conformational information based on the amount, location and mobility of water molecules (Nuzzo, Mazzei, Savy, Di Meo, & Piccolo, 2020; Potter, Carpenter, & Hall, 1994; Proietti et al., 2017).

Figure 4.4 shows spin density MRI images of alginate hydrogels obtained through different crosslinker solutions prepared with increasing concentrations of CaCl2 (10, 15, 18, 20 and 25 mM).

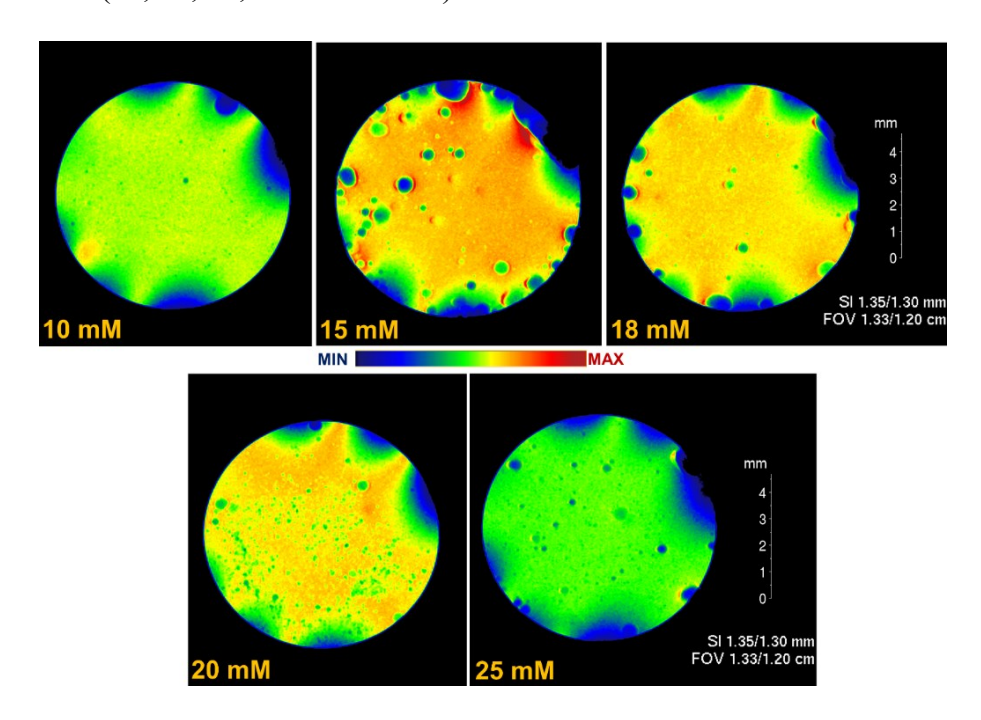


Figure 4.4 MRI images of a representative central axial slice of alginate hydrogels obtained through different crosslinker solutions prepared with increasing concentrations of CaCl₂ (10 mM in #G3_10; 15 mM in #G3_15, 18 mM in #G3_18, 20 mM in #G3_20 and 25 mM in #G3_25). The images were acquired through MSME pulse sequence and resulted from a total spinecho time of 14 ms. The colour scale indicates the relative spin intensities, ranging from lower (MIN, dark blue) to higher (MAX, red) values.

From a visual point of view, almost all axial images exhibited in Figure 4.4 include two types of artifacts consisting of (i) the darker pseudo-circular shapes with a diameter ranging within 0.1 and 1 mm, ascribable to residual air macrobubbles trapped randomly within the gel during the loading into the NMR tube and (ii) the darker semi-ellipsoidal haloes along the borders due to instrumental field inhomogeneity. In all cases, these artifacts were ignored,

being not informative, as well as the ROIs were meticulously built-in areas lacking artifacts.

By comparing the MRI images exhibited in Figure 4.4, the only remarkable difference, in terms of morphology and macroscopic structure, consisted in the average density and diameter of bubbles with a diameter lower than 0.1 mm (referred to as microbubbles, from now on). In fact, it was observed a general distribution of these microbubbles which largely varied according to the used crosslinker concentration. We hypothesized that this aspect may, in part, depend on the variation of Ca-dependent crosslinking level, which, affecting the hydrogel microstructure and its spatial arrangement, hampers, at different extents, the release of entrapped air, thus permitting the accumulation of different-sized microbubbles. In addition, the different colour modulation observed for MRI figures (Figure 4.4) also denoted a change in the overall spin density. In fact, both the distribution of proton signals per relative signal intensity as well as the water content resulting from the integration of spindensity curves revealed a different water response as a function of hydrogel type (Figure 4.5).

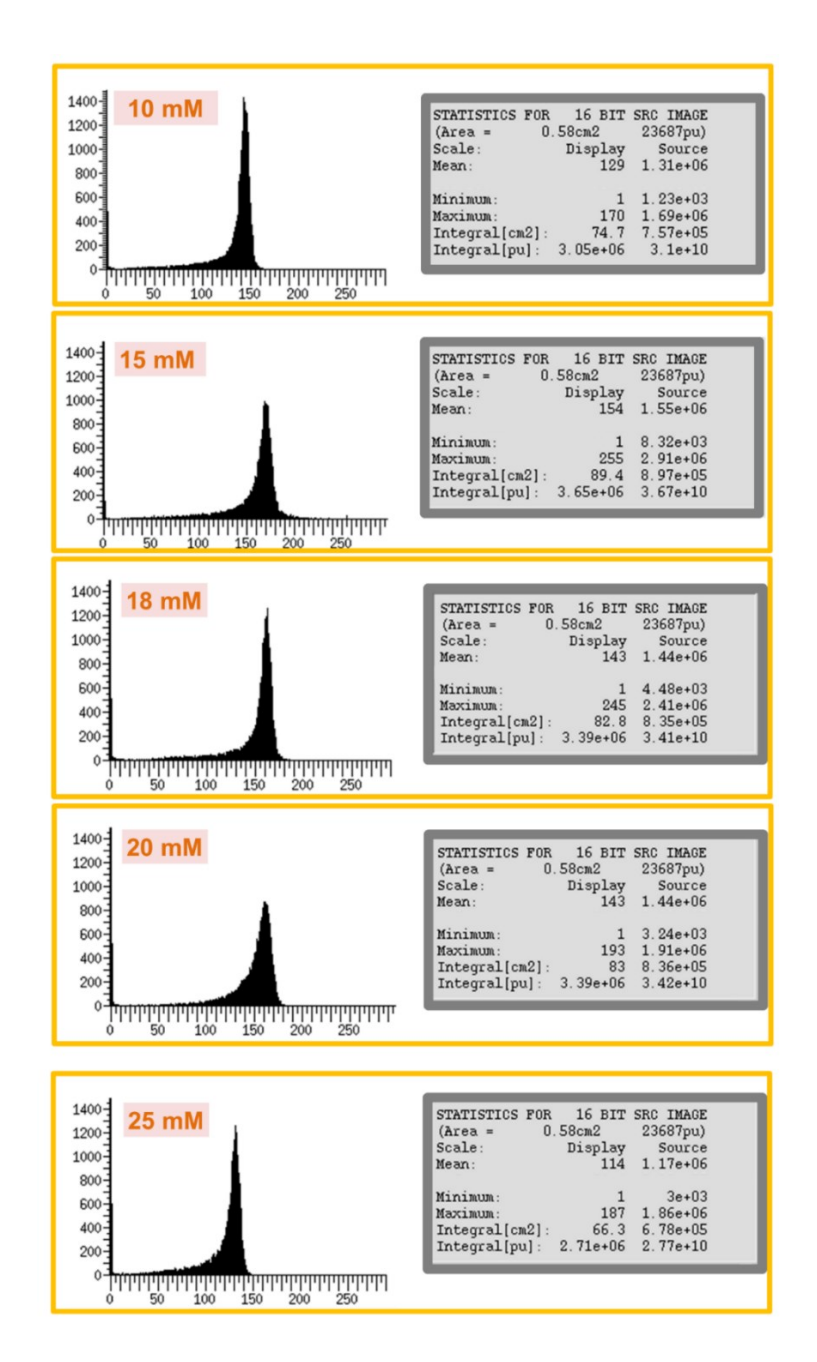


Figure 4.5 Proton spin density evaluation of the MRI images shown in previous figure and related to alginate hydrogels obtained through different crosslinker solutions containing CaCl2 (10 mM in #G3_10; 15 mM in #G3_15, 18 mM in in #G3_18, 20 mM in #G3_20 and 25 mM in #G3_25). For each hydrogel is reported the distribution of proton signals per signal intensity (curves on the left-side) associated with the corresponding integration data (boxes on the right-side)

In detail, the integration of sample 10 mM curve revealed an area of 77.4 cm2 with the largest distribution of protons corresponding to the relative intensity of \approx 140. Areas for samples 15, 18 and 20 mM corresponded to 89.4, 82.8 and 83 cm², respectively, with curve modes ranging within 160-170, thus representing the hydrogels with the largest areas and the highest intensities. Finally, the smallest area was recorded for sample 25 mM, associated to a curve mode at a relative intensity of 130. As the MRI proton spin density indicates the water content per volume-unit, the highest intensities observed for samples 15, 18 and 20 mM may be attributed to (i) the formation of a gel structured in such a way to enable the access of a larger amount of water per hydrogel volume-unit (ii), a lower number of micro- and nanobubbles of air. Interestingly, the broader curves detected for samples 15 and 20 mM also suggested a slightly more heterogeneous distribution of protons in these two samples, attributable to a different Ca-depending gelation extent.

It was also conducted an evaluation of the proton relaxation times of studied hydrogels aiming to better understand the Ca-dependent process of alginate gelation. Conceptually, immediately after the MRI excitation phase, the water proton nuclei recover the equilibrium state by releasing the energy in the form of a radiowave through a relaxation process. The latter is driven by the energy loss from the excited nuclear spin to either the lattice, through an intermolecular transfer (longitudinal or spin-lattice T1 relaxation), or to other spins, through an intramolecular transfer (transversal or spin-spin T2

relaxation) (Levitt, 2013; Zhao et al., 2017). The complex dynamics influencing such energy loss and the extent of relaxation rates are dependent on the specific environment experienced by the excited nucleus. It can be generalized that relatively long T₁ and T relaxation times typically correspond to water molecules characterized by a fast tumbling rate (tending to a free-state), while short relaxation times are indicative of slower tumbling rates, resulting from either tight water interaction with solid surfaces or a confinement in relatively restricted material compartments (Degrassi, Toffanin, Paoletti, & Hall, 1998; Gruwel, Yang, de Gervai, Sun, & Kupriyanov, 2009; Nuzzo, Mazzei, Drosos, & Piccolo, 2020). T₁ and T₂ relaxation times of studied hydrogels (Figure 4.6) unveiled a generalized and significant decrease of both spin-lattice and spin-spin relaxation times as a function of calcium concentration.

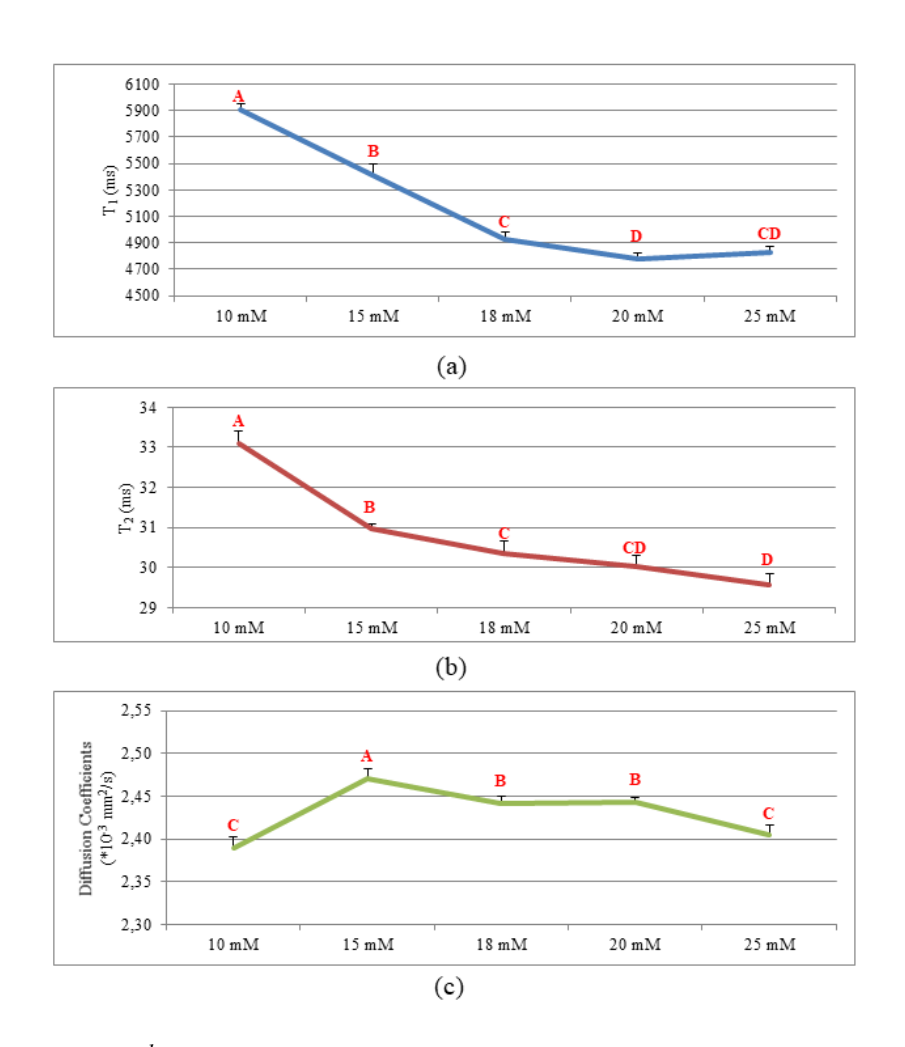


Figure **4.6** ¹H NMR Spin-lattice (a), Spin-spin (b) relaxation times and self-diffusion coefficients (c) of alginate hydrogels obtained through different crosslinker solutions prepared with increasing concentrations of CaCl2 (10 mM in #G3_10; 15 mM in #G3_15, 18 mM in in #G3_18, 20 mM in #G3_20 and 25 mM in #G3_25). Figures include, for each measure, the standard deviation as well as the results of ANOVA Tukey's test (red letters A-D), where hydrogels with no common letters are significantly different from each other at a 0.05 confidence level (95% of significance).

In detail, T₁ values decreased almost progressively from 5906 (sample 10 mM) to 4774 (sample 20 mM) ms, corresponding to a reduction of the 19.1%. A progressive and enhanced decrease occurred from 10 mM to 20 mM samples, followed by only a slight and not significant increase for sample 25

mM, (Figure 4.6a). Analogously, the T₂ values also exhibited a drastic decline form 33.1 (sample 10 mM) to 29.58 ms (sample 25 mM), corresponding to a decrease of the 10.6% (Figure 4.6b). Specifically, the most enhanced diminution occurred from sample 10 (33.1 ms) to 15 mM (30.98 ms). The T₂ values calculated for samples 18, 20 and 25 mM showed a progressive but very slight further decrease which did not reach values lower than 29.58 ms. In all cases it was observed a relatively low standard deviation within each sample, thus suggesting a discrete spatial homogeneity, in terms of structure and physico-chemical properties. This evidence well agrees with the spin-density curves characterized by a single peak in all cases (Figure 4.5).

Assuming a reliable reproducibility in the gel preparation, both types of relaxation times are expected to be almost constant (Levitt, 2013). Given this, the observed sample-depending changes may be considered as diagnostic parameters revealing an alteration in water mobility as well as a variation in the chemical environment experimented by water molecules composing the hydrogel liquid-phase. In general terms, the faster the tumbling rate of examined water molecules, the longer both the relaxation times and *viceversa* (Mazzei, Cozzolino, & Piccolo, 2018). The progressive decrease of these two nuclear parameters may indicate a slower movement of water included in the hydrogel reticule, probably attributable to a more enhanced Ca-dependent crosslinking. Such a crosslinking extent may have led to an increase in the molar fraction of water characterized by a slower tumbling rate due to a more

pronounced confinement within the scaffold (Degrassi et al., 1998; Zhao et al., 2017). Moreover, the fact that both T₁ and T₂ values showed the most enhanced decrease from sample 10 to 18 mM, beyond confirming the well-known role played by the calcium in such an ionotropic gelation, suggests that the calcium content impacts drastically the gelation up to a concentration of 18 mM while higher concentrations of calcium only slightly further influence the structure. Interestingly, the presence of micro and nanobubbles of air may represent a further minority factor co-responsible for the progressive reduction of both relaxation times. In fact, their presence determines a local magnetic susceptibility which indirectly accelerates the relaxation process.

Diffusion coefficients (DIFF) permit to estimate the apparent translational self-diffusion of water molecules within the gel scaffold, thus indirectly indicating the extent of free diffusion within the studied matrix. Consequently, Diff are expected to decrease when water molecules experience barriers to diffusion (such as relatively rigid polysaccharidic structures), interact with gel structure, or are forced to diffuse within relatively small-sized pores. Conversely, Diff values increase if water molecules can move more freely into a less crosslinked matrix, because of a longer free diffusion distance (Degrassi et al., 1998; Zhao et al., 2017)

In figure 4.6c the results of Diff values calculated for the produced alginate hydrogels are displayed. Also, the diffusivity changed according to the type of studied sample, although the extent of these variations did not result as

enhanced as for relaxation times. In particular, the lowest diffusivity was recorded for the sample 10 mM, with a Diff value of 2.39·10-3 mm²/s. Conversely, the sample 15 mM showed the highest DIFF value (2.471·10-3 mm2/s), thus suggesting a more enhanced mobility of water, presumably ascribable to the newly formed hydrogel structure. Then, samples 18 and 20 mM showed, invariably, a DIFF of $\approx 2.44 \cdot 10-3$ mm2/s, while the sample 25 mM exhibited a DIFF of 2.405·10-3 mm2/s. The interpretation of these data must consider that the diffusion coefficients calculated for a representative ROI correspond to the averaged values of different populations of water molecules, each with a specific mobility (i.e., relatively free water, water molecules tightly interacting with polar polysaccharide surface and water molecules confined in a multimer clusterization). The fact that the diffusivity decreased from samples 15 to 25 mM may be simply justified by a more pronounced reticular crosslinking promoted by calcium which led to a diminution of the relative abundance of free water. However, about the value observed for 10 mM, it can be inferred that the ratio Ca/Guluronic acid is not enough to match the critical value required for the development of the typical "egg-box" formation (Fang et al., 2007; Grant, 1973), thus determining a larger dispersion of Ca-monocomplexes, whose weak interactions may, overall, cause a spread barrier to water diffusion.

Conversely, the initial formation of clusters at 15 mM may translate in the coexistence of still few crosslinked domains (characterized by a low total

diffusivity) surrounded by peripheral regions characterized by a faster diffusivity. Consequently, it can be hypothesized that at 15 mM the ratio between low diffusivity/high diffusivity regions is unbalanced towards the high diffusivity, while at increasing calcium content (samples 18, 20 and 25 mM) the ratio turns towards a relatively larger amount of more clustered and crosslinked regions.

After the carefully physico-chemical investigation of calcium alginate hydrogel matrices, rheological measurements were carried out to fully characterise the hydrogels or potential ink and to relate their properties with the SSE 3D printing process. Preliminarily, for all hydrogels the viscosity at the rest and the shear viscosity profiles were evaluated via shear rate rotational test. As expected, the viscosity at the rest of sodium alginate gel was the lowest, with minimum variations at different shear rate values compared to the pre-crosslinked gels (Figure 4.7).

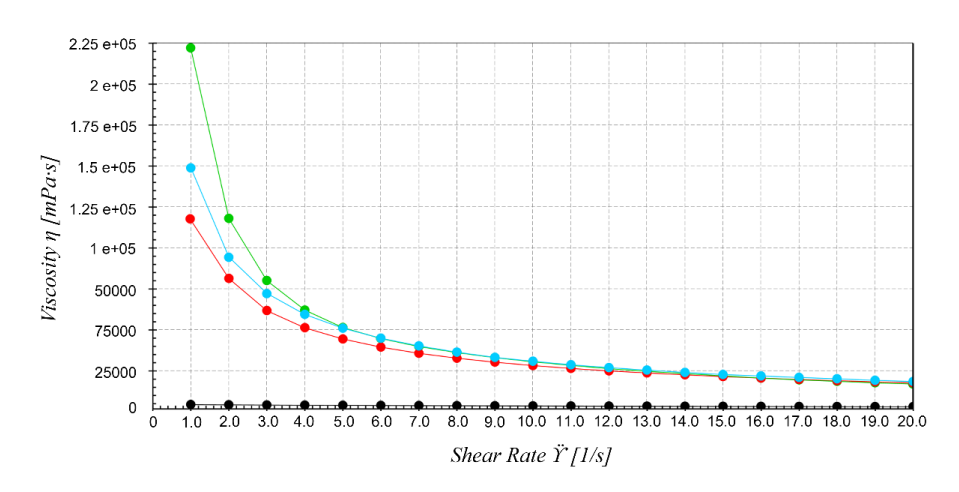


Figure 4.7 Results of rheological characterisation of #G3 (black); #G3_10 (red); #G3_15 (light blue); #G3_25 (green) by rotational test

Differently, these fluids show a shear thinning behavior, with a viscosity decrease of almost three orders of magnitude; moreover, the Newtonian plateau range increased with the calcium concentration. The acquisition of a shear thinning behavior with the pre-crosslinking step is a very important outcome, leading to a printable ink as evidenced by several authors (Heggset et al., 2019; Smith, Basu, Saha, & Nelson, 2018).

With the aim to relate the flow behavior of hydrogels with their extrudability, the viscoelastic properties were analyzed. Firstly, the amplitude test was carried out to highlight the changes in the storage (G') and loss (G'') modules and establish the limit of viscoelastic region (Figure 4.8).

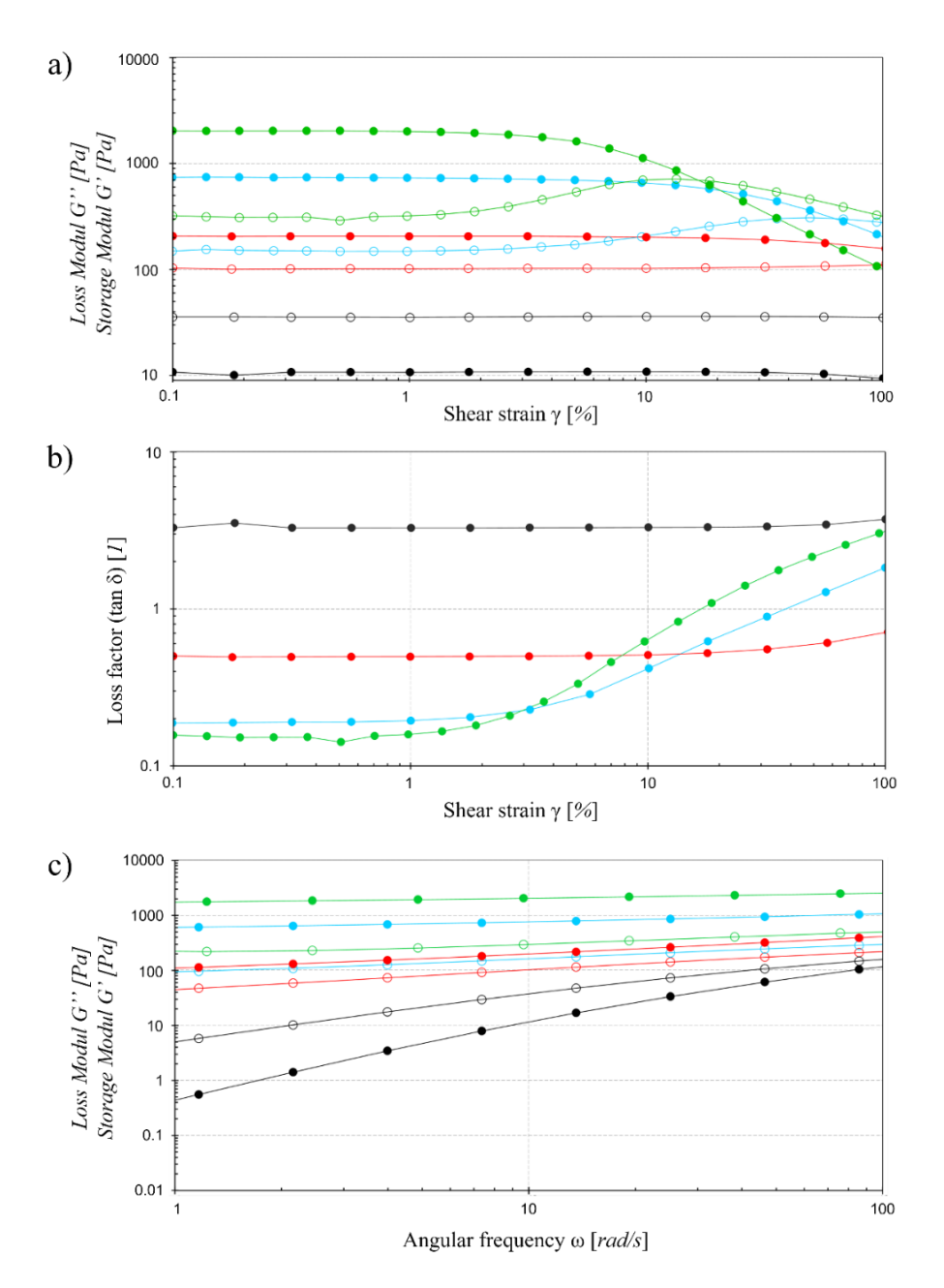


Figure 4.8 Results of rheological characterisation of #G3 (black); #G3_10 (red); #G3_15 (light blue); #G3_25 (green) by oscillatory test: a) storage G' and loss G" moduli evaluated via amplitude sweep test, b) strain dependent tangent of loss factor, and c) frequency sweep test.

The alginate solution has a G'' value always higher than G' $(\tan \delta > 1)$, highlighting the predominance of its liquid characteristics. Contrarily, for all

pre-crosslinked gels at low strain amplitudes G'' is lower than the G' (tanδ <1), confirming the presence of a polymeric network (Ricciardi, Gaillet, Ducouret, Lafuma, & Lauprêtre, 2003). In particular, the increase in calcium concentration led to:

- an increase of the gap between the storage and loss modulus, in agreement with the prevalent gel behaviour;
 - a shift at lower strain values of the crossover point (where G'=G'')
 - a reduction of the linear viscoelastic region (LVER).

Moreover, the slope's increase in the G'' curves (figure 6.8a, empty circles), observed when higher calcium concentrations were used, considers the higher incidence of microcracks in the gel structure, after the shear rate increase.

Particular attention in the rheological study was dedicated to the tan δ (Figure 4.8b), the factor describing the ratio of the two portions of the viscoelastic behavior: for practical applications as SSE, a 0.1<tan δ <1 describes a gel like behavior, with 0.5 value considered as the transition point from a prevalent solid-like to a prevalent liquid behavior (Mezger, 2020). Accordingly, the pre-crosslinking process with calcium shifted the tan δ from values>1 to a minimum value of 0.2 (batch G3_25) with an evident correlation between the calcium concentration and the tan δ value (Table 4.3).

Table 4.3 Loss factor value of each ink at specific shear strain

Code	Loss factor	Loss factor		
Cour	at 0.1% shear strain	at 10% shear strain		
<i>G</i> 3	3.291	3.307		
G3_10	0.500	0.508		
G3_12.5	0.260	0.353		
G3_15	0.188	0.419		
G3_18	0.194	0.583		
G3_20	0.125	0.937		
G3_25	0.157	0.620		

Via frequency sweep test (Figure 4.8c) we also confirmed the processability of the calcium alginate gels, since no variation in the viscoelastic properties were observed.

Finally, knowing the normal force applied by the syringe system pump used for the gel extrusion (7.6 N) the hydrogels rheological performance, in terms of viscosity versus time, at a fixed shear strain value, i.e., 10%, approximately corresponding to the calculated strain to which the fluid undergoes during the extrusion from our system were analyzed. Results (Figure 4.9) suggest a good extrudability for all the pre-crosslinked gels with a calcium concentration

between 0.15 and 0.25, corresponding to both egg-box dimers and multimers interactions.

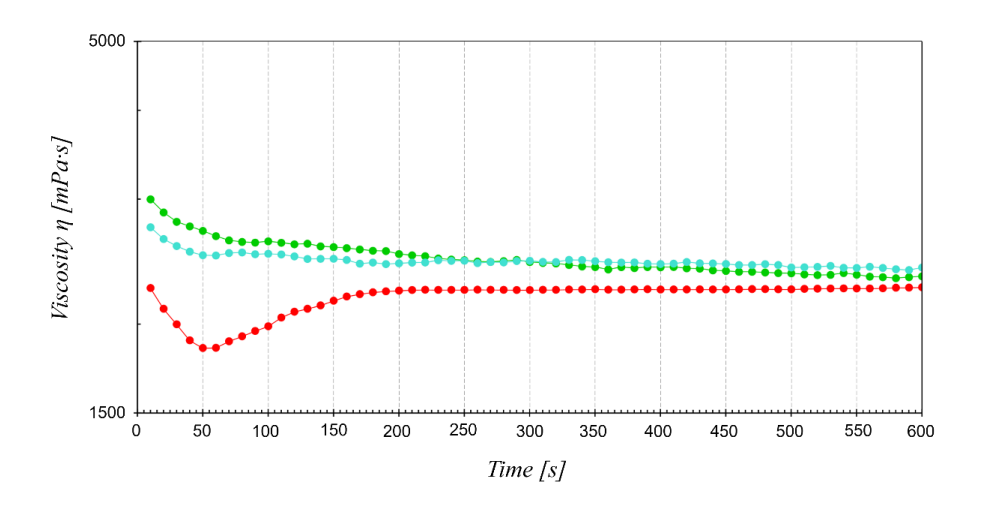


Figure 4.9 Time dependent viscosity curve performed at constant shear rate, samples G3 10 (red); G3 15 (light blue); G3 25 (green)

As described by Paxton, to be considered printable, a gel should lead to the formation of reproducible cylindrical fibres with a good shape retention, which allows the layer-by-layer deposition and the 3D growth of the printed object (Paxton et al., 2017). To check the printability of different alginate inks, their spreading degree was evaluated extruding a 1cm-long gel fibre on the building plate and measuring the left and right angles between the building plate and the outer wall of the fibre (Table 4.4).

Table 4.4 Inks spreading angles (left and right)

Code	θ _l	θ_{R}
	$artheta_L$ (°)	$artheta_R$ (°)
G3	117±2	117±3
G3_10	70±2	71±3
G3_12.5	61±2	57±5
G3_15	56±1	52±3
G3_18	62±5	70±3
G3_20	72±6	59±3
G3_25	69±5	68±3

Only G3 (Table 4.4) showed angles values >90°, value beyond which the gel cannot be considered self-standing. The calcium treated alginate matrices G3_10, G3_12.5, G3_15 and G3_25 showed comparable values of θ_L and θ_R , demonstrating the good symmetry of the hydrogel fibre during the extrusion on the building plate; while G3_18 and G3_20 showed an increased difference between θ_L and θ_R probably due to a poor homogeneity of the matrix, which may negatively affect the printing process.

Once the pre-crosslinked hydrogels were fully characterized, the aim was to verify the behaviour and developed ability to be extruded by SSE maintaining the shape using process parameters defined during preliminary tests.

In agreement with the shear thinning behaviour evidenced during the rheological studies, all the gels resulted extrudable, with significant differences in the reproducibility (extruded mass) and in the retention of the shape after extrusion and after drying (in terms of diameter D_d % and H_d % height) (Table 4.5).

Table 4.5 Mass analysis, after printing and after drying, and morphological analysis of all printouts

Code	Mass (g)	$D_p(\%)$	$H_p(\%)$	M_d (%)	D_d (%)	H_d (%)
G3_10	1.40	123.3	89.4	3.6	102.1	3.9
	±0.04	±5.7	±5.3	±0.2	±6.21	±0.3
G3_12.5	1.43	107.9	102.4	3.7	97.6	4.5
	±0.02	±3.5	±2.5	±0.4	±4.79	±0.4
G3_15	1.43	109.0	99.3	3.6	98.2	4.8
	±0.05	±3.3	±3.1	±0.3	±5.44	±0.4
G3_18	1.46	110.0	96.3	4.0	96.3	4.6
	±0.05	±3.5	±3.5	±0.4	±5.61	±0.5
G3_20	1.44	109.7	98.7	3.9	89.3	4.8
	±0.10	±3.7	±3.9	±0.5	±5.13	±0.3
G3_25	1.44	111.8	90.0	3.9	44.28	36.06
	±0.04	±2.7	±3.1	±0.1	±2.30	±3.44

At low calcium concentrations (G3_10, 10 mM) it is possible to observe a high spreading of the gel on the printing plate which leads in a short time to the loss of the printing shape, with an increase in diameter and reduction in

height, in comparison with the digital model. This effect can be attributed to the monocomplex state of the alginate matrix, which fails to sustain the weight of the subsequent layers.

Increasing the calcium concentration, the ink extrudability was comparable to that of inks produced at low calcium concentrations, but the shape after printing was more efficiently maintained, demonstrating the shift from the monomeric state to the egg box dimers. However, at concentrations of 20mM the upper limit of the dimeric state, it is possible to observe a lower homogeneity of the ink, as evidenced by higher variations in mass of the extruded gel and by different deposition angles θ_L and θ_R (Table 4.4). Moving to 25mM and, therefore, to the egg box multimers, the ink properties substantially changed with significant differences observed only during the drying step. The egg-box multimeric network that characterize G3 25 in fact, leads a lower collapse along the z axes during the solvent evaporation (critical phase in the less structured matrix) allowing to obtain form with the best shape retention (capacity to preserve the initial ratio between diameter and height of the structure).

After verifying the printability of the pre-crosslinked alginate gels and their different influence on the drying behaviour of the final printed forms, we checked the possibility of using these gels to produce particles loaded platforms. To this aim, a bulk agent (M), was loaded to the alginate hydrogels: G3_15 that showed the best printability, and G3_25 that showed the best shape

retention after drying. In detail the M powder (15-20-25% w/v) was mixed to the SA powder following the geometric dilution of precision method before the hydration phase (first step of inks production protocol) obtaining, before the crosslinking step, a partial dispersion of mannitol in polymeric chains (Table 4.6).

Table **4.6** Mass analysis, after printing and after drying, and morphological analysis of all mannitol loaded printouts

Code	M (%w/v)	Mass (g)	D _p (%)	H _p (%)	M_d (%)	D_d (%)	H _d (%)
		Printed model			L.	Dried model	
G3_15	1.5	1.49	119.1	86.4	15.9	97.3	67.5
	15	±0.10	±4.3	±1.6	±1.2	±4.3	±11.5
G3_15	20	1.50	116.1	91.9	20.6	99.8	89.5
		±0.02	±2.7	±5.7	±0.8	±2.6	±3.3
G3_15	25	1.48	111.9	86.6	24.6	98.3	89.3
	25	±0.04	±2.8	±3.0	±1.6	±1.8	±5.9
G3_25	20	1.51	107.2	89.3	20.8	103.4	81.6
	20	±0.1	±3.0	±1.7	±0.3	±2.0	±2.7

4.4 Conclusion

In this research, the hypothesis of having an alginate hydrogels ready-to-print for Semi-solid extrusion 3D printing, able to maintain the shape after printing and after drying was successfully assessed and confirmed. The polymer pre-crosslinking with calcium chloride improved the printability of alginate matrices, giving them the right shape retention property essential for their use in 3D printing, thus replacing the post-printing curing used up to now.

Advanced analytical techniques, such as DSC and MRI, were employed to identify and highlight important properties of alginate hydrogels, potentially useful to better understand and, at a certain extent, predict the evolution of alginate ionotropic gelation. MRI-based relaxation and diffusion parameters revealed that, according to the pre-crosslinker content, the ionotropic gelation led to the development of materials with different properties, in terms of structure, spatial arrangement and inner-water mobility. Moreover, the addiction of bulking agent allowed to overcome the matrix collapsing after the drying of the printed forms suggesting that the high embedding capacity hydrogel entanglement could be exploited to load high drug concentration ensuring a good reproducibility of the production process

Application of the 3D printable alginate hydrogels ink for the production of Flurbiprofen loaded personalized DDS

Based on the Article

Falcone, G.; Mazzei, P.; Piccolo, A.; Esposito, T.; Mencherini, T.; Aquino, R.P.; Del Gaudio, P.; Russo, P. Advanced printable hydrogels from pre-crosslinked alginate as a new tool in Semi solid extrusion 3D printing process. Carbohydrate Polymers 2022, 276, 118746.

https://doi.org/10.1016/j.carbpol.2021.118746

5.1 Research aim

Starting from the promising results reached with crosslinked alginate hydrogels, in terms of resolution and reproducibility of the SSE printing process, in this study it was investigated the applicability of these innovative inks as tools for the production of DDS containing flur biprofen for a personalized therapeutic approach.

5.2 Materials & Methods

5.2.1 Materials

Flurbiprofen (FB) (CAS 51543-39-6) (batch n° T17121044, degree of purity: 99.7%), used as model drug, was donated by Recordati S.p.A. (IT-Milano) (Figure 6.1)



Figure 5.1 Flurbiprofen structure

Sodium alginate (SA, CAS 9005-38-3) (with β-d-mannuronic:β-l-guluronic acid ratio of 1.3 and MW > 200000 g/mol),) was purchased from Carlo Erba (Carlo Erba, Milano, Italy); the crosslinking agent "Calcium chloride" (CAS 10043-52-4) was provided by VWR International (VWR International, Milano, Italy). Hydrochloric acid 37% w/w (ACS reagent, CAS 7647-01-0, Sigma-Aldrich, Milano, Italy) and sodium phosphate (CAS 7601-54-9, Sigma-Aldrich, Milano, Italy) were used for the preparation of the dissolution media.

5.2.2 Methods

5.2.2.1 Ink gel production

Flurbiprofen loaded Inks were prepared according to the 4-step protocol established in the previous work, with appropriate amendments. The FB, in form of powder was mixed with sodium alginate powder before the polymer hydration

5.2.2.2 Rheological characterization

To highlight the impact of flurbiprofen addition on the rheological properties of inks and consequentially on their printability, rheological analyses were carried out. In detail, time dependent viscosity curve (rotational test) at constant shear rate (10*1/s), and frequency sweep (oscillatory test) with an increased angular frequency from 300*1/s to 0.01*1/s were performed. The instrument used for the analysis was the MCR 102 rheometer (Anton Paar, Austria) equipped with a parallel plate (PP25, with a diameter of 24.985mm).

5.2.2.3 DDS Digital optimization & SSE printing process

A cylindrical structure was selected for the development of the DDS (diameter of 15mm, height of 7.5mm and, final volume of 1.325 cm³). The printing process was carried out using lab-made extruder fixed on the Ultimaker3 printhead and connected with a syringe pump system, Fusion 4000 (Chemix Inc., UK) through a channel. The flow rate was set at 125μL/min, while the printhead speed at 0.75 mm/sec. The DDS were printed after a scale up and a scale down of volume of digital model through the following equation (Eq 5.1), keeping constant the 2:1 ratio between diameter and height of the model

$$V * f = (D/2)^2 * h * \pi$$
 (Eq 5.1)

where: V is the volume of models; D is the diameter of models; f is the scale multiplier (x0.5, x0.75, x1.5, x2.0); h the height of models.

The data were reported in a graph to highlight the linear relationship between mass and volume of DDS and the process scalability.

5.2.2.4 Printing resolution and reproducibility

To investigate the resolution and reproducibility of the different manufacturing processes, for all the produced batches the mass and the dimension (diameter "D" and height "H") were analyzed during both steps: post-printing and post-drying. In detail, at least six printed units for each formulation were accurately weighed by digital analytical balance (MX5 micro-balance, Mettler Toledo, Germany) both after printing and after drying. The results of post-printing mass were reported as absolute values (g) with standard deviation; for post-drying mass evaluation, the results were showed thanks to the following equation:

$$M_d$$
 (%) = $\frac{Mass\ after\ drying\ (mg)}{Mass\ after\ printing\ (mg)} * 100$ (Eq 5.2)

Where M_d is the mass variation after drying.

Similarly, the dimensions were analyzed after both steps by digital caliper. the acquired data were used to calculate the process resolution and reproducibility. For the evaluation of shape fidelity after printing, the data were related to the digital dimensions exploiting the equation reported below:

$$D_p (\%) = \frac{D_{Printed model}}{D_{Digital model}} * 100$$
 (Eq 5.3)

$$H_p (\%) = \frac{H_{Printed model}}{H_{Digital model}} * 100$$
 (Eq 5.4)

While, to highlight the impact of drying process on the shape fidelity, the dimension after drying were related to the dimension after printing

$$D_d (\%) = \frac{D_{Dried \ model}}{D_{Printed \ model}} * 100$$
 (Eq 5.5)

$$H_d (\%) = \frac{H_{Dried \ model}}{H_{Printed \ model}} * 100$$
 (Eq 5.6)

5.2.2.5 FT-IR analysis

FT-IR analysis was carried out using FT-IR spectrophotometer (Spotlight 400N FT-NIR Imaging System, Perkin Elmer Inc, USA) equipped with an ATR accessory (ZnSe crystal plate) to detect any changes in the drug structure during the printing and drying processes. All the analysed samples i.e., powders, films and printed layer particles were analysed using 128 scans and 1 cm-1 resolution step in the spectral range of 4000-600 cm-1.

5.2.2.6 Drug content analysis and drug-loading efficiency

All the formulations ($n \ge 3$) loaded were evaluated for drug content (DC) and drug loading efficiency (DLE) values.

The DLE (Eq.) has been calculated as:

DLE (%) =
$$\frac{Mass\ of\ PrpHCl\ observed\ (mg)}{Mass\ of\ PrpHCl\ predicted\ (mg)} * 100$$
 (Eq 5.8)

and the DC (Eq.) according to:

$$DC (\%) = \frac{Mass \ of \ PrpHCl \ observed \ (mg)}{Mass \ of \ dryed \ formulation \ (mg)} * 100$$
 (Eq 5.9)

The FB content was detected by UV-vis Spectrophotometer (Evolution 201 UV-vis Spectrophotometer, Thermo Fischer Scientific Inc.) setting the

wavelength (λ) at 247 nm. The PBS calibration curve used for the analysis was in a range of concentration between 10.90 mg/ml and 6.51 mg/ml

5.2.2.7 Dissolution tests

Dissolution tests were performed with USP dissolution Apparatus II (AT7 Smart Dissolution Tester, Sotax Corporation): paddle or basket configuration, 70 rpm stirring, 37 °C, using as dissolution medium in gastro (pH 1.2 ± 0.5) and intestinal (pH 6.8 ± 0.5) simulated fluids, according to USP 36.

For all drug loaded batches, the absorbance values (λ = 247 nm) at different times were measured and related to the API calibration curve (in a range of concentration from 10.5 µg/ml to 65 µg/ml). For all batches analyzed, mean values and standard deviations were reported.

5.2.2.8 Release kinetics fitting studies

Fitting analysis on the release data was performed by using three different kinetic models to clarify release mechanism of the different formulations in accordance with the method proposed by Del Gaudio and colleagues (Del Gaudio et al., 2015). In fact, the linear fitting regression, the Higuchi's model (Eq.5.10) and Peppas-Korsmeyer's equation (Eq. 5.11) were used. To better highlight the impact of calcium concentration the data were normalized as function of surface area.

Higuchi's model is one of the most used to investigate pure Fickian transport, when pure diffusion is the main driving force of the release (Higuchi, 1961)

Higuchi:
$$M_t = A\sqrt{D(2C_0 - C_S)t}$$
 (Eq 5.10)

where Mt is the drug cumulative amount released at time t, t is time, A is the surface area, D the diffusivity of the drug through the matrix, and C0 and Cs are the initial drug concentration and drug solubility, respectively.

The Peppas-Korsmeyer's equation (Ritger & Peppas, 1987) used to mainly explain complex release mechanisms where diffusion is coupled with erosion or swelling of the matrix:

Peppas – Korsmeyer:
$$\frac{M_t}{M_{\infty}} = kt^n$$
 (Eq 5.11)

where $M\infty$ is the drug amount released at infinity, k is a constant, and n is a diffusion coefficient, which depends on geometry of the system and on the release mechanism. When pure diffusion controls the release mechanism n=0.5, whereas when n=1 the release is mechanism is dominated by a case II transport and Eq. 5.11 turns into a zero-order kinetic.

Correlation coefficient corrected for the degree of freedom of the system (r^2_{adj}) and reduced $\chi 2$ Levenberg–Marquardt method for the minimization of the function were used to evaluate the lack of fit.

5.3 Results and discussion

The API selected in this study was the Flurbiprofen, a nonsteroidal antiinflammatory agent ranked as propionic acid derivates. FB is widely used for the treatment of moderate pain accompanied by inflammation; it is dispensed in form of tablets or coated tablet with a dosage range around 100 mg (150-300 mg/die for adult patient, 3/4 mg/kg) (Bulut, 2020; Vemula, Veerareddy, & Devadasu, 2015).

Potentially the personalization of FB tablets in terms of dosage could allow the patient's compliance, also reducing its adverse effects.

The study was carried out comparing two different alginate inks, related to two different calcium-alginate microstructures. Both inks were loaded with 15% w/v of FB to investigate the influence of calcium amount on all the DDS' technological properties. The compositions are reported in Table 5.1

Table 5.1 Composition of inks loaded with Flurbiprofen

Code	Alginate (%w/v)	Calcium Chloride (mM)	Flurbiprofen (%w/v)
G3_15	3	15	15
G3_25	3	25	15

The preliminary step of this work was focused on the optimization of the ink production protocol in accordance with the physiochemical characteristics of Flurbiprofen. The API is characterized by poor water solubility (0.0249 mg/mL), almost ten thousand times lower than the mannitol solubility (229.0

mg/mL), that could negatively affect the particles distribution in the alginate hydrogels. Despite the extremely different water solubilities in comparison to the mannitol, high homogeneity was reached for both drug-loaded crosslinked hydrogels G3_15_FB15, and G3_25_FB15. On the contrary, the poor water solubility of drug prevents the possibility of calcium-drug interaction that would negative affect the three-dimensional entanglement formation. In fact, the high homogeneity was probably due to the high physical embedding capacity of calcium-alginate network that allows the incorporation of API as powder dispersion.

The rheological analysis was exploited as checkpoint for the extrudability of drug-loaded ink (Figure 5.2).

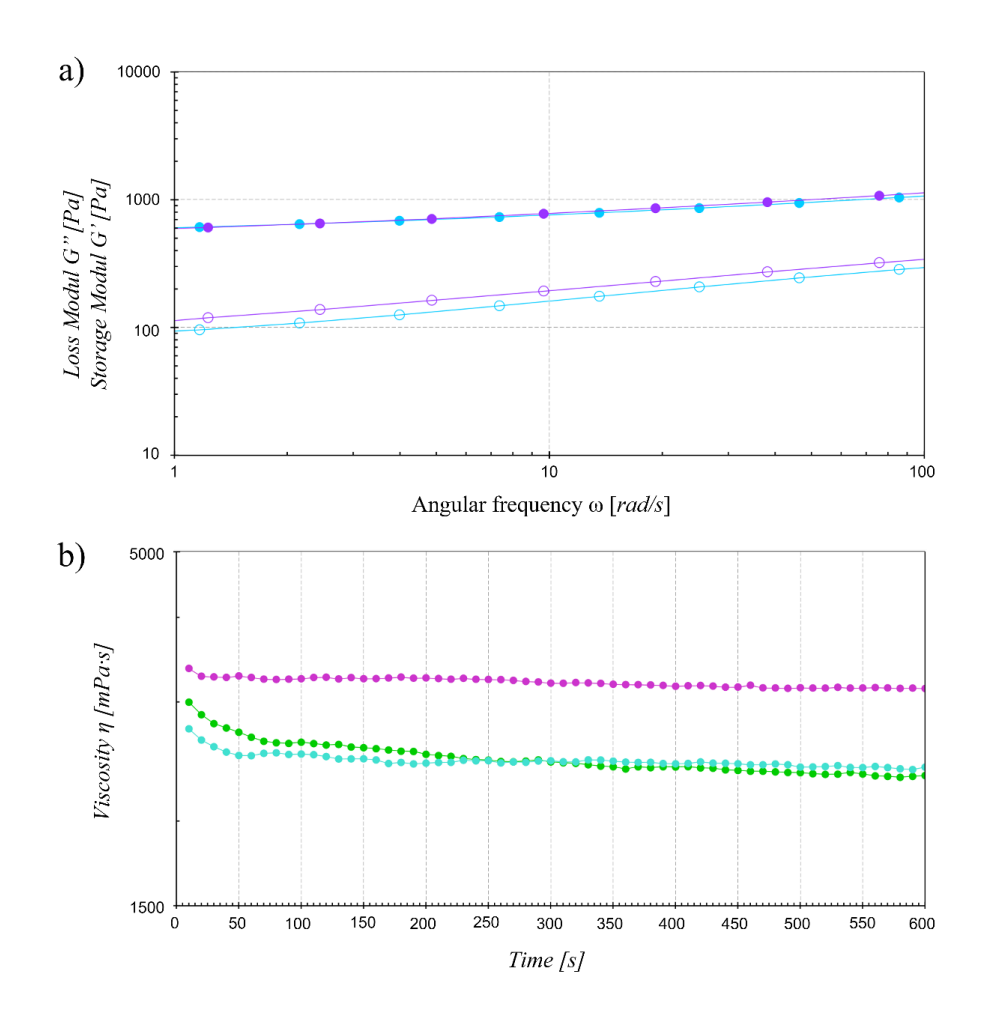


Figure 5.2 comparison of rheological profiles of #G3_15 (light blue) and #G3_15_F15 (violet): a) frequency sweep test, and b) Time dependent viscosity curve at constant shear rate

In Figure 6.2, the comparison of viscoelastic properties of blank and drug-loaded ink during frequency sweep test was reported. As it is possible to observe, the G' and G'' curves of loaded inks were almost superimposable to the blank ones. Moreover, from the comparison of time dependent viscosity curve (Figure 5.2b), an increase in viscosity at rest was highlighted, as expected due the powder addition, while the trend of G3_15 and G3_15_FB15 curves were the same. This result highlighted the homogeneous incorporation

of flurbiprofen in alginate hydrogels in form of dispersion without any changes in the inks' viscoelastic characteristics. After the drug-loaded inks characterization underlining their printability both G3_15_FB15 and G3_25_FB15 were used to produce flurbiprofen loaded printouts (Table 5.2).

Table 5.2 Mass analysis, after printing and after drying, and morphological analysis of Flurbiprofen DDS

Code	FB (%w/v)	Mass (g)	<i>D_p</i> (%)	<i>H_p</i> (%)	M_d (%)	<i>D_d</i> (%)	<i>H_d</i> (%)
		Printed model			Dried model		
G3_15_FB15	15	1.49	108.4	98.1	18.9	94.6	50.1
		±0.08	±3.3	±1.5	±1.0	±2.4	±4.7
G3_25_FB15	15	1.50	111.1	88.1	17.91	82.7	63.6
		±0.04	±1.5	±2.5	±0.7	±7.8	±4.3

As expected from the data acquired about the positive impact of particles addition, the optimal printability of inks (high printing resolution and reproducibility) was reached, as well as the improvement in shape retention after drying was observed for drug loaded forms in comparison with plain alginate platforms.

As a proof of the huge versatility of the SSE production process, the possibility to scaled up and scaled down the dimension of printed forms was evaluated following the equation 5.1. The scaled up and scaled down printed forms showed a predictable mass/volume relationship, useful to produce personalised medicine (Figure 5.3).

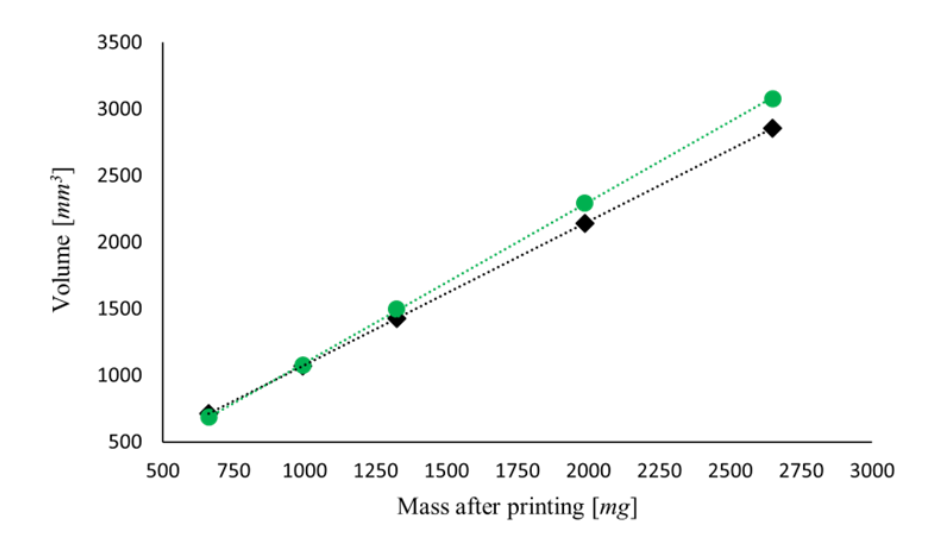


Figure 5.3 Graphical comparison between the ideal printing reproducibility

In fact, by simply scaling the volume of the digital model, using as feedstock
the same drug loaded ink, it is possible to adapt the API dosage loaded in the
printed DDS to the therapeutic needs of a specific patient.

To confirm this hypothesis and understand the potentiality of these new DDS, they were subjected to drug-loading efficiency and drug content analyses (the results were evaluated independently from the different size of printed tablets) (Table 5.3).

Table 5.3 Drug loading efficiency and drug content values of both Flurbiprofen loaded DDS

Code	FB (%w/v)	Drug loading efficiency (%)	Drug content (%)
	1.5	96.68	79.55
G3_15_FB15	15	±6.41	±5.10
G3_25_FB15	15	98.80	81.44
		±1.11	±1.91

Both batches showed drug loading efficiency higher than 90% (96.68± 6.41 % G3_15_FB15, and 98.80±1.11% G3_25_FB15), and a comparable drug content value around 80%. From a macroscopic point of view, these data allow to underline the high potentialities of SSE process in the pharmaceutical field. Focusing the attention on the Standard deviation values, it was possible to observe a reduction of these values for the G3_25_FB15 suggesting the better embedding capacity of egg-box multimeric structure (25mM calcium) in comparison to the egg-box dimeric structure (15mM calcium).

To detect the presence of chemical interaction between API and polymeric matrices FT-IR analysis (Figure 5.4) was carried out.

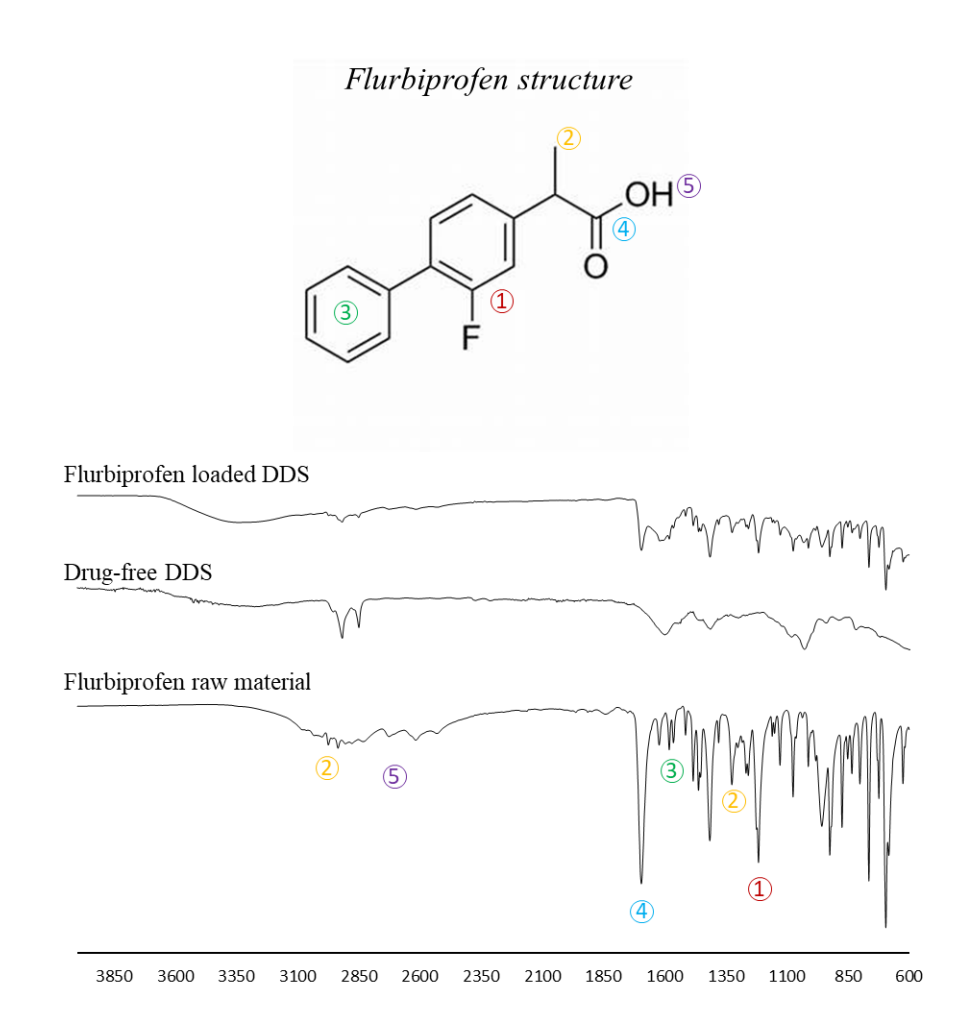


Figure 5.4 FT-IR spectra of (from bottom to top): flurbiprofen raw material, drug-free DDS, and Flurbiprofen loaded DDS. Flurbiprofen structure, with schematic representation of the chemical bonds, was reported to allow data analysis

All the characteristic peaks of FB spectrum were detected in drug loaded DDS without relevant shift: C-F at 1216 cm-1 (peak 1), C-H deformation at 1325 cm-1 (peak 2) and stretch in a range between 2850 and 3050 cm-1 (peak 2), C=C at 1514 cm-1 (peak 3), C=O at 1694 cm-1 (peak 4), and O-H from 2524 to 2730 cm-1 (peak 5) (Vemula et al., 2015).

Finally, to obtain a careful technological characterization of produced DDS, dissolution tests were carried out. The release profiles of both batches G3 15 FB15, and G3 25 FB15 were showed in Figure 5.5.

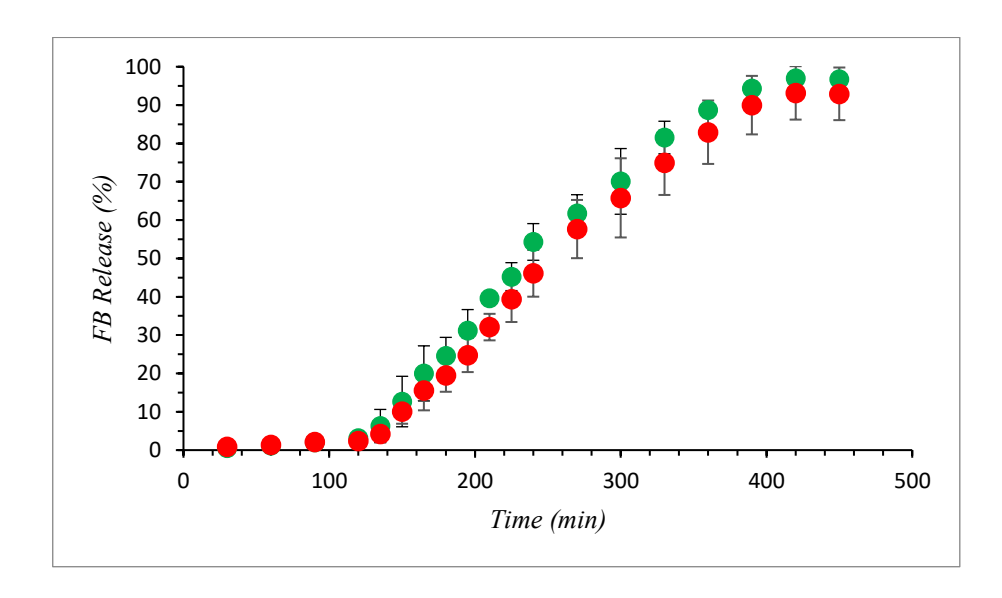


Figure 5.5 Comparison of release profiles from G_25_FB15 (green) and G_15_FB15 (red).

The FB release in gastric medium was found to be very low (less than 5%), In accordance with the information reported in literature about Flurbiprofenalginate DDS, this phenomenon could be due to the combination of poor drug solubilities and the formation of alginate coating characterized by high stiffens and poor swelling capacity at this pH condition (Varma & Hemamalini, 2007). However, the switch of simulated fluid's pH, from 1.2 to 6.8, led to the beginning of matrix dissolution and consequentially the drug release. For both batches, the complete matrix erosion and drug release occurred after six hours in intestinal media. Considering tant many factors such as erosion of polymer,

swelling of matrix, drug diffusion inside the matrix, system geometry (cylinder, sphere, film, etc.) and amount of drug can affect drug release kinetics (Dadsetan et al., 2013), drug release kinetics investigation was carried out to understand the main mechanism involved in the drug release (Table 5.4)

Table **5.4** Fitting results of the kinetic models on the release profiles of Fig. 32, normalized as function of surface area

Model	Higuchi		Zero order**		Korsmeyer-Peppas		
Code	r ² adj (n)*	†Reduce d χ²	r ² adj (n)*	†Reduce d χ²	r ² adj (n)*	†Reduce d χ²	n (S.E.)
G3_15 FB15	0.72	139.24	0.82	109.69	0.90 9	65.91	0.91±0. 1
G3_25 FB15	0.73	132.33	0.84	114.92	0.90	67.58	0.87±0. 1

As shown by the r^2 adj and χ^2 values release of the drug is mainly related to swelling and relaxation of the drug delivery system, with the Higuchi's equation showing worse performance compared to the fitting capacity of the

^{**}Limited to the 85% of release

[†]χ²/DoF as obtained by the Levenberg-Marquardt method

^{*}No release observed in simulated gastric fluid

zero-order kinetic model and Peppas-Korsmeyer's equation (Higuchi, 1961; Peppas & Sahlin, 1989). Moreover, Peppas-Korsmeyer's fitting showed above 0.85 for both formulation (n = 0.91 and n = 0.86, respectively), due the contribution of matrix erosion to the release of the drug (Rodríguez-Dorado et al., 2018). Such values indicate that the mechanism of release can be influenced by the amount of Ca⁺² in the ink resulting in a tougher matrix able to control fluid entry and drug diffusion, which lead to a complex non-Fickian release.

5.4 Conclusion

This study allowed to demonstrate the feasibility to use pre-crosslinked alginate inks in pharmaceutical compounding to produce a new DDS. Thanks to the high embedding capacity of calcium-alginate entanglement it is possible to load high drug amount without any relevant changes in the ink properties. In fact, the SSE 3D printing process can be easily optimized by simple rheological check of ink flowability, reaching the optimal printing performance. The excellent size resolution and the high mass reproducibility could be exploited to produce personalized DDS varying the final amount of loaded drug. Moreover, the drug loading efficiency evaluation underline the efficiency and versatility of the alginate hydrogel as carrier matrices, able to ensure an high level of dosage accuracy (98.80 % ± 1.11). Finally, given the

well-known influence of the alginate matrix structuring on the performance of the produced DDS, it is possible to tune the calcium chloride concentration used in the pre-crosslinking phase also based on the required drug release kinetics.

Application of the 3D printable alginate hydrogels ink for the production of easy to swallow tablets

Based on Submitted Manuscript to Advanced Engineering Materials
Falcone, G.; Kuth, S.; Boccaccini, A.; Aquino, R. P.; Esposito, T,; Russo, P.,
Application of Calcium Alginate Hydrogels in Semi-solid Extrusion 3D
Printing for the Production of Easy-to-Swallow Tablets.

This research project was carried out in collaboration with the Biomaterial Institute of Friedrich Alexander University, Erlangen-Nurnberg

6.1 Scientific background and research aim

Difficulties in swallowing solid medications are common for many people for different reasons: very young or old age, personal phobia, dry mouth state, dysphagia, incapacity in overcoming the instinctive chew and swallow mechanism (Breitkreutz & Boos, 2007; Hanning et al., 2016). The simplistic use of liquid formulations (Zajicek et al., 2013), more easily accepted by a patient, cannot be an adequate solution, given the problems of physio-chemical and microbiological stability (Ruiz et al., 2019). Among the newest drug delivery approaches, minitablets (Stoltenberg & Breitkreutz, 2011), fast dissolving tablets or films (Preis, 2015), and mucoadhesive forms deserve mention (Boateng, 2017; Hoffmann, Breitenbach, & Breitkreutz, 2011; Preis, 2015), but several strategies still be investigated.

To satisfy the ever-growing demand for personalized therapy and to meet the needs of patients with difficulty in swallowing traditional tablets, in this study we wanted to investigate the possibility to develop innovative DDS via 3D printing (Venables, Batchelor, Hodson, Stirling, & Marriott, 2015). In detail, taking advantage from the high embedding capacity of the ready-to-print alginate ink, previously developed (section 4.2), it was speculated the possibility to functionalize it with sorbitol producing sorbitol-alginate soft tablets able to satisfy the swallowability requirements (Venables et al., 2015).

6.2 Materials & Methods

6.2.1 Materials

The materials used to prepare hydrogel inks for Semi-solid extrusion were: sodium alginate (SA) (CAS 9005-38-3, Carlo Erba, Italy) (with β -d-mannuronic: β -l-guluronic acid ratio of 1.3 and MW > 200,000 g/mol), calcium chloride (CAS 10043–52-4), provided by VWR International, Milano, Italy and sorbitol (S) 70% water solution, (CAS 50-70-4, Sigma-Aldrich, Italy), used as polymeric matrix, crosslinking agent and plasticizer, respectively.

The reagents used for the preparation of simulated fluids were:

Sodium chloride (CAS 7647-14-5), hydrochloric acid 37% w/w (ACS reagent, CAS 7647-01-0), and sodium phosphate (CAS 7601-54-9), calcium chloride dihydrate (CAS 10035-04-8), potassium chloride (CAS 7447-40-7), potassium phosphate monobasic (CAS 7778-77-0), potassium phosphate dibasic (CAS 7758-11-4), potassium carbonate (CAS 584-08-7), potassium thioacetate (CAS

10387-40-2) and citric acid (CAS 77-92-9). All reagents were purchased from Sigma-Aldrich, Italy.

6.2.2 Methods

6.2.2.1 3D-printable hydrogels preparation

The 3D-printable alginate hydrogels were prepared following a procedure described in a previous study, with appropriate modifications. Alginate and calcium were hydrated and solubilized, respectively, in a pre-settled volume of water to reach the following concentrations: alginate solution 3% w/v and calcium solution 25mM. These solutions were mixed (1/1 v/v ratio) under homogenization (10 RPM for 120 s) to promote the crosslinking process. Sorbitol was then slowly added into the crosslinked hydrogel under gentle mixture, until a homogeneous distribution was reached. The obtained hydrogels were centrifuged (2500 RPM for 10 min) and stored (16 hours at 4°C). The final compositions of hydrogel inks are reported in Table 6.1.

Table 6.1 Composition of inks (alginate-sorbitol hydrogels)

	Functional excipients				
Code	Alginate (% w/v)				
F25			-		
F25_S5	2	25	5		
F25_S15	3	25	15		
F25_S25			25		

6.2.2.2 Rheological evaluation of 3D printable hydrogels

The knowledge needed to understand the hydrogels extrusion properties and to optimize the printing process derives from different rheological studies, each providing significant information. In detail:

- Flow curve: evaluation of viscosity behavior varying a shear rate (γ^*) from 0.01 to 10 1/s (logarithmic representation)
- > (CSD): varying the shear strain from 0.1 % to 100 % at a constant frequency of 10 1/s
- ➤ Creep and recovery measurement: the creep phase was carried out with a constant shear stress at 5 Pa for 200 seconds, the same time lapse during which the recovery was evaluated

All tests were performed with the same set of parameters: measuring gap (0.250 mm), plate temperature (30.0±0.5°C) using the MCR 102 rheometer (Anton Paar, Austria) equipped with a parallel plate (PP25, with a diameter of 24.985 mm)

6.2.2.3 Inks spreading measurement

Method was developed to evaluate the spreading angle, and the fiber circularity from all hydrogel inks. The spreading angle was reported as " θE values" (the average of the angle, i.e. left and right angle values between the extruded gel filament and the build plate); while fiber circularity was defined by the "e value", which considers the fitting of the area described by the fiber

section with the area of a circumference with the same radius. The spreading angle, and the fiber circularity of all hydrogel inks were evaluated exploiting the manual point procedure of ImageJ software (Figure 6.1). In detail, pictures of the hydrogels on the build plate were taken 15 sec after the extrusion.

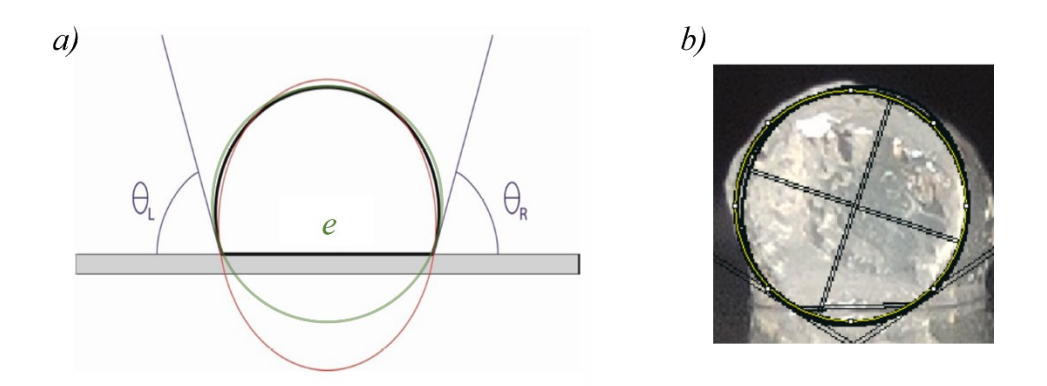


Figure 6.1 a) Schematic representation of parameters analysed in the spreading angle measurement, b) screenshot Image J software during the hydrogel fibre evaluation

In accordance with the information proposed by Schubert (Schubert, 2022) about the impact of build plate material on the self-standing of extruded fibers, three different surfaces, with different surface characteristics were evaluated, i.e. Glass Petri dish (CellInk, Sweden), Polystyrene Petri dish (Sterilin Ltd, Great Britain) raw and coated with vegetable oils spray for grassing (rapeseed, grapeseed, and palmeseed) approved for food application (Solchim S.r.l., Itay).

6.2.2.4 Printability evaluation

To identify the best printing pressure for each hydrogel ink, in accordance with the different sorbitol concentration, two different outcomes were evaluated: ink flowability, evaluated measuring the ink mass extruded in a

second, and layer width fidelity. In detail, using a monolayer model with the same pattern of the drug delivery system (DDS) model, all hydrogels were tested (ten times for each hydrogel) at different extrusion pressures in a range between 20 to 30 KPa. To obtain the ink flowability, the printed masses were accurately weighed by analytical balance and related to the printing time. The line width fidelity (LWF) was obtained comparing the line width measured by ImageJ software using pictures acquired immediately after printing, and the needle diameter (Needle 21G=0.51mm), according to the equation 6.1:

$$LWF (1) = \frac{Measured line width (mm)}{Needle diameter (mm)}$$
 (Eq 6.1)

6.2.2.5 DDS Digital optimization & SSE printing process

The DDS printing was carried out using the BioX 3D-bioprinter by CellInk (CellInk, Sweden). The software used for the development of the three-dimensional DDS model was Rhinoceros 6 CAD software. The model was a cylindrical structure with the diameter at the base of 10 mm and the height of 5 mm. The slicing and printing process were optimized by the HeartOS 1.4 Software developed by CellInk. The CAM modelling provided the grid as pattern with infill percentage of 50, and a layer height of 0.51 mm (Figure 6.2). For all inks a printing temperature of 30.0±0.2°C and a print speed of 15mm/sec were fixed, while the printing pressure was tuned in accordance

with the different printing performance of each ink: 22 KPa, 27 KPa, 30 KPa, and 32 KPa for F25 S25, F25 S15, F25 S5, and F25 respectively.

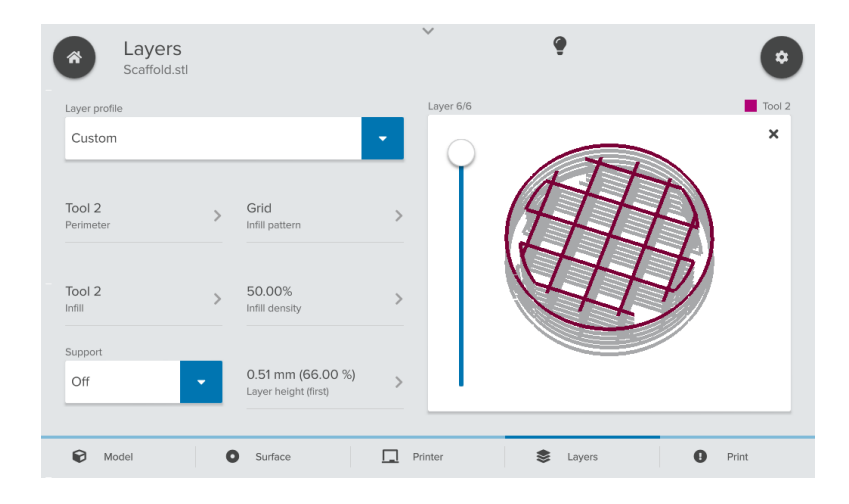


Figure **6.2** Screenshot of the HeartOS 1.4 Software. Recap of the slicing parameters

6.2.2.6 3D-printed platforms resolution and reproducibility

To evaluate the printing performance of different hydrogel-inks, the mass was weighed by analytical balance, while the diameter (D) and the height (h) were accurately measured by digital calibre for each printed sample. These dimensions were used to calculate the volume of the model V (Equation 6.2)

$$V = (D/2)^2 * h * \pi$$
 (Eq 6.2)

Then, the Shape fidelity (SF) was evaluated comparing the printed volume to the volume calculated from the digital model, in accordance with the following equation

$$SF (\%) = \frac{Volume \ of \ Printed \ Platform \ (mm^3)}{Volume \ of \ Platform \ digital \ model \ (mm^3)} * 100$$
 (Eq 6.3)

The results were shown in form of histograms with standard deviations.

6.2.2.7 Drying impact: morphological and mass analysis

To quantify the mass reduction and the shape changes of the printed forms after the drying process, the dried printouts were weighed and these values were related to the mass after printing, while the dimensions were compared to post–printing dimensions. The data were reported as a percentage ratio, according to the following Equations:

$$M_d$$
 (%) = $\frac{Platform\ Mass\ after\ drying\ (mg)}{Platform\ Mass\ after\ printing\ (mg)} * 100$ (Eq. 6.4)

$$D_d (\%) = \frac{D_{Dried \, model}}{D_{Printed \, model}} * 100$$
 (Eq. 6.5)

$$(\%) = \frac{H_{Dried\ model}}{H_{Printed\ model}} *100$$
 (Eq. 6.6)

6.2.2.8 Morphological analysis

Macroscopic images of the final platforms were obtained by single-lens reflex camera (Canon EOS 600D), while microscopic images, at different magnification (x1.25, x4) were acquired by means of Carl Zeiss STEMI 508 microscope and evaluated with ZEN 3.2 (blue edition) software.

6.2.2.9 Platforms mechanical characterization

The mechanical properties of all platforms were determined by parallel plate compression test (MicroTester LT, CellScale, Canada) (Figure 6.3).



Figure **6.3** MicroTester LT by CellScale (https://www.cellscale.com/products/microtester/)

Before measurements, samples were immersed in saliva simulating fluid (prepared following the method proposed by Duffo & Castillo (Duffo & Castillo, 2004) at pH 6.5±0.2) for 30 s and pat dried. Two different tests were performed, determining Young's modulus and adhesion force. Firstly, the samples were compressed to a maximum force of 0.55 N with a loading time of 20 s. Each sample (at least 5 for each batch) was compressed for 4 cycles. To determine the adhesion force, the probe was loaded with a negative compression (aka tension) at the end of the fourth compression cycle and the measure was stopped once the probe detached from the sample. All measurements were performed in air at room temperature. The Young's modulus was determined by the slope of the linear fit of the stress-strain curve

in the range of 1-3 % of samples compression. The software used for fitting analysis was GraphPad Prism 9

6.2.2.10 Media induced matrix behavior

To highlight the impact of sorbitol on the technological properties of the platforms matrix, all batches (at list minimum 3 samples for each one) were subjected to in vitro test using a USP dissolution Apparatus II, in paddle configuration (70 rpm) (AT7 Smart Dissolution Tester, Sotax Corporation). In detail, the changes in the platforms mass during the residence in gastro (120 min at pH 1.2 ± 0.5) and intestinal (pH 6.8 ± 0.5) simulated fluids at 37 ± 0.5 °C were investigated. At specific time points, until a complete matrix disintegration, samples were withdrawn from the vessel, deprived of the medium excess, and weighed using analytical balance. The mass variation was calculated in percentage following the Equation 6.7 reported below:

Mass Variation (%) =
$$\frac{DDS \ mass \ (ti)}{Dried \ DDS \ mass} *100$$
 (Equation 6.7)

where *DDS mass* (ti) means the mass value at specific time from 0 to 300 min

The results were reported in form of graph.

6.2.2.11 Statistical analysis

All the statistical analyses were conducted using GraphPad Prism 9 software. For the fitting evaluation of the printability and morphological variation a simple linear regression model was used. Confidence interval selected was 95% with a p value <0.05.

6.3 Results and discussion

Sorbitol is a hexahydro alcohol (Figure 6.4), derived from natural source, available in form of powder as well as syrupy liquid, widely used as excipient both in food and in pharmaceutical compounds (Sheskey, Cook, & Cable, 2017).

Figure **6.4** Sorbitol structure

Due to its hygroscopic nature that increase the water retention, the main use of sorbitol is plasticizer agent. Moreover, the sorbitol is also used as a sweeting agent improving the tablet palatability, one of the most important parameters that improves the patient's compliance. Another interesting property related to the hygroscopicity of sorbitol was the potential improvement of tablets dissolution rate, that could be exploited to modify the matrix behaviour in vivo and the drug release kinetics (Goyanes, Souto, & Martínez-Pacheco, 2010) However, the hydroxyl groups of sorbitol could negatively affect the crosslinking reaction between alginate and calcium. For

this reason, the sorbitol was used in form of liquid solution and added (in three different ratio 5-15-25% v/v) into the hydrogel previously crosslinked.

Given the close relationship between the rheological properties of hydrogels and their printability, all the developed inks were subjected to rheological characterization (Hazur et al., 2020; Sonnleitner, Schrüfer, Berglund, Schubert, & Lang, 2021) Firstly, a controlled shear rate test was performed to highlight the ink-flow behaviour in comparison to the previously develop hydrogel (Figure 6.5 a). Each hydrogel showed a constant decrease in the viscosity value, with a speed-dependent viscosity ratio higher than 1, typical of the shear thinning behaviour, a crucial property for a 3D printing application. Thanks to the evaluation of rheo-graphs with the Bingham equation (Bingham, 1917) for the yield determination the effect of different amount of sorbitol was investigated, highlighting an inverse relationship between sorbitol concentration and yield point. As known, hydrogels are characterized by a three-dimensional network that give to the polymeric matrix a viscoelastic behaviour; for this reason, oscillatory (CSD) and translational test were also carried out. Figure 6.5b is the graphical representation of results obtained by CSD amplitude sweep test. It was exploited to detect the limit of linear viscoelastic (LVE) range, below which the structure of the sample shows no significant change.

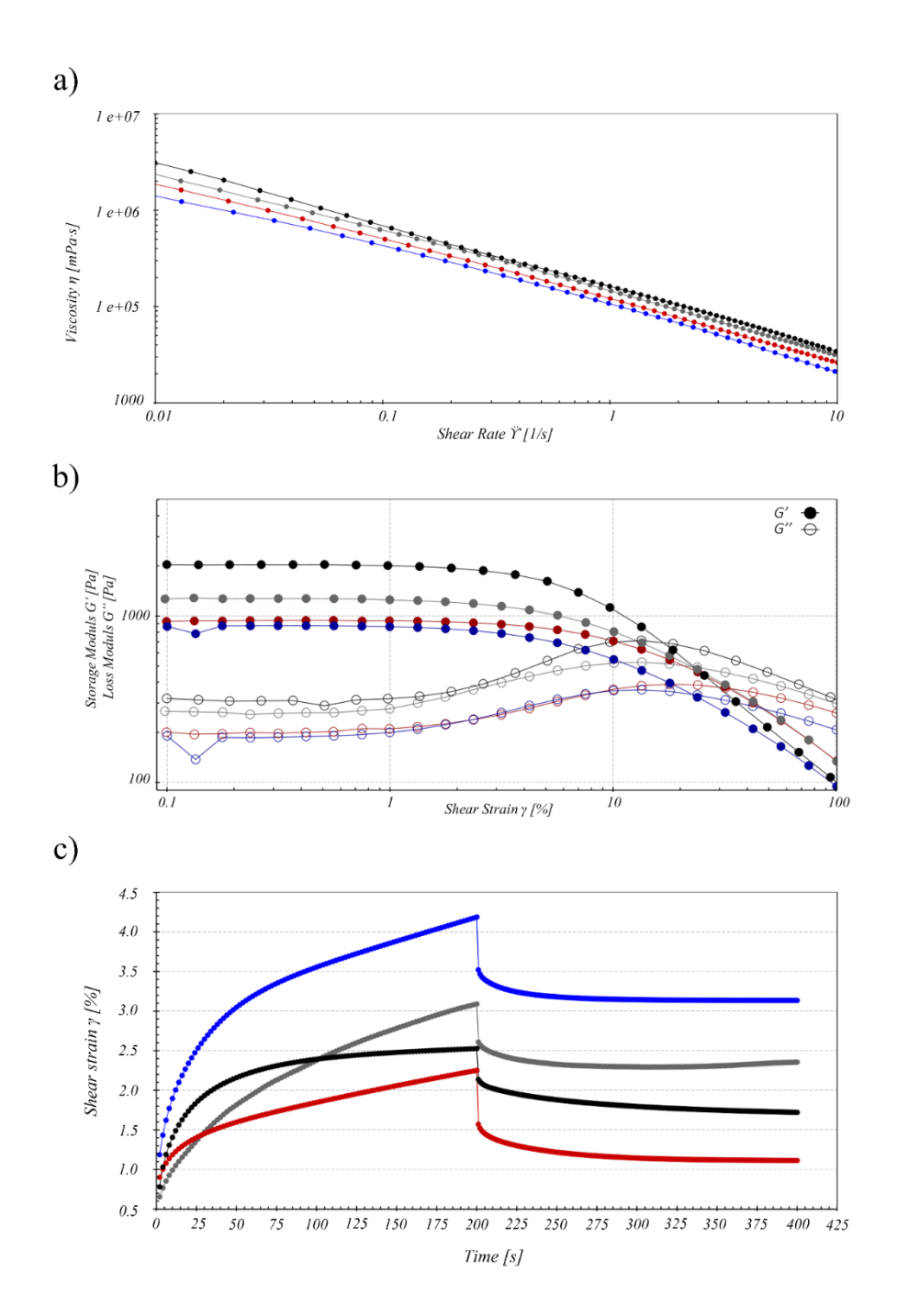


Figure **6.5**. Rheological evaluation of inks: F25 (black), F25_S5 (grey), F25_S15 (red), F25_S25 (blue). a) flow sweep curve: viscosity as function of shear rate; b) oscillatory evaluation of storage G' and loss G'' moduli as function of shear strain; c) transient analysis (creeping and recovery) deformation as function of time with constant shear stress

All the inks showed a similar linear viscoelastic region, with a dominant elastic behaviour in the low-shear range, underlining the gel-like consistency of all inks. On the contrary, each ink showed a different viscous behaviour and crossover point.

Through the comparison of ink curves with the calcium-alginate raw ink (F25, black curve) it was possible to highlight that the addition of sorbitol led to:

- a decrease of G' and G'' values at rest
- an increase of the LVE region from 1.9 to 4.2% of strain (with a limit of G' decrease settled at 5%) (Mezger, 2020)
- a shift of crossover points at higher strain values
- a reduction of G" curve slope, highlighting the reduction of the internal friction.

In detail, the maximum extension of non-relevant deformation region was reached for F25_S5 and F25_S15, while F25_S25 shows a reduction of this region (limit of LVE region at 3.2% of strain). Moreover, F25_S25, at low strain showed a poor linearity of G'' curve, describing an inhomogeneous deformation that could suggest the negative impact on the ink's rheological properties of the highest amount of sorbitol loaded. Finally, to obtain a carefully characterization of the inks, they were subjected to the measurement of the time-dependent deformation function $\gamma(t)$, analyzing the viscoelastic

behavior during two shear stress steps, i.e. both deformation and reformation (Figure 6.5c). The curve obtained from both steps allowed to understand the balance between elastic and viscous components that influence both the hydrogel extrudability and the printouts resolution (Gao et al., 2015) As it is possible to observe in Figure 6.5c, the changes in the transient properties of the hydrogels did not show a predictable relationship with sorbitol addition. The incorporation of 5% sorbitol (F25 S5) did not change the elastic portion of hydrogel, while had an important effect on the viscous ones, with a growth of about 100%. A further increase in sorbitol content (15% in batch F25 S15) improved the gel recovery properties as evidenced by the increase of elastic recovery of around 85%, which dropped down again with gels containing 25% of sorbitol solution. In F25 S25, in fact, the viscous portion overcome again the elastic ones and showed the highest strain value, over the linear viscoelastic limit.

All together these results suggest that a 5% sorbitol solution is not sufficient to fill the alginate matrix, crosslinked with calcium before its addition, giving rise to an inhomogeneous distribution of the excipient into the ink-gel. At the opposite, a 25% of sorbitol is overabundant, some of it remaining outside the alginate matrix.

Another of the main parameters that negatively affect the final resolution of the material extrusion 3D printing is the spreading of the fiber immediately after deposition. This becomes crucial if the starting material is a hydrogel that

is strictly influenced by many variables such us flow rate, wettability, and surface charge. In detail, Schubert explains that for a water-based system like hydrogels the impact of surface tension between fiber and print bed is the most relevant phenomenon that affect the layer spreading (Schubert, 2022) For this reason, we decided to analyze the inks spreading evaluating three different print-bed surfaces. i.e., glass, plastic, and oily covered surface. Based on these assumptions, the spreading angle as well as the circularity of hydrogel fiber were analyzed (Table 6.2). Generally, the pre-crosslinking approach exploited for the inks preparation ensured a good self-standing for all tested hydrogels $(\theta_e < 90^\circ)$. The hydrophobic surface, where the hydrogels surface charge did not affect the wettability, allowed for a better shape retention of the filament after deposition onto the printing plate, with higher circularity and reduced spreading angles for any of the sorbitol concentration. Moreover, for the hydrophobic surface, the effect of sorbitol was higher and gradual as its concentration increases, while for plastic and glass the reduction in circularity and spreading angle was evident already at the lowest excipient concentration. The non-relevant influence of sorbitol increase in the spreading angle on glass and plastic was due to the non-relevant impact of sorbitol on surface tension.

Table **6.2** Ink spreading evaluation: spreading angle (θ_e) and circularity value (e)

Codo	Build plate materials		
Code	Glass	Plastic	Oily surface

	θ _e (°)	e (1)	θ _e (°)	e (1)	θ _e (°)	e (1)
F25	65.2±0.7	0.89	52.2±1.2	0.91	29.5±0.4	0.97
F25_S5	76.2±3.2	0.78	68.7±2.5	0.82	33.4±1.2	0.95
F25_S15	82.7±3.6	0.75	71.6±0.9	0.80	48.3±1.6	0.92
F25_S25	79.4±1.0	0.72	73.9±3.3	0.82	61.4±3.0	0.86

This hypotesis was in line with the results obtained from the ink flowability and line width fidelity tests, performed to evaluate the inks printing performance at different printing pressures and optimize for each one the best experimental conditions.

In particular for both flowability and line with fidelity, a linear relationship with the printing pressure has been obtained (Figure 6.6).

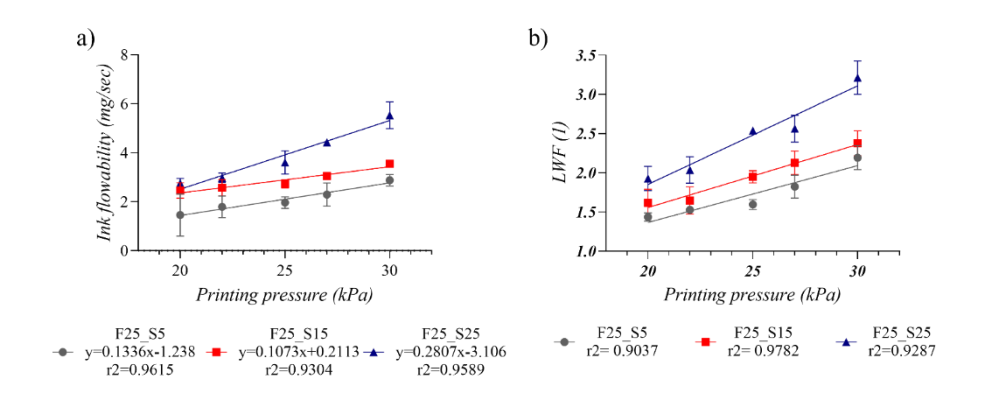


Figure **6.6** Graphical report of printability parameters a) ink flowability, and b) layer width fidelity., F25_S5 grey marker, F25_S15 red marker, and F25_S25 blue marker

As for ink flowability, F25_S5 and F25_S25 showed higher standard deviations compared to F25_S15, highlighting once again the poor ink

homogeneity and a less predictable behavior of these hydrogels when extruded. Moreover, performing a simple linear regression of the collected data, F25_S25 showed a higher slope value, indicating a greater impact of sorbitol on printing performance. Similar results were obtained with the LWF test. In fact, as expected from literature report on material spreading after Semi-solid extrusion onto a printing plate, line width fidelity always higher than 1 were obtained, with an enlargement of the extruded filament diameter that increased with the printing pressure (Paxton et al., 2017) This effect was less reproducible and predictable when 5% and 25% of sorbitol solution was used, as underlined by r² values lower than 0.95. The At the end of the printability evaluation, through the variation of the slicing parameters (infill density at 50%) in accordance with ink properties previously described a high printing

resolution for the final platforms, described by shape fidelity (Figure 6.7) was reached starting from all the tested inks.

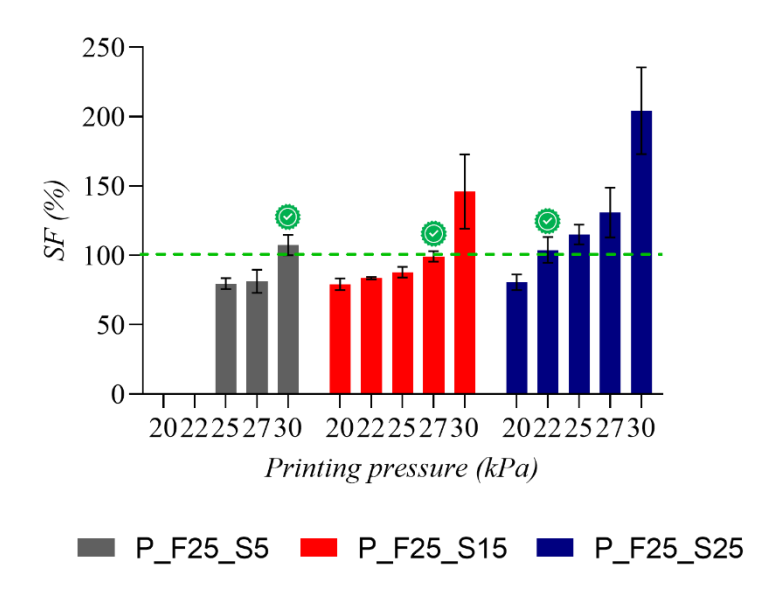


Figure 6.7 Shape fidelity evaluation of platforms obtained from different alginate-sorbitol inks as function of printing pressure. F25_S5 grey data set, F25_S15 red data set, and F25_S25 blue data set

Interestingly, the printing pressure value giving the best shape fidelity decreased with sorbitol content increase into the alginate crosslinked inks from 32 KPa for F25, to 30 KPa (F25_S5) to 27 KPa (F25_S15) and 22 KPa (F25_S25). For all the inks the dimensional standard deviation was lower than 10% (7.5%, 3.7%, and 9.3% for P_F25_S5, P_F25_S15, and P_F25_S25, respectively); moreover, the average of printed masses, calculated independently from the ink used, showed a standard deviation lower than 5%

in agreement with traditional mass uniformity requirement reported in pharmacopeia (mass average 384.07±19.15 mg)

After the printing step, all platforms were subjected to airdrying process to highlight the impact of sorbitol on the mass variation and the shape retention (Figure 6.8) (Table 6.3) (Heggset et al., 2019).

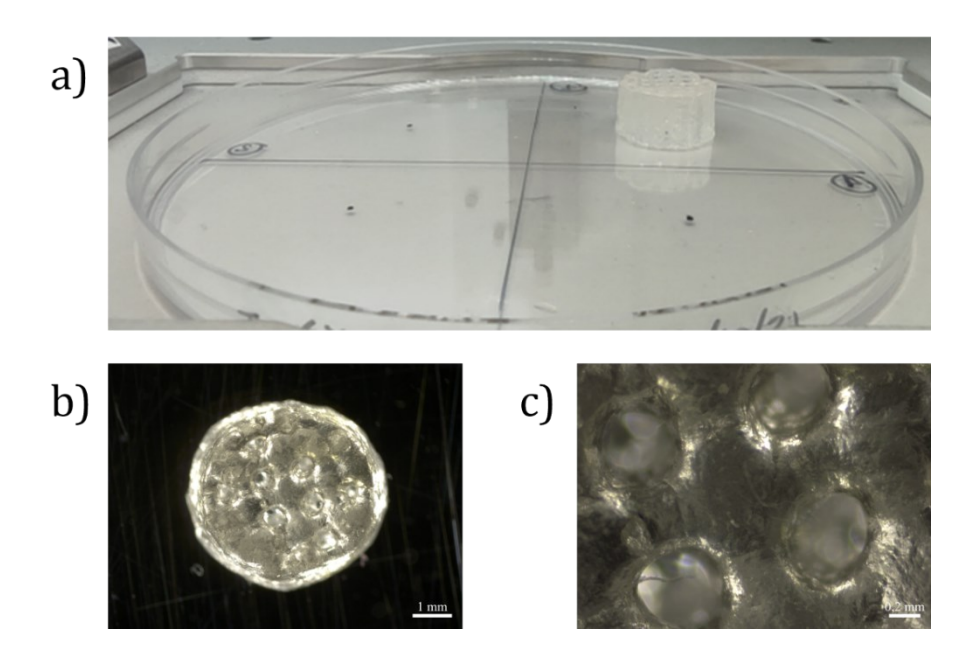


Figure 6.8 a) Photo of platform immediately after printing. Microscopic acquisition of dried platform b) mag 1.25x, and c) mag 4x

As expected from the results described in previous section the addition of an excipient into the hydrogel matrix, improves the shape retention. The residual mass after drying increased with the sorbitol content into the inks, confirming the ability of the preformed alginate matrix to load compatible ingredients also in high amount. Also, the shape retainment after drying was influenced by the sorbitol content, with an increase in both residual diameter and height. However, it is important to underline that the ratio between diameter and height was maintained also unchanged among different batches, demonstrating that the sorbitol did not favor the spreading onto the printing plate during the platforms drying. This predictability could be exploited for the platforms customization in accordance with patients' needs. In accordance with the swallowability requirements, all the dried batches, except for P_F25_S25, fulfilled the dimension limits with a final diameter less than 6 mm. Nevertheless, this dimensional limit can be easily predicted and overcome optimizing the digital model.

Table 6.3 Evaluation of mass and shape of DDS after drying process

Code	Residual weight Diameter (S		Height (%)
	(%)		
P_F25	3.9 ± 0.1	44.3 ± 2.3	36.1 ± 3.4
P_F25_S5	7.9±0.5	44.1±1.9	38.2±1.9
P_F25_S15	16.5±0.9	55.5±1.2	47.0±4.5
P_F25_S25	23.6±0.7	62.9±3.0	53.3±3.6

As described at the beginning of this section, sorbitol is particularly useful as functional excipient in the chewable tablet because it combines the plasticizer effect with a sweet taste (Bolhuis, Rexwinkel, & Zuurman, 2009). For this reason, to investigate the impact of plasticizer addition and relate it to the tablet swallowability, all developed platforms were subjected to mechanical characterization evaluating the matrices' deformability (Figure 6.9), described by the Young's modulus. From a macroscopic point of view,

our platforms compared to the conventional tablets showed a matrix elasticity similar to soft and chewable tablets (Ambros, Podczeck, Podczeck, & Newton, 1998; Dille, Hattrem, & Draget, 2018). Moreover, focusing on figure 7.9a, it was possible to observe a relevant decrease in the Young's modulus moving from P_F25_S5 (1982±521 KPa), that showed also the highest standard deviation, to P_F25_S15 (554±74 KPa); as noticed for other inks and DDS properties, a further addition of sorbitol did not result in a further decrease in Young's modulus (P F25 S25, 543±33 KPa).

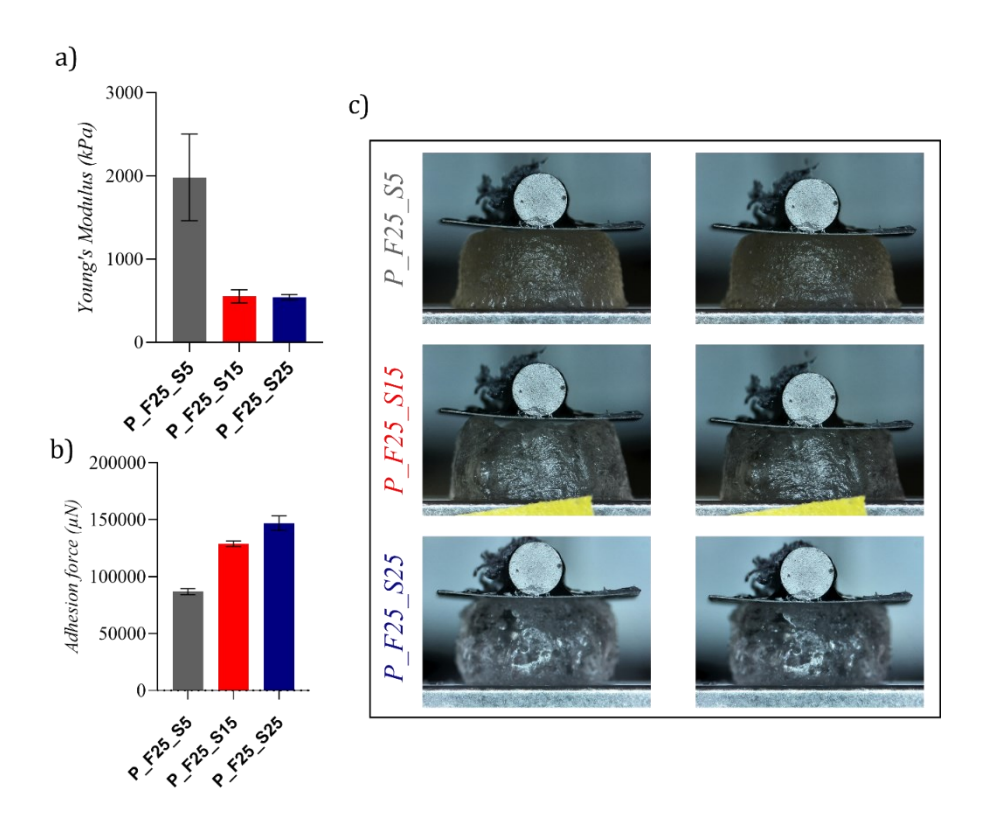


Figure 6.9 Mechanical properties study of P_F25_S5, P_F25_S15, and P_F25_S25: a) Young's modulus and b) adhesion force. c) MicroTester LT software acquisition of platforms derived from each hydrogel: acquisition "at the beginning of the test" (left side) and "at the maximum compression point" (right side)

To date some problems about accidental adhesion of tablets during esophageal transit remain (Swisher, Sendelbeck, & Fara, 1984). For this reason, another interesting parameter evaluated during the mechanical characterization was the adhesivity of the matrix (Drumond & Stegemann, 2018) Marvola et al identified as limit of adhesivity force approximately 1.5 N (Marvola, Vahervuo, Sothmann, Marttila, & Rajaniemi, 1982). The results of the adhesion test (Figure 6.9b) showed the opposite trend in comparison with Young's modulus values, highlighting this time a slight difference also between P_F25_S15 and P_F25_S25. In fact, the additional amount of sorbitol used in the ink F25_S25 not only affected the soft-ability of the matrix but it led to a further increase in the adhesivity, due to the increased hygroscopicity, next to the limits identified for the swallowability (Marvola et al., 1982).

Finally, to predict the fate of platforms after oral administration in vivo, the matrix behavior in simulated fluids was evaluated (Figure 6.10).

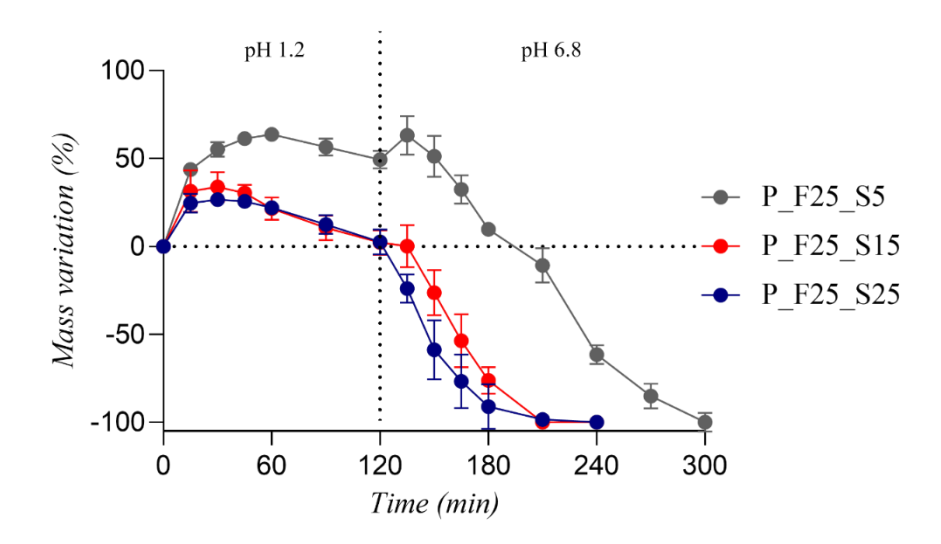


Figure **6.10** Curves obtained by media induced matrix behavior investigation. P_F25_S5 grey line, P_F25_S15 red line, and P_F25_S25 blue line

In detail, the balance with the medium up-take capacity and the erosion of the matrix was investigated underlining the role of sorbitol not only as plasticizer but also as disaggregate agent. In fact, the behavior of each curve could be divided in two steps, the first characterized by the mass increase probably related to the swelling of the matrix, and a second step more evident after the pH change in which the matrix erosion was predominant. Increasing the sorbitol amount from 5 to 155, it was possible to observe a decrease around 50% of the maximum of mass acquired, due to the reduction of swelling properties of the matrix and/or an increase of the disaggregation. The matrix disaggregation in P_F25_S15 is more relevant also in intestinal medium, leading to a remarkable reduction in the time needed for the complete matrix erosion (from 210' to 300'). Moreover, P_F25_S5 showed an increase of the

mass immediately after the shift of pH, a phenomenon characteristic of alginate matrix. Again, a further increase of sorbitol from 15 to 25 % v/v did not affect the matrix interaction with simulated fluids. properties of the platforms. The variation in technological properties of platforms could be considered during the setting of the best therapeutic approach.

6.4 Conclusion

When dealing with oral administration of solid dosage forms, one of the main problem remains the swallowability; in view of the production of DDS patient's tailored, this issue has to be overcome. To this aim, exploiting the high manufacturing flexibility of 3D printing technique, in combination with a careful rheological characterization, the hydrogel printability has been optimised as function of printing pressure, enabling the development of platforms with high shape fidelity independently from the inks' composition. On one hand, the tuning of sorbitol concentration allows for the production of a softer matrix, removing the plasticky aspect typical of dosage forms obtained by 3D printing, with a hopefully improvement of patient's compliance. On the other hand, the possibility to predict the variation of inks printability and matrix properties with the changes in alginate gel composition acquired after this research maximizes the versatility of this technology, moving an important step towards a ready-to-print pharmaceutical ink, for the production of dosage

forms with peculiar characteristics such us shapes, palatability, and swelling/erosion properties after the interaction with biological fluids.

7 Conclusion & Perspectives

The Ph.D. project aimed to demonstrate the potentialities of Semi-solid extrusion 3D printing as pioneering production process in pharmaceutical field to develop innovative and personalized drug delivery systems, using alginate as feedstock material. In particular, two different strategies were conceived, developed and followed, both aimed at overcoming the problems that prevent alginate from its use in SSE-3D printing.

Thanks to a careful rheological characterization of the starting materials and a consequent fine tuning of the printing parameters, both strategies were successfully applied for the production of customizable pharmaceutical forms, even floating ones, suitable for the administration of different active ingredients.

This represents an important step towards obtaining a ready-to-use alginate ink able to load customizable amounts of different active ingredients, as well as functional excipients that easily allow to define the final properties of the printed DDS, from gastro-resistant, to gastro-retentive and easy-to-swallow tablets.

Focusing on the future perspective, this project could be considered for as the first chapter of a wider research context, discovering on the long way of 3D printing application in the pharmaceutical field.

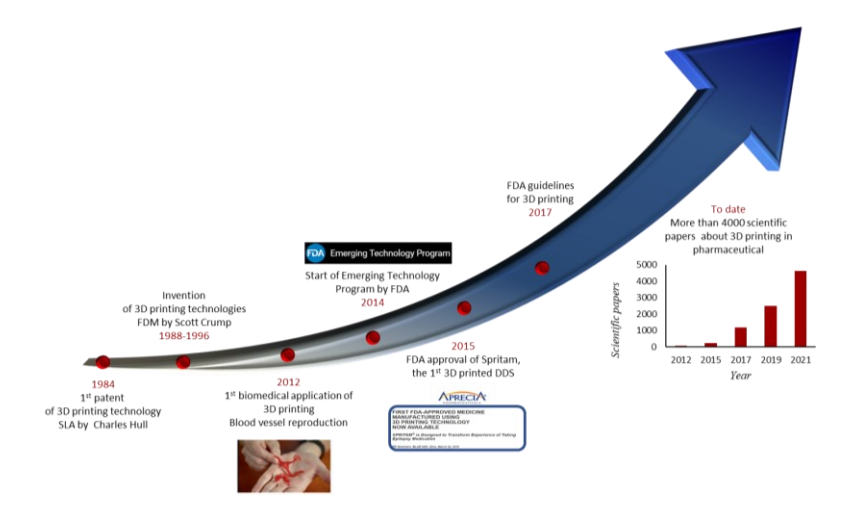


Figure 9.1 Timeline of 3D printing in pharmaceutical field. What will be the next step?

Starting from the promising results about the application of alginate hydrogels to produce innovative personalized DDS via Semi-solid extrusion 3D printing, further studies will be necessary to fulfil the requirements of personalized medicine such us the expansion of the number of APIs and excipients investigated in relation to the several potential applications of printed DDS. At the same time, particular attention must be paid to establish guidelines that describe the safety procedure of all steps of the 3D printing workflow allowing to overcome the regulatory limitations on 3D printing for personalised medicine developing.

Bibliography

- Administration, U. F. D. (2013). Paving the way for personalized medicine: FDA's role in a new era of medical product development. *Silver Spring, MD: US Food Drug Administration*.
- Alhijjaj, M., Belton, P., & Qi, S. (2016). An investigation into the use of polymer blends to improve the printability of and regulate drug release from pharmaceutical solid dispersions prepared via fused deposition modeling (FDM) 3D printing. *European Journal of Pharmaceutics Biopharmaceutics*, 108, 111-125.
- Amante, C., Esposito, T., Del Gaudio, P., Di Sarno, V., Porta, A., Tosco,
 A., Russo, P., Nicolais, L., Aquino, R. P. (2021). A Novel Three-Polysaccharide Blend In Situ Gelling Powder for Wound Healing Applications. *Pharmaceutics*, 13(10), 1680.
- Ambros, M. C., Podczeck, F., Podczeck, H., & Newton, J. M. (1998). The characterization of the mechanical strength of chewable tablets. *Pharmaceutical Development Technology*, 3(4), 509-515.

- Amir-Aslani, A., & Mangematin. (2010). The future of drug discovery and development: shifting emphasis towards personalized medicine.

 Technological Forecasting Social Change 77(2), 203-217.
- Aquino, R. P., Barile, S., Grasso, A., & Saviano, M. (2018). Envisioning smart and sustainable healthcare: 3D Printing technologies for personalized medication. *Futures*, 103, 35-50.
- Auriemma, G., Russo, P., Del Gaudio, P., García-González, C. A., Landín, M., & Aquino, R. P. (2020). Technologies and formulation design of polysaccharide-based hydrogels for drug delivery. *Molecules*, 25(14), 3156.
- Awad, A., Trenfield, S. J., Gaisford, S., & Basit, A. W. (2018). 3D printed medicines: A new branch of digital healthcare. *International Journal of Pharmaceutics*, 548(1), 586-596.
- Awad, A., Trenfield, S. J., Goyanes, A., Gaisford, S., & Basit, A. W. (2018).

 Reshaping drug development using 3D printing. *Drug discovery today*,
 23(8), 1547-1555.
- Axpe, E., & Oyen, M. L. (2016). Applications of alginate-based bioinks in 3D bioprinting. *International journal of molecular sciences*, 17(12), 1976.

- Balakrishnan, B., & Jayakrishnan, A. (2005). Self-cross-linking biopolymers as injectable in situ forming biodegradable scaffolds. *Biomaterials*, 26(18), 3941-3951.
- Bartolomei, M., Bertocchi, P., Ramusino, M. C., & Signoretti, E. C. (1998).

 Thermal studies on the polymorphic modifications of (R, S) propranolol hydrochloride. *Thermochimica acta*, 321(1-2), 43-52.
- Barui, S. (2021). 3D inkjet printing of biomaterials: Principles and applications. *Medical Devices Sensors*, 4(1), e10143.
- Basit, A. W., & Gaisford, S. (2018). 3D printing of pharmaceuticals: Springer.
- Bingham, E. C. (1917). An investigation of the laws of plastic flow: US Government Printing Office.
- Boateng, J. (2017). Drug delivery innovations to address global health challenges for pediatric and geriatric populations (through improvements in patient compliance). *Journal of Pharmaceutical Sciences* 106(11), 3188-3198.
- Bolhuis, G. K., Rexwinkel, E. G., & Zuurman, K. (2009). Polyols as filler-binders for disintegrating tablets prepared by direct compaction. *Drug Development Industrial Pharmacy*, 35(6), 671-677.

- Boon, W., & Van Wee, B. J. T. R. (2018). Influence of 3D printing on transport: a theory and experts judgment based conceptual model. 38(5), 556-575.
- Boontheekul, T., Kong, H.-J., & Mooney, D. J. (2005). Controlling alginate gel degradation utilizing partial oxidation and bimodal molecular weight distribution. *Biomaterials*, 26(15), 2455-2465.
- Braccini, I., & Pérez, S. (2001). Molecular basis of Ca2+-induced gelation in alginates and pectins: the egg-box model revisited. Biomacromolecules, 2(4), 1089-1096.
- Breitkreutz, J., & Boos, J. (2007). Paediatric and geriatric drug delivery. Expert opinion on drug delivery, 4(1), 37-45.
- Bulut, E. (2020). Flurbiprofen-loaded interpenetrating polymer network beads based on alginate, polyvinyl alcohol and methylcellulose: design, characterization and in-vitro evaluation. *Journal of Biomaterials Science, Polymer Edition*, 31(13), 1671-1688.
- Campbell, T. (2011). Could 3D printing change the world?: Technologies, potential, and implications of additive manufacturing.
- Cardoso, M. J., Costa, R. R., & Mano, J. F. (2016). Marine origin polysaccharides in drug delivery systems. *Marine drugs*, 14(2), 34.

- Castillo, J., Palomo-Canales, J., Garcia, J., Lastres, J., Bolas, F., & Torrado, J. (1999). Preparation and characterization of albendazole β-cyclodextrin complexes. *Drug development and industrial pharmacy*, 25(12), 1241-1248.
- Chan, I. S., & Ginsburg, G. S. (2011). Personalized medicine: progress and promise. *Annual review of genomics human genetics*, 12, 217-244.
- Chan, L. W., Ching, A. L., Liew, C. V., & Heng, P. W. S. (2007).
 Mechanistic study on hydration and drug release behavior of sodium alginate compacts. *Drug Development Industrial Pharmacy*, 33(6), 667-676.
- Chaudhary, M. K., Prajapati, P., Srivastava, K., Silva, K. F., Joshi, B. D., Tandon, P., & Ayala, A. P. (2021). Molecular interactions and vibrational properties of ricobendazole: Insights from quantum chemical calculation and spectroscopic methods. *Journal of Molecular Structure*, 1230, 129889.
- Coleman, R. J., Lawrie, G., Lambert, L. K., Whittaker, M., Jack, K. S., & Grøndahl, L. (2011). Phosphorylation of alginate: synthesis, characterization, and evaluation of in vitro mineralization capacity. *Biomacromolecules*, 12(4), 889-897.

- Dadsetan, M., Taylor, K. E., Yong, C., Bajzer, Ž., Lu, L., & Yaszemski, M. J. (2013). Controlled release of doxorubicin from pH-responsive microgels. *Acta biomaterialia*, 9(3), 5438-5446.
- Daemi, H., & Barikani, M. (2012). Synthesis and characterization of calcium alginate nanoparticles, sodium homopolymannuronate salt and its calcium nanoparticles. *Scientia Iranica*, 19(6), 2023-2028.
- Dai, L., Cheng, T., Duan, C., Zhao, W., Zhang, W., Zou, X., Aspler, J., Ni,
 Y. (2019). 3D printing using plant-derived cellulose and its derivatives:
 A review. *Carbohydrate polymers*, 203, 71-86.
- Degrassi, A., Toffanin, R., Paoletti, S., & Hall, L. D. (1998). A better understanding of the properties of alginate solutions and gels by quantitative magnetic resonance imaging (MRI). *Carbohydrate* research, 306(1-2), 19-26.
- Del Gaudio, P., De Cicco, F., Sansone, F., Aquino, R. P., Adami, R., Ricci, M., & Giovagnoli, S. (2015). Alginate beads as a carrier for omeprazole/SBA-15 inclusion compound: A step towards the development of personalized paediatric dosage forms. *Carbohydrate polymers*, 133, 464-472.

- Di Prima, M., Coburn, J., Hwang, D., Kelly, J., Khairuzzaman, A., & Ricles, L. (2016). Additively manufactured medical products—the FDA perspective. *3D printing in medicine*, 2(1), 1-6.
- Dib, A., Paredes, A. J., Eliópulos, N., Farias, C. E., Suárez, G., Aldrovandi,
 A., Palma, S. D., Allemandi, D. A., Lanusse, C. D., Sanchez Bruni, S. F.
 (2015). Pharmacokinetic Assessment of Novel Controlled Release
 Formulations of Ricobendazole Intended for Oral Administration in
 Dogs. Clinical & Experimental Pharmacology.
- Dille, M. J., Hattrem, M. N., & Draget, K. I. (2018). Soft, chewable gelatin-based pharmaceutical oral formulations: a technical approach.

 Pharmaceutical Development Technology, 23(5), 504-511.
- Draget, K. I., Skjåk-Bræk, G., & Smidsrød, O. (1997). Alginate based new materials. *International journal of biological macromolecules*, 21(1-2), 47-55.
- Drumond, N., & Stegemann, S. (2018). Polymer adhesion predictions for oral dosage forms to enhance drug administration safety. Part 3: Review of in vitro and in vivo methods used to predict esophageal adhesion and transit time. *Colloids Surfaces B: Biointerfaces*, 165, 303-314.

- Duffo, G., & Castillo, E. Q. (2004). Development of an artificial saliva solution for studying the corrosion behavior of dental alloys. *Corrosion*, 60(6), 594-602.
- Elbadawi, M., McCoubrey, L. E., Gavins, F. K., Ong, J. J., Goyanes, A., Gaisford, S., & Basit, A. W. (2021). Harnessing artificial intelligence for the next generation of 3D printed medicines. *Advanced Drug Delivery Reviews*, 175, 113805.
- Elbl, J., Gajdziok, J., & Kolarczyk, J. (2020). 3D printing of multilayered orodispersible films with in-process drying. *International Journal of Pharmaceutics*, 575, 118883.
- Erol-Taygun, M., Unalan, I., Idris, M. I. B., Mano, J. F., & Boccaccini, A. R. (2019). Bioactive glass-polymer nanocomposites for bone tissue regeneration applications: a review. *Advanced Engineering Materials*, 21(8), 1900287.
- Everett, H. (2021). Triastek Receives FDA IND Clearance for 3D Printed

 Drug to Treat Rheumatoid Arthritis. In 3D Printing Industry
- Fang, Y., Al-Assaf, S., Phillips, G. O., Nishinari, K., Funami, T., Williams,
 P. A., & Li, L. (2007). Multiple steps and critical behaviors of the binding of calcium to alginate. *The Journal of Physical Chemistry B*, 111(10), 2456-2462.

- Farhadnejad, H., Mortazavi, S. A., Erfan, M., Darbasizadeh, B., Motasadizadeh, H., & Fatahi, Y. (2018). Facile preparation and characterization of pH sensitive Mt/CMC nanocomposite hydrogel beads for propranolol controlled release. *International journal of biological macromolecules*, 111, 696-705.
- Gao, W., Zhang, Y., Ramanujan, D., Ramani, K., Chen, Y., Williams, C.
 B., Wang, C. C. L., Shin, Y. C., Zhang, S., Zavattieri, P. D. (2015). The status, challenges, and future of additive manufacturing in engineering. Computer-Aided Design, 69, 65-89.
- Goetz, L. H., & Schork, N. J. (2018). Personalized medicine: motivation, challenges, and progress. *Fertility sterility*, 109(6), 952-963.
- Goole, J., & Amighi, K. (2016). 3D printing in pharmaceutics: A new tool for designing customized drug delivery systems. *International Journal of Pharmaceutics*, 499(1-2), 376-394.
- Goyanes, A., Madla, C. M., Umerji, A., Piñeiro, G. D., Montero, J. M. G.,
 Diaz, M. J. L., Barcia, M. G., Taherali, F., Sanchez-Pintos, P., Couce, M.
 L., Gaisford, S., Couce, M.-L. (2019). Automated therapy preparation of isoleucine formulations using 3D printing for the treatment of MSUD:
 First single-centre, prospective, crossover study in patients.
 International Journal of Pharmaceutics, 567, 118497.

- Goyanes, A., Souto, C., & Martínez-Pacheco, R. (2010). Control of drug release by incorporation of sorbitol or mannitol in microcrystalline-cellulose-based pellets prepared by extrusion-spheronization.

 Pharmaceutical Development Technology, 15(6), 626-635.
- Grant, G. T. (1973). Biological interactions between polysaccharides and divalent cations: the egg-box model. *Febs Lett.*, 32, 195-198.
- Grøndahl, L., Lawrie, G., Anitha, A., & Shejwalkar, A. (2020). *Applications* of alginate biopolymer in drug delivery. In Biointegration of medical implant materials (pp. 375-403): Elsevier
- Gruwel, M. L., Yang, Y., de Gervai, P., Sun, J., & Kupriyanov, V. V. (2009). Magnetic resonance imaging tracking of alginate beads used for drug delivery of growth factors at sites of cardiac damage. *Magnetic resonance imaging*, 27(7), 970-975.
- Gutierrez, E., Burdiles, P. A., Quero, F., Palma, P., Olate-Moya, F., & Palza,
 H. (2019). 3D printing of antimicrobial alginate/bacterial-cellulose
 composite hydrogels by incorporating copper nanostructures. ACS
 Biomaterials Science Engineering, 5(11), 6290-6299.
- Hait, S. K., & Moulik, S. P. (2001). Determination of critical micelle concentration (CMC) of nonionic surfactants by donor-acceptor interaction with lodine and correlation of CMC with hydrophile-

- lipophile balance and other parameters of the surfactants. *Journal of Surfactants and Detergents*, 4(3), 303-309.
- Hanning, S. M., Lopez, F. L., Wong, I. C., Ernest, T. B., Tuleu, C., & Gul,
 M. O. (2016). Patient centric formulations for paediatrics and geriatrics:
 Similarities and differences. *International Journal of Pharmaceutics*,
 512(2), 355-359.
- Hariyadi, D. M., & Islam, N. (2020). Current status of alginate in drug delivery. *Advances in Pharmacological Pharmaceutical Sciences*, 2020.
- Hazur, J., Detsch, R., Karakaya, E., Kaschta, J., Teßmar, J., Schneidereit,
 D., Friedrich, O., Schubert, D. W., Boccaccini, A. R. (2020). Improving alginate printability for biofabrication: Establishment of a universal and homogeneous pre-crosslinking technique. *Biofabrication*, 12(4), 045004.
- Heggset, E. B., Strand, B. L., Sundby, K. W., Simon, S., Chinga-Carrasco,
 G., & Syverud, K. (2019). Viscoelastic properties of nanocellulose based
 inks for 3D printing and mechanical properties of CNF/alginate
 biocomposite gels. *Cellulose*, 26(1), 581-595.
- Herrada-Manchón, H., Rodríguez-González, D., Fernández, M. A., Suñé-Pou, M., Pérez-Lozano, P., García-Montoya, E., & Aguilar, E. (2020).

- 3D printed gummies: Personalized drug dosage in a safe and appealing way. *International Journal of Pharmaceutics*, 587, 119687.
- Higuchi, T. (1961). Rate of release of medicaments from ointment bases containing drugs in suspension. *Journal of Pharmaceutical Sciences*, 50(10), 874-875.
- Ho, D., Quake, S. R., McCabe, E. R., Chng, W. J., Chow, E. K., Ding, X.,
 Gelb, B. D., Ginsburg, G. S., Hassenstab, J., Ho, C.-M., Mobley, W. C.,
 Nolan, G. P., Rosen, S. T., Tan, P., Yen, Y., Zarrinpar, A. (2020).
 Enabling technologies for personalized and precision medicine. *Trends*in biotechnology, 38(5), 497-518.
- Hoffmann, E. M., Breitenbach, A., & Breitkreutz, J. (2011). Advances in orodispersible films for drug delivery. *Expert opinion on drug delivery*, 8(3), 299-316.
- Hölzl, K., Lin, S., Tytgat, L., Van Vlierberghe, S., Gu, L., & Ovsianikov,A. (2016). Bioink properties before, during and after 3D bioprinting.Biofabrication, 8(3), 032002.
- Hsiao, W.-K., Lorber, B., Reitsamer, H., & Khinast, J. (2018). 3D printing of oral drugs: a new reality or hype? *Expert opinion on drug delivery*, 15(1), 1-4.

- ISO/ASTM52900. (2021). Additive Manufacturing—General Principles—
 Fundamentals and Vocabulary. ASTM International Geneva,
 Switzerland.
- Jagdale, S. C., Agavekar, A. J., Pandya, S. V., Kuchekar, B. S., & Chabukswar, A. R. (2009). Formulation and evaluation of gastroretentive drug delivery system of propranolol hydrochloride.
 AAPS PharmSciTech, 10(3), 1071-1079.
- Jamróz, W., Szafraniec, J., Kurek, M., & Jachowicz, R. (2018). 3D printing in pharmaceutical and medical applications—recent achievements and challenges. *Pharmaceutical research*, 35(9), 1-22.
- Jang, J.-S. R., & Mizutani, E. (1996). Levenberg-Marquardt method for ANFIS learning. Proceedings of North American Fuzzy Information Processing (pp. 87-91): IEEE.
- Johannesson, J., Khan, J., Hubert, M., Teleki, A., & Bergström, C. A. (2021). 3D-printing of solid lipid tablets from emulsion gels.
 International Journal of Pharmaceutics, 597, 120304.
- Kafle, A., Luis, E., Silwal, R., Pan, H. M., Shrestha, P. L., & Bastola, A. K.
 (2021). 3D/4D Printing of polymers: Fused deposition modelling
 (FDM), selective laser sintering (SLS), and stereolithography (SLA).
 Polymers, 13(18), 3101.

- Kaygusuz, H., Evingür, G. A., Pekcan, Ö., von Klitzing, R., & Erim, F. B.
 (2016). Surfactant and metal ion effects on the mechanical properties of alginate hydrogels. *International journal of biological macromolecules*, 92, 220-224.
- Khaled, S. A., Burley, J. C., Alexander, M. R., & Roberts, C. J. (2014).Desktop 3D printing of controlled release pharmaceutical bilayer tablets.International journal of pharmaceutics, 461(1-2), 105-111.
- Khaled, S. A., Burley, J. C., Alexander, M. R., Yang, J., & Roberts, C. J. (2015a). 3D printing of five-in-one dose combination polypill with defined immediate and sustained release profiles. *Journal of Controlled Release*, 217, 308-314.
- Khaled, S. A., Burley, J. C., Alexander, M. R., Yang, J., & Roberts, C. J. (2015b). 3D printing of tablets containing multiple drugs with defined release profiles. *International Journal of Pharmaceutics*, 494(2), 643-650.
- Lanusse, C., Virkel, G., Sanchez, S., Alvarez, L., Lifschitz, A., Imperiale, F., & Monfrinotti, A. (1998). Ricobendazole kinetics and availability following subcutaneous administration of a novel injectable formulation to calves. *Research in veterinary science*, 65(1), 5-10.

- Leppiniemi, J., Lahtinen, P., Paajanen, A., Mahlberg, R., Metsä-Kortelainen, S., Pinomaa, T., Pajari, H., Vikholm-Lundin, I., Pursula, P.,
 Hytönen, V. P. (2017). 3D-printable bioactivated nanocellulose–alginate hydrogels. ACS applied materials interfaces, 9(26), 21959-21970.
- Levitt, M. H. (2013). *Spin dynamics: basics of nuclear magnetic resonance:*John Wiley & Sons.
- Li, P., Zhang, S., Sun, W., Cui, M., Wen, H., Li, Q., Pan, W., & Yang, X. (2019). Flexibility of 3D extruded printing for a novel controlled-release puerarin gastric floating tablet: design of internal structure. Aaps Pharmscitech, 20(6), 236.
- Li, Q., Guan, X., Cui, M., Zhu, Z., Chen, K., Wen, H., Jia, D., Hou, J., Xu, W., Yang, X., & Pan, W. (2018). Preparation and investigation of novel gastro-floating tablets with 3D extrusion-based printing. *International journal of pharmaceutics*, 535(1-2), 325-332.
- Liew, C. V., Chan, L. W., Ching, A. L., & Heng, P. W. S. (2006). Evaluation of sodium alginate as drug release modifier in matrix tablets.

 International Journal of Pharmaceutics, 309(1-2), 25-37.
- Lifschitz, A., Lanusse, C., & Alvarez, L. (2017). Host pharmacokinetics and drug accumulation of anthelmintics within target helminth parasites of ruminants. *New Zealand veterinary journal*, 65(4), 176-184.

- Liu, L. X., & Weller, P. F. (1996). Antiparasitic drugs. New England Journal of Medicine, 334(18), 1178-1184.
- Lopez-Garcia, M. L., Torrado-Duran, S., Torrado-Duran, J., Martínez-Fernández, A. R., & Bolás-Fernández, F. (1997). Albendazole versus ricobendazole (albendazole-sulphoxide) against enteral and parenteral stages of Trichinella spiralis in mice. *International journal for parasitology*, 27(7), 781-785.
- Mallakpour, S., Azadi, E., & Hussain, C. M. (2021). State-of-the-art of 3D printing technology of alginate-based hydrogels—An emerging technique for industrial applications. *dvances in Colloid Interface Science*, 293, 102436.
- Manners-Bell, J., & Lyon, K. (2012). The implications of 3D printing for the global logistics industry. *Transport Intelligence*, 1, 1-5.
- Marvola, M., Vahervuo, K., Sothmann, A., Marttila, E., & Rajaniemi, M. (1982). Development of a method for study of the tendency of drug products to adhere to the esophagus. *Journal of Pharmaceutical Sciences*, 71(9), 975-977.
- Mathur, S., & Sutton, J. (2017). Personalized medicine could transform healthcare. *Biomedical reports*, 7(1), 3-5.

- Mazzei, P., Cozzolino, V., & Piccolo, A. (2018). High-resolution magicangle-spinning NMR and magnetic resonance imaging spectroscopies distinguish metabolome and structural properties of maize seeds from plants treated with different fertilizers and arbuscular mycorrhizal fungi. *Journal of agricultural food chemistry*, 66(11), 2580-2588.
- McKellar, Q., & Scott, E. (1990). The benzimidazole anthelmintic agents-a review. *Journal of veterinary pharmacology and therapeutics*, 13(3), 223-247.
- Mezger, T. (2020). The rheology handbook: for users of rotational and oscillatory rheometers: European Coatings.
- Mohapatra, S., Kar, R. K., Biswal, P. K., & Bindhani, S. (2022).

 Approaches of 3D printing in current drug delivery. *Sensors International*, 3, 100146.
- Mørch, Ý., Donati, I., Strand, B., & Skjåk-Bræk, G. (2007). Molecular engineering as an approach to design new functional properties of alginate. *Biomacromolecules*, 8(9), 2809-2814.
- Naseri, E., Butler, H., MacNevin, W., Ahmed, M., & Ahmadi, A. (2020). Low-temperature solvent-based 3D printing of PLGA: a parametric printability study. *Drug Development Industrial Pharmacy*, 46(2), 173-178.

- Nuzzo, A., Mazzei, P., Drosos, M., & Piccolo, A. (2020). Novel humopectic hydrogels for controlled release of agroproducts. *ACS Sustainable Chemistry Engineering*, 8(27), 10079-10088.
- Nuzzo, A., Mazzei, P., Savy, D., Di Meo, V., & Piccolo, A. (2020). Bio-based hydrogels composed of humic matter and pectins of different degree of methyl-esterification. ACS Sustainable Chemistry, 25(12), 2936.
- Park, B. J., Choi, H. J., Moon, S. J., Kim, S. J., Bajracharya, R., Min, J. Y.,
 & Han, H.-K. (2019). Pharmaceutical applications of 3D printing technology: current understanding and future perspectives. *Journal of Pharmaceutical Investigation*, 49(6), 575-585.
- Paxton, N., Smolan, W., Böck, T., Melchels, F., Groll, J., & Jungst, T. (2017). Proposal to assess printability of bioinks for extrusion-based bioprinting and evaluation of rheological properties governing bioprintability. *Biofabrication*, 9(4), 044107.
- Peppas, N. A., & Sahlin, J. J. (1989). A simple equation for the description of solute release. III. Coupling of diffusion and relaxation. *International Journal of Pharmaceutics*, 57(2), 169-172.

- Potter, K., Carpenter, T., & Hall, L. (1994). Magnetic resonance imaging (MRI) of calcium alginate gels. *Magnetic resonance imaging*, 12(2), 309-311.
- Preis, M. (2015). Orally disintegrating films and mini-tablets—innovative dosage forms of choice for pediatric use. *AAPS PharmSciTech*, 16(2), 234-241.
- Prendergast, M. E., & Burdick, J. A. (2020). Recent advances in enabling technologies in 3D printing for precision medicine. *Advanced Materials*, 32(13), 1902516.
- Proietti, N., Capitani, D., Aru, V., Bellomaria, A., Bertocchi, F., Botta, B., Çela, D. (2017). NMR applications in food analysis: Part B. *Analytical chemistry: Developments, applications challenges in food science*, 255-296.
- Real, J. P., Barberis, M. E., Camacho, N. M., Bruni, S. S., & Palma, S. D. (2020). Design of novel oral ricobendazole formulation applying melting solidification printing process (MESO-PP): An innovative solvent-free alternative method for 3D printing using a simplified concept and low temperature. *International Journal of Pharmaceutics*, 587, 119653.

- Reis, C. P., Neufeld, R. J., Vilela, S., Ribeiro, A. J., & Veiga, F. (2006).
 Review and current status of emulsion/dispersion technology using an internal gelation process for the design of alginate particles. *Journal of microencapsulation*, 23(3), 245-257.
- Ricciardi, R., Gaillet, C., Ducouret, G., Lafuma, F., & Lauprêtre, F. (2003). Investigation of the relationships between the chain organization and rheological properties of atactic poly (vinyl alcohol) hydrogels. *Polymer*, 44(11), 3375-3380.
- Ritger, P. L., & Peppas, N. A. (1987). A simple equation for description of solute release II. Fickian and anomalous release from swellable devices. *Journal of Controlled Release*, 5(1), 37-42.
- Rodríguez-Dorado, R., Landín, M., Altai, A., Russo, P., Aquino, R. P., & Del Gaudio, P. (2018). A novel method for the production of core-shell microparticles by inverse gelation optimized with artificial intelligent tools. *International Journal of Pharmaceutics*, 538(1-2), 97-104.
- Ruiz, F., Vallet, T., Dufaÿ Wojcicki, A., Belissa, É., Fontan, J.-E., de Pontual, L., Boudy, V. (2019). Dosage form suitability in vulnerable populations: A focus on paracetamol acceptability from infants to centenarians. *PloS one*, 14(8), e0221261.

- Russo, P., Zacco, R., Rekkas, D. M., Politis, S., Garofalo, E., Del Gaudio, P., & Aquino, R. P. (2019). Application of experimental design for the development of soft-capsules through a prilling, inverse gelation process. *ournal of Drug Delivery Science Technology*, 49, 577-585.
- Rycerz, K., Stepien, K. A., Czapiewska, M., Arafat, B. T., Habashy, R., Isreb, A., Alhnan, M. A. (2019). Embedded 3D printing of novel bespoke soft dosage form concept for pediatrics. *Pharmaceutics*, 11(12), 630.
- Saleh Alghamdi, S., John, S., Roy Choudhury, N., & Dutta, N. K. (2021).

 Additive manufacturing of polymer materials: Progress, promise and challenges. *Polymers*, 13(5), 753.
- Schubert, D. W. (2022). Simple Model for the Spreading of Inks in Bioprinting—Revealing Relevant Scaling Laws—Part I Theory.

 *Macromolecular Theory Simulations, 31(1), 2100032.
- Schwab, A., Levato, R., D'Este, M., Piluso, S., Eglin, D., & Malda, J. (2020). Printability and shape fidelity of bioinks in 3D bioprinting. *Chemical reviews*, 120(19), 11028-11055.
- Shahare, M. B., Kadam, V. J., Jagdale, D. M., Gandhi, P. S., & Gaikwad,
 P. L. (2012). Synthesis and evaluation of novel anthelmentic
 benzimidazole derivatives. *Int. J. Res. Pharm. Chem*, 2(1), 132-136.

- Sheskey, P. J., Cook, W. G., & Cable, C. G. (2017). *Handbook of pharmaceutical excipients*: Pharmaceutical Press.
- Sjöholm, E., & Sandler, N. (2019). Additive manufacturing of personalized orodispersible warfarin films. *International Journal of Pharmaceutics*, 564, 117-123.
- Skaugrud, Ø., Hagen, A., Borgersen, B., & Dornish, M. (1999). Biomedical and pharmaceutical applications of alginate and chitosan. *Biotechnology* genetic engineering reviews, 16(1), 23-40.
- Smith, P. T., Basu, A., Saha, A., & Nelson, A. (2018). Chemical modification and printability of shear-thinning hydrogel inks for directwrite 3D printing. *Polymer*, 152, 42-50.
- Sonego, J. M., Santagapita, P. R., Perullini, M., & Jobbágy, M. (2016). Ca (II) and Ce (III) homogeneous alginate hydrogels from the parent alginic acid precursor: a structural study. *Dalton Transactions*, 45(24), 10050-10057.
- Soni, A., Gowthamarajan, K., & Radhakrishnan, A. (2018). Personalized Medicine and Customized Drug Delivery Systems: The New Trend of Drug Delivery and Disease Management. *International Journal of Pharmaceutical Compounding*, 22(2), 108-121.

- Sonnleitner, D., Schrüfer, S., Berglund, L., Schubert, D. W., & Lang, G. (2021). Correlating rheology and printing performance of fiber-reinforced bioinks to assess predictive modelling for biofabrication. *Journal of Materials Research*, 36(19), 3821-3832.
- Spasov, A., Smirnova, L., Iezhitsa, I., Sergeeva, S., & Ozerov, A. (2002).

 Pharmacokinetics of benzimidazole derivatives. *Voprosy meditsinskoi khimii*, 48(3), 233-258.
- Srikanth, M. V., Rao, N. S., Sunil, S. A., Ram, B. J., & Kolapalli, V. R. M. (2012). Statistical design and evaluation of a propranolol HCl gastric floating tablet. *Acta Pharmaceutica Sinica B*, 2(1), 60-69.
- Stoltenberg, I., & Breitkreutz, J. (2011). Orally disintegrating mini-tablets (ODMTs)—a novel solid oral dosage form for paediatric use. *European journal of pharmaceutics biopharmaceutics* 78(3), 462-469.
- Swisher, D. A., Sendelbeck, S. L., & Fara, J. W. (1984). Adherence of various oral dosage forms to the esophagus. *International Journal of Pharmaceutics*, 22(2-3), 219-228.
- Tagami, T., Ito, E., Kida, R., Hirose, K., Noda, T., & Ozeki, T. (2021). 3D printing of gummy drug formulations composed of gelatin and an HPMC-based hydrogel for pediatric use. *International Journal of Pharmaceutics*, 594, 120118.

- Takka, S. (2003). Propranolol hydrochloride–anionic polymer binding interaction. *Il Farmaco*, 58(10), 1051-1056.
- Tan, L. J., Zhu, W., & Zhou, K. (2020). Recent progress on polymer materials for additive manufacturing. Advanced Functional Materials, 30(43), 2003062.
- Thakur, S., & Arotiba, O. A. (2018). Synthesis, swelling and adsorption studies of a pH-responsive sodium alginate—poly (acrylic acid) superabsorbent hydrogel. *Polymer bulletin*, 75(10), 4587-4606.
- Tian, Y., Orlu, M., Woerdenbag, H. J., Scarpa, M., Kiefer, O., Kottke, D., Sjoholm, E., Oblom, H., Sandler, N., Hinrichs, W. L., Frijlink, H. W., Breitkreutz, J. & Visser, J. C. (2019). Oromucosal films: From patient centricity to production by printing techniques. *Expert opinion on drug delivery*, 16(9), 981-993.
- Varma, M. V. K., & Hemamalini, K. (2007). Comparative studies on the dissolution profile of flurbiprofen from coated and uncoated alginate microspheres. *Pharmacolonlin*, 202(2), 187.
- Vaz, V. M., & Kumar, L. (2021). 3D printing as a promising tool in personalized medicine. *AAPS PharmSciTech*, 22(1), 1-20.
- Vemula, S. K., Veerareddy, P. R., & Devadasu, V. R. (2015).

 Pharmacokinetics of colon-specific pH and time-dependent flurbiprofen

- tablets. European Journal of Drug Metabolism Pharmacokinetics, 40(3), 301-311.
- Venables, R., Batchelor, H., Hodson, J., Stirling, H., & Marriott, J. (2015).

 Determination of formulation factors that affect oral medicines acceptability in a domiciliary paediatric population. *International journal of pharmaceutics*, 480(1-2), 55-62.
- Visser, J., Wibier, L., Mekhaeil, M., Woerdenbag, H. J., & Taxis, K. (2020).

 Orodispersible films as a personalized dosage form for nursing home residents, an exploratory study. *International journal of clinical pharmacy*, 42(2), 436-444.
- Vizirianakis, I. S. (2004). Challenges in current drug delivery from the potential application of pharmacogenomics and personalized medicine in clinical practice. *Current Drug Delivery*, 1(1), 73-80.
- Wen, H., He, B., Wang, H., Chen, F., Li, P., Cui, M., Li, Q., Pan, W., & Yang, X. (2019). Structure-based gastro-retentive and controlled-release drug delivery with novel 3D printing. Aaps Pharmscitech, 20(2), 68.
- West, T. G., & Bradbury, T. J. (2019). 3D Printing: A Case of ZipDose® Technology–World's First 3D Printing Platform to Obtain FDA Approval for a Pharmaceutical Product. 3D 4D Printing in Biomedical Applications: Process Engineering Additive Manufacturing, 53-79.

- Wu, Z., Razzak, M., Tucker, I. G., & Medlicott, N. J. (2005).
 Physicochemical characterization of ricobendazole: I. Solubility, lipophilicity, and ionization characteristics. *Journal of pharmaceutical sciences*, 94(5), 983-993.
- Xiong, S., Chen, Y., Jia, W., Yang, X., Liu, K., Li, C., & Ling, G. (2021).

 Optimization of the co-axial dispensing nozzle of a 3D bioprinter for the fabrication of tubular structures with micro-channel encapsulation. *Journal of Micromechanics and Microengineering*, 31(4), 045009.
- Yan, T.-T., Lv, Z.-F., Tian, P., Lin, M.-M., Lin, W., Huang, S.-Y., & Chen, Y.-Z. (2020). Semi-solid extrusion 3D printing ODFs: an individual drug delivery system for small scale pharmacy. *Drug Development Industrial Pharmacy*, 46(4), 531-538.
- Yang, J.-S., Xie, Y.-J., & He, W. (2011). Research progress on chemical modification of alginate: A review. *Carbohydrate polymers*, 84(1), 33-39.
- Zajicek, A., Fossler, M. J., Barrett, J. S., Worthington, J. H., Ternik, R., Charkoftaki, G., Lum, S., Breitkreutz, J., Baltezor, M., Macheras, P., Chan, M., Agharkar, S., & MacLaren, D. D. (2013). A report from the pediatric formulations task force: perspectives on the state of child-friendly oral dosage forms. *The AAPS journal*, 15(4), 1072-1081.

Zhao, C., Zhang, C., Kang, H., Xia, Y., Sui, K., & Liu, R. (2017). Gelation of Na-alginate aqueous solution: A study of sodium ion dynamics via NMR relaxometry. *Carbohydrate polymers*, 169, 206-212.

Sitography

https://s3platform.jrc.ec.europa.eu/personalised-medicine

https://personalizedmedicinecoalition.org

https://www.fda.gov/about-fda/center-drug-evaluation-and-research-cder/emerging-technology-program

https://www.fda.gov/regulatory-information/search-fda-guidance-documents/technical-considerations-additive-manufactured-medical-devices

https://www.marketresearch.com/360iResearch-v4164/3D-Printed-Drugs-Research-Technology-32372054/

https://www.fda.gov/media/125479/download

https://www.fda.gov/regulatory-information/search-fda-guidance-documents/technical-considerations-additive-manufactured-medical-devices

Appendix

List of papers

- Auriemma, G.; Tommasino, C.; <u>Falcone, G.</u>; Esposito, T.; Sardo, C.;
 Aquino, R. P., Additive Manufacturing Strategies for Personalized Drug
 Delivery Systems and Medical Devices: Fused Filament Fabrication and
 Semi Solid Extrusion. Molecules 2022, 27(9), 2784
 https://doi.org/10.3390/molecules27092784
- Falcone, G.; Real, J. P.; Palma, S. D.; Aquino, R. P.; Del Gaudio, P.; Garofalo, E.; Russo, P., Floating Ricobendazole Delivery Systems: A 3D Printing Method by Co-Extrusion of Sodium Alginate and Calcium Chloride. International Journal of Molecular Sciences 2022, 23, (3), 1280. https://doi.org/10.3390/ijms23031280
- 3. **Falcone, G.**; Mazzei, P.; Piccolo, A.; Esposito, T.; Mencherini, T.; Aquino, R. P.; Del Gaudio, P.; Russo, P., Advanced printable hydrogels from pre-crosslinked alginate as a new tool in semi solid extrusion 3D printing process. Carbohydrate Polymers 2022, 276, 118746. https://doi.org/10.1016/j.carbpol.2021.118746

- Falcone, G.; Saviano, M.; Aquino, R. P.; Del Gaudio, P.; Russo, P.,
 Coaxial semi-solid extrusion and ionotropic alginate gelation: A successful duo for personalized floating formulations via 3D printing.
 Carbohydrate Polymers 2021, 260, 117791
 https://doi.org/10.1016/j.carbpol.2021.117791
- Saviano, M.; Bowles, B. J.; Penny, M. R.; Ishaq, A.; Muwaffak, Z.;
 Falcone, G.; Russo, P.; Hilton, S. T., Development, and analysis of a novel loading technique for FDM 3D printed systems: Microwave-assisted impregnation of gastro-retentive PVA capsular devices. International Journal of Pharmaceutics 2022, 613, 121386.
 https://doi.org/10.1016/j.ijpharm.2021.121386

Oral communications

- G. Falcone; M. Petraglia, A. Cotticelli, R.P. Aquino, P. Russo; Design and manufacturing of alginate soft tablets via semi solid extrusion 3D printing; Autumn Meeting for Young Chemists in Biomedical Sciences 2022 (3rd edition); Naples, Italy, 17-19 October 2022
- G. Falcone; M. Petraglia, A. Cotticelli, R.P. Aquino, P. Russo; Alginate-sorbitol matrix to develop an innovative soft-tablet via 3D printing;

XXI scuola dottorale in tecnologia farmaceutica; Università di Roma Sapienza, 5-7 settembre 2022

- G. Falcone, M. Petraglia, A. Cotticelli, R. P. Aquino, P. Del Gaudio, P. Russo; Coaxial Semi-soli extrusion 3D printing & ionotropic gelation for drug delivery application; 3D-printing of gels and aerogels;
 Training School on 3D-printing of gels and aerogels, Santiago de Compostela (Spain), 21-23 June 2022
- G. Falcone; R. P. Aquino; P. Del Gaudio; P. Russo; Pre-crosslinked alginate hydrogels: physico-chemical requirements for high 3D-printing performance; 13th World Meeting on Pharmaceutics,
 Biopharmaceutics and Pharmaceutical Technology; Rotterdam, The Netherlands, 28 31 March 2022
- G. Falcone, R. P. Aquino, P. Del Gaudio, P. Russo; Polysaccharides in Drug delivery: potentialities of alginate crosslinked hydrogels in Semisolid Extrusion 3D Printing; 4th International EPNOE Junior Scientist Meeting, February 3 & 4, 2021
- G. Falcone, T. Esposito, R. P. Aquino, G. Auriemma, P. Del Gaudio, P.Russo; Calcium Alginate hydrogels in Semi Solid Extrusion 3D

printing: physico-chemical requirements for high printing

performance; XXVII Congresso Nazionale della Società Chimica

Italiana; (remote mode); September 14-23, 2021

G. Falcone, M. Saviano, R.P. Aquino, P. Del Gaudio, P. Russo, P.;
Development and characterization of gastroretentive drug delivery
formulations produced via FDM 3D-printed coaxial semi-solid
extrusion systems; NanoInnovation Conference and Exhibition 2020,
Rome (remote mode), September 15-18, 2020